Springer ThesesRecognizing Outstanding Ph.D. Research

Kenichiro Hashimoto

Non-Universal Superconducting Gap Structure in Iron-Pnictides Revealed by Magnet Penetration Depth Measurements



Springer Theses

Recognizing Outstanding Ph.D. Research

For further volumes: http://www.springer.com/series/8790

Aims and Scope

The series "Springer Theses" brings together a selection of the very best Ph.D. theses from around the world and across the physical sciences. Nominated and endorsed by two recognized specialists, each published volume has been selected for its scientific excellence and the high impact of its contents for the pertinent field of research. For greater accessibility to non-specialists, the published versions include an extended introduction, as well as a foreword by the student's supervisor explaining the special relevance of the work for the field. As a whole, the series will provide a valuable resource both for newcomers to the research fields described, and for other scientists seeking detailed background information on special questions. Finally, it provides an accredited documentation of the valuable contributions made by today's younger generation of scientists.

Theses are accepted into the series by invited nomination only and must fulfill all of the following criteria

- They must be written in good English.
- The topic should fall within the confines of Chemistry, Physics, Earth Sciences, Engineering and related interdisciplinary fields such as Materials, Nanoscience, Chemical Engineering, Complex Systems and Biophysics.
- The work reported in the thesis must represent a significant scientific advance.
- If the thesis includes previously published material, permission to reproduce this must be gained from the respective copyright holder.
- They must have been examined and passed during the 12 months prior to nomination.
- Each thesis should include a foreword by the supervisor outlining the significance of its content.
- The theses should have a clearly defined structure including an introduction accessible to scientists not expert in that particular field.

Kenichiro Hashimoto

Non-Universal
Superconducting Gap
Structure in Iron-Pnictides
Revealed by Magnetic
Penetration Depth
Measurements

Doctoral Thesis accepted by Kyoto University, Kyoto, Japan



Author
Dr. Kenichiro Hashimoto
Department of Physics
Kyoto University
Kyoto
Japan

Supervisors
Prof. Takasada Shibauchi
Prof. Yuji Matsuda
Department of Physics
Kyoto University
Kyoto
Japan

ISSN 2190-5053 ISSN 2190-5061 (electronic) ISBN 978-4-431-54293-3 ISBN 978-4-431-54294-0 (eBook) DOI 10.1007/978-4-431-54294-0

Springer Tokyo Heidelberg New York Dordrecht London

Library of Congress Control Number: 2012955240

© Springer Japan 2013

This work is subject to copyright. All rights are reserved by the Publisher, whether the whole or part of the material is concerned, specifically the rights of translation, reprinting, reuse of illustrations, recitation, broadcasting, reproduction on microfilms or in any other physical way, and transmission or information storage and retrieval, electronic adaptation, computer software, or by similar or dissimilar methodology now known or hereafter developed. Exempted from this legal reservation are brief excerpts in connection with reviews or scholarly analysis or material supplied specifically for the purpose of being entered and executed on a computer system, for exclusive use by the purchaser of the work. Duplication of this publication or parts thereof is permitted only under the provisions of the Copyright Law of the Publisher's location, in its current version, and permission for use must always be obtained from Springer. Permissions for use may be obtained through RightsLink at the Copyright Clearance Center. Violations are liable to prosecution under the respective Copyright Law.

The use of general descriptive names, registered names, trademarks, service marks, etc. in this publication does not imply, even in the absence of a specific statement, that such names are exempt from the relevant protective laws and regulations and therefore free for general use.

While the advice and information in this book are believed to be true and accurate at the date of publication, neither the authors nor the editors nor the publisher can accept any legal responsibility for any errors or omissions that may be made. The publisher makes no warranty, express or implied, with respect to the material contained herein.

Printed on acid-free paper

Springer is part of Springer Science+Business Media (www.springer.com)

Parts of this thesis have been published in the following journal articles:

- 1. **K. Hashimoto**, K. Cho, T. Shibauchi, S. Kasahara, Y. Mizumaki, R. Katsumata, T. Terashima, H. Ikeda, M. A. Tanatar, H. Kitano, N. Salovich, R. W. Giannetta, A. Carrington, R. Prozorov, and Y. Matsuda, "Discovery of a quantum phase transition hidden beneath the superconducting dome of BaFe₂-(As_{1-x}P_x)₂", Science **336**, 1554 (2012).
- 2. **K. Hashimoto**, S. Kasahara, R. Katsumata, Y. Mizukami, M. Yamashita, H. Ikeda, T. Terashima, A. Carrington, Y. Matsuda, and T. Shibauchi, "Nodal versus nodeless order parameters in LiFeP and LiFeAs superconductors", Phys. Rev. Lett. **108**, 047003 (2012).
- 3. **K. Hashimoto**, A. Serafin, S. Tonegawa, R. Katsumata, R. Okazaki, T. Saito, H. Fukazawa, Y. Kohori, K. Kihou, C. H. Lee, A. Iyo, H. Eisaki, H. Ikeda, Y. Matsuda, A. Carrington, and T. Shibauchi, "Evidence for Superconducting Gap Nodes in the Zone-Centered Hole Bands of KFe₂As₂ from Magnetic Penetration-Depth Measurements", Phys. Rev. B **82**, 014526 (2010).
- 4. **K. Hashimoto**, M. Yamashita, S. Kasahara, Y. Senshu, N. Nakata, S. Tonegawa, K. Ikada, A. Serafin, A. Carrington, T. Terashima, H. Ikeda, T. Shibauchi, and Y. Matsuda, "Line Nodes in the Energy Gap of Superconducting BaFe₂(As_{1-x}P_x)₂ Single Crystals as Seen via Penetration Depth and Thermal Conductivity", Phys. Rev. B **81**, 220501 (2010).
- 5. K. Hashimoto, T. Shibauchi, S. Kasahara, K. Ikada, S. Tonegawa, T. Kato, R. Okazaki, C. J. van der Beek, M. Konczykowski, H. Takeya, K. Hirata, T. Terashima, and Y. Matsuda, "Microwave Surface-Impedance Measurements of the Magnetic Penetration Depth in Single Crystal Ba_{1-x}K_xFe₂As₂ Superconductors: Evidence for a Disorder-Dependent Superfluid Density", Phys. Rev. Lett. 102, 207001 (2009).
- K. Hashimoto, T. Shibauchi, T. Kato, R. Okazaki, H. Shishido, M. Ishikado, H. Kito, A. Iyo, H. Eisaki, S. Shamoto, and Y. Matsuda, "Microwave Penetration Depth and Quasiparticle Conductivity of PrFeAsO_{1-y} Single Crystals: Evidence for a Full-Gap Superconductor", Phys. Rev. Lett. 102, 017002 (2009).

Supervisor's Foreword

This thesis describes the scientific achievements of Dr. Kenichiro Hashimoto, which were made during his doctoral program in the Department of Physics, Kyoto University. During that relatively short time as a researcher, he obtained a number of important results on the superconducting properties in the recently discovered iron-pnictide high-temperature superconductors. As a supervisor of his master's and doctoral courses, I can introduce the most important two findings of his studies. One is the first determination of the superconducting gap structure in iron-pnictide superconductors, and the other is the first strong evidence for the presence of a quantum critical point inside the superconducting dome of iron-based superconductors.

Soon after the discovery of iron-pnictide superconductivity, many researchers in the field of superconductivity began studying this new class of materials. The record of superconducting transition temperature in these iron-based superconductors has been boosted up to 56 K during a very short period, and an immediate question arose about the mechanism of high-temperature superconductivity in these materials, which is closely related to the structure of the superconducting gap. Dr. Hashimoto provided the first evidence for a fully gapped superconductivity in one of these materials from the single crystalline study of the temperature dependence of the magnetic penetration depth—one of the most fundamental quantities that describe the superconducting state. Then he found that the gap structure is nonuniversal among the different materials with a slightly different multiband electronic structure, which is now considered as an important factor in understanding the unconventional nature of superconductivity in this class of materials.

The evidence for the quantum criticality inside the superconducting dome has been obtained from his careful study of the experimental determination of the absolute value of zero-temperature penetration depth as a function of chemical composition. He used three different methods to show unambiguously that the penetration depth has a sharp peak at a certain composition. This result, reported in the journal *Science* magazine, may address a key question on the general phase

diagram of unconventional superconductivity in the vicinity of magnetic order, which has been a central issue in strongly correlated electron systems.

I hope that there will be many grateful readers who will have gained a broad perspective of the superconducting properties in these fascinating systems as a result of the author's efforts.

Kyoto, Japan, August 2012

Takasada Shibauchi

Acknowledgments

I would like to thank Professor Yuji Matsuda, whose comments and suggestions were of inestimable value for my study. I would also like to acknowledge Professor Takasada Shibauchi for his valuable advice and great encouragement throughout this work. I learned how to grasp the essence of physics from them. Over the past five years, they spent a significant amount of time and energy on my work. Without their guidance and stimulation, this work would not have been possible.

I would like to thank Professor Antony Carrington especially for providing extensive advice with regard to the experiments using the tunnel diode oscillator. I worked in his laboratory two times for a total of four months to carry out magnetic penetration depth measurements. The expertise I acquired during those stays gave me the skills needed to build up the tunnel diode oscillator system in Kyoto. It also gave me the opportunity to collaborate with other leading researchers overseas in this field.

This study could not have been possible without high-quality single crystals. I am deeply indebted to my collaborators, especially to Dr. Sigeru Kasahara who provided us with very high-quality single crystals of $(Ba_{1-x}K_x)Fe_2As_2$, $BaFe_2(As_{1-x}P_x)_2$, LiFeAs, and LiFeP. I also wish to thank Dr. Motoyuki Ishikado, Prof. Shinichi Shamoto, Prof. Hijiri Kito, Prof. Akira Iyo, Prof. Chul-Ho Lee, Prof. Hiroshi Eisaki, Prof. Hiroyuki Takeya, Prof. Kazuto Hirata, Mr. Taku Saito, Prof. Hideto Fukazawa, and Prof. Yoh Kohori for providing high-quality single crystals of PrFeAsO_{1-y} and KFe₂As₂. I would like to thank Prof. C. J. van der Beek, Prof. Marcin Konczykowski, Prof. Kenji Ishida, Prof. Hiroaki Ikeda, Prof. Hiroshi Kontani, Prof. Ilya Vekhter, Prof. Anton Vorontsov, Prof. Ruslan Prozorov, and Prof. Makariy Tanatar for fruitful discussions. I thank Mr. Kosuke Ikada, Mr. Sho Tonegawa, Mr. Ryo Katsumata, and Mr. Yuta Mizukami for their experimental assistance. I would like to acknowledge Mr. Alessandro Serafin, Dr. Kyuil Cho, Prof. Ryuji Okazaki, Prof. Hiroaki Shishido, Prof. Yuichi Kasahara, and Prof. Yasuyuki Nakajima for their help.

x Acknowledgments

In addition, I would like to acknowledge Prof. Takahito Terashima and Prof. Minoru Yamashita for experimental support and helpful discussions. I am also deeply indebted to all members of the Matsuda–Shibauchi group at Kyoto University, namely, Dr. Swee Goh, Mr. Masaaki Shimozawa, Mr. Masaki Nagata, Mr. Hongjie Shi, Mr. Satoshi Yasumoto, Mr. Daiki Watanabe, and other members for their helpful assistance and stimulating discussions.

I would like to thank the staff of the Research Center for Low Temperature and Materials Sciences at Kyoto University and the cryogenic service laboratory at the Institute for Solid State Physics for providing me with liquid helium and liquid nitrogen. I also wish to thank the staff members of the machine shop at Kyoto University for their technical advice. I wish to acknowledge, as well, the financial support from the Research Fellowships of the Japan Society for the Promotion of Science for Young Scientists.

Finally, I would like to express my gratitude to my parents, my wife, and the rest of my family for their support and warm encouragement.

Contents

1			on	1 5
2	Sup	ercondi	ucting Gap Structure and Magnetic	
	Pen	etratior	n Depth	7
	2.1	Super	conducting Pairing Symmetry	7
	2.2	Super	conducting Gap Structure and Quasiparticle	
		Densit	ty of States	10
	2.3	Magne	etic Penetration Depth	12
		2.3.1	London Penetration Depth	12
		2.3.2		13
		2.3.3	Impurity Effect	15
	Refe	erences		17
3	Iror	-Based	Superconductors	19
	3.1	Crysta	al Structure of Iron-Based Superconductors	19
	3.2	Electr	onic Structure of Iron-Based Superconductors	21
		3.2.1	Band Structure Calculations	21
		3.2.2	Comparison with Experimental Fermi Surface	24
	3.3	Phase	Diagram	25
	3.4	Super	conducting Pairing Mechanism and Types	
		of Pai	ring Symmetry	27
	3.5	Super	conducting Gap Structure of Iron-Based	
		Super	conductors	30
		3.5.1	Penetration Depth	31
		3.5.2	Thermal Conductivity	35
		3.5.3	Nuclear Magnetic Resonance	37
		3.5.4	Angle Resolved Photoemission	
			Spectroscopy (ARPES)	39
		3.5.5	Neutron Scattering	40
	Refe	erences		41

xii Contents

4	Exp	rimental Method	45		
	4.1	Tunnel Diode Oscillator Technique	45		
		4.1.1 Principle	45		
		4.1.2 Tunnel Diode LC Oscillator	49		
		4.1.3 Experimental Setup	51		
		4.1.4 Al-Coating Method	53		
	4.2	Microwave Cavity Perturbation Technique	54		
		1	54		
		4.2.2 Surface Impedance	56		
		4.2.3 Experimental Setup	58		
	Refe	rences	61		
5	Sup	rconducting Gap Structure and Quantum Critical			
•			63		
	5.1		63		
		5.1.1 Phase Diagram	65		
			65		
			69		
	5.2		72		
	5.3				
			73		
			73		
		5.3.2 Comparisons with Thermal Conductivity			
			75		
			78		
			79		
	5.4	Results and Discussion 2: Quantum Critical Point Beneath			
		the Superconducting Dome	85		
	5.5	ž	91		
	Refe		91		
6	Sup	rconducting Gap Nodes in the Zone-Centered Hole			
	_		95		
	6.1		95		
	6.2				
	6.3	1			
			00 00		
		1	01		
		1	04		
	6.4		06		
		·	nz		

Contents xiii

7	Nodeless Versus Nodal Order Parameters			
	ın L		and LiFeP	10
	7.1	Stoich	iometric Superconducting System LiFeAs and LiFeP	10
	7.2 Experimental			11.
	7.3	Result	s and Discussion	1
		7.3.1	Penetration Depth	1
		7.3.2	Superfluid Density	1
		7.3.3	Electron–Electron Correlations	1
		7.3.4	Pnictogen-Height Dependence of Nodal	
			Versus Nodeless Behaviors	1
	7.4 Summary		12	
	Refe	References		
8	Con	alucian	S	1′

Chapter 1 Introduction

Abstract The discovery of high transition temperature (T_c) superconductivity up to 56 K in iron-based superconductors has attracted numerous interest both experimentally and theoretically. So far, various theories have been proposed for the pairing mechanism, but a consensus for the pairing symmetry in this system is still lacking. Therefore, the first experimental task to this problem is to elucidate the superconducting pairing symmetry, which is intimately related to the pairing interaction. To investigate the superconducting gap structure of iron-based superconductors, we have performed high-precision magnetic penetration depth measurements for several iron-pnictides. In addition, in this study, we have extended our research to explore a possible presence of a quantum critical point beneath the superconducting dome. The zero-temperature magnetic penetration depth measurements revealed the first convincing signature of a second-order quantum phase transition deep inside the dome, which may address a key question on the general phase diagram of unconventional superconductivity in the vicinity of a QCP. In this chapter, we will briefly overview the content of this book.

Keywords Iron-based superconductors · Superconducting pairing symmetry · Superconducting gap structure · Magnetic penetration depth · Quantum critical point

Superconductivity has remained an active area of research in the field of condensed matter physics since it was discovered one century ago [1]. In 1957, the Bardeen-Cooper-Schrieffer (BCS) theory [2] was advanced and successful in explaining the superconducting pairing mechanism of conventional superconductors. In conventional metals, superconductivity occurs at low temperatures when the conduction electrons form the so-called Cooper pairs, which are mediated by the interaction of electrons with phonons. Therefore, the attractive interaction between electrons is isotropic and the Cooper pairs are formed in a state with zero orbital angular momentum (*s*-wave pairing). In 1986, however, Bednorz and Müller discovered the high

1

2 1 Introduction

critical temperature (high- T_c) cuprate superconductors [3], demonstrating that very low temperatures are not indispensable for the appearance of superconductivity. It was a turning point and tremendous breakthrough in understanding unconventional superconductivity with angular momentum greater than zero. Unconventional superconductivity is mostly characterized by the anisotropic superconducting gap function with zeros (nodes) along certain directions in the momentum space [4]. For instance, it is widely believed that the high- T_c cuprates have a $d_{x^2-y^2}$ -wave symmetry [5, 6], which leads to line nodes along the c axis with fourfold symmetry within the basal ab plane. Since the superconducting gap structure is intimately related to the pairing interaction, a detailed knowledge of the gap structure and how it varies as a function of material parameters will give a strong guide to establishing the mechanism of high- T_c superconductivity.

The recent discovery of superconductivity in LaFeAsO_{1-x} F_x [7] has attracted much attention both experimentally and theoretically because of its high transition temperature $T_c \sim 26 \, \text{K}$. The subsequent development in this new class of superconductors, whose T_c has been immediately increased up to 56 K, has generated a huge boost of activity in this field and opened new routes to solve the problem of high- T_c superconductivity (see Fig. 1.1). These parent materials have an antiferromagnetic spin-density-wave (SDW) order, and the superconductivity can be induced by a variety of means such as doping or applying pressure [8]. Moreover, the electronic structure of these materials is quasi-two-dimensional. Such properties, i.e., the close proximity of magnetism and superconductivity, and quasi-2D structure may lead to speculation that the physics of iron-based superconductors is similar to the high- T_c cuprates. However, there exists a sharp contrast to the high- T_c cuprates: multi-band electronic structure with electron and hole pockets. So far, various theories have been proposed for the pairing symmetry in this system [9], ranging from an s_{\pm} -wave state with opposite signs between hole and electron pockets or s_{++} -wave state without sign change, to nodal s_{\pm} -wave or d-wave state, and more exotic order parameter such as p-wave state, but a consensus for the pairing symmetry in this system is still lacking. Therefore, the first experimental task is to clarify the superconducting pairing symmetry in the iron-based superconductors.

Until now, numerous experimental techniques have been developed in order to investigate the superconducting gap structure: penetration depth, thermal conductivity, electronic specific heat, NMR relaxation rate, ARPES measurements, and so on. Among them, the penetration depth λ , which is a direct measure of low-energy quasiparticle excitations, is a powerful probe to elucidate the superconducting gap structure, particularly the presence or absence of nodes. The temperature dependence of the penetration depth $\lambda(T)$ comes from the decrease in the screening superfluid by thermal excitations of quasiparticles. In fully gapped superconductors, the quasiparticle excitation is of thermally-activated type, so that the penetration depth λ shows an exponential temperature dependence. By contrast, in unconventional superconductors with nodes, thermally excited quasiparticles near the gap nodes give rise to a power-law temperature dependence of the penetration depth λ at low temperatures. For instance, in a clean superconductor with line nodes, such as the high- T_c cuprates with the $d_{x^2-y^2}$ symmetry, the temperature dependence of the penetration depth λ

1 Introduction 3

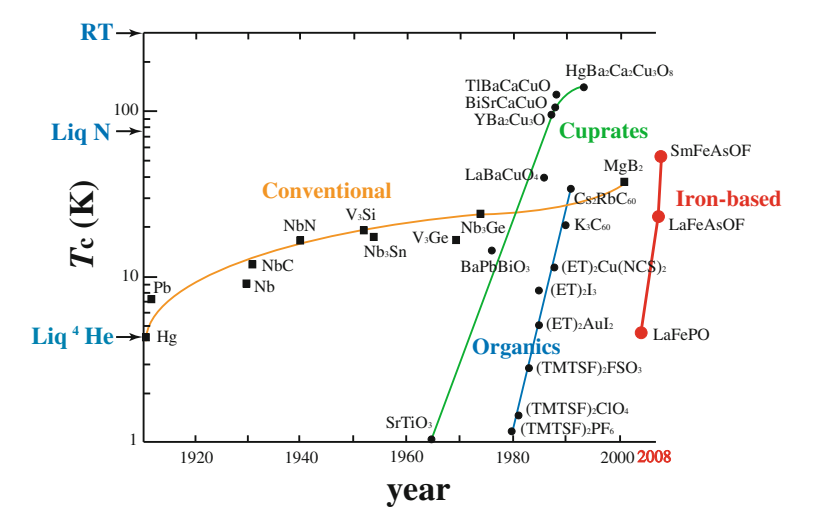


Fig. 1.1 Records of the superconducting transition temperature T_c for various superconductors

exhibits a *T*-linear behavior. Such differences offer important information on the superconducting gap structure.

In order to elucidate the superconducting gap structure of the iron-based superconductors, we have performed magnetic penetration depth measurements using tunnel diode oscillator and microwave cavity perturbation techniques; the tunnel diode oscillator technique provides very precise measurements of the variation in the penetration depth, while the microwave cavity perturbation technique gives important information on its absolute value. In the iron-based superconductors there is growing evidence that the superconducting gap structure is not universal. In certain materials such as optimally doped $(Ba_{1-x}K_x)Fe_2As_2$ and $Ba(Fe_{1-x}Co_x)_2As_2$, strong evidence for a fully gapped superconducting state has been observed from several low-energy quasiparticle excitation probes [10, 11]. In contrast, significant quasiparticle excitations at low temperatures due to nodes in the energy gap have been revealed in several iron-based superconductors in this study. These materials include BaFe₂(As_{1-x}P_x)₂. $(T_c \le 30 \,\mathrm{K})$ [12], KFe₂As₂ $(T_c = 4 \,\mathrm{K})$ [13], and LiFeP $(T_c = 5 \,\mathrm{K})$ [14]. This nonuniversality is quite different to the high- T_c cuprate superconductors which all have the nodal $d_{x^2-y^2}$ pairing state. So unlike the cuprates, the way that the superconducting gap structure depends on the detailed magnetic and electronic structure of individual iron-based superconductors provides a stringent test of candidate theories.

Another main topics of this thesis concerns whether high- T_c superconductivity is driven by an underlying quantum critical point (QCP). In particular, whether a QCP lies beneath the superconducting dome or the criticality is avoided by the transition to the superconducting state has been a central issue (see Fig. 1.2). A quantum phase transition is a phase transition at absolute zero temperature, which describes an abrupt change in the ground state of a many-body system due to its quantum fluctuations [15]. Contrary to classical phase transitions, quantum phase transitions can only

4 1 Introduction

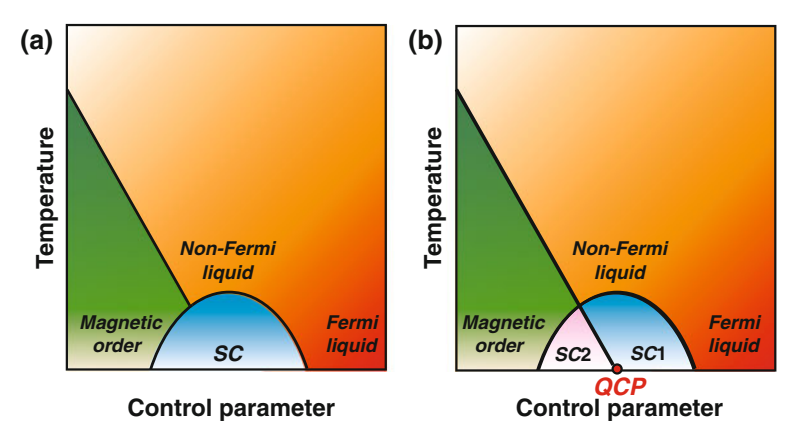


Fig. 1.2 Generic temperature versus nonthermal control parameter phase diagram sketches illustrating two cases. **a** Quantum criticality is avoided by the transition to the superconducting state. There is only one superconducting phase. **b** A QCP lies beneath the superconducting dome. The QCP separates two distinct superconducting phases (SC1 and SC2)

be accessed by varying a non-thermal control parameter, such as chemical doping, pressure, or magnetic field [16]. As mentioned above, cuprates and iron-pnictides share common features in that high- T_c superconductivity emerges in close proximity to an antiferromagnetically ordered state and a superconducting dome appears as a function of doping or pressure. Competing orders and quantum criticality are central issues in both systems. In particular, elucidating whether a QCP, at which the quantum critical transition takes place, is hidden inside the superconducting dome may be key to understanding high- T_c superconductivity. Moreover, unlike classical critical points driven by thermal fluctuations, the influence of the QCP can extend over a wide temperature range above the QCP. Both cuprates and iron-pnictides exhibit anomalous normal-state properties which strikingly deviate from the conventional Landau Fermi-liquid behaviors [15, 17, 18]. However, whether this strange metal phase is associated with the finite temperature quantum critical region linked to the QCP at zero temperature has been a highly controversial issue. For one thing the location of the QCP has been difficult to identify.

Pinning down the location of any QCP inside the superconducting dome is an extremely difficult experimental task because most physical quantities vanish below T_c . A sufficiently strong magnetic field can destroy the superconductivity, but the applied field may induce a different QCP or shift the zero field QCP [19]. The absolute value of λ in the zero-temperature limit immediately gives the superfluid density $\lambda^{-2}(0) = \mu_0 e^2 \sum_i n_i/m_i^*$, which is a direct probe of the superconducting state; here, m_i^* and n_i are the effective mass and concentration of the superconducting carriers in band i, respectively. Measurements on very high-quality crystals are indispensable because impurities and inhomogeneity may otherwise wipe out the signatures of the quantum critical transition. Another advantage of this approach is that it does not

1 Introduction 5

require the application of a strong magnetic field, which may induce a different QCP or shift the zero-field QCP [19].

In order to explore a possible presence of a QCP within the dome, we performed three different absolute penetration depth measurements for the BaFe₂(As_{1-x}P_x)₂ series. In this system, the isovalent substitution of P for As in the parent compound BaFe₂As₂ offers an elegant way to suppress magnetism and induce superconductivity [17]. Non-Fermi liquid properties are apparent in the normal state above the superconducting dome and de Haas-van Alphen (dHvA) oscillations [18] have been observed over a wide x range including the superconducting compositions, which give detailed information on the electronic structure. We find a sharp peak in the x-dependence of zero-temperature penetration depth $\lambda(0)$ at the optimum composition x = 0.30 ($T_c = 30$ K) [20]. This peak structure most likely results from pronounced quantum fluctuations associated with the QCP which separates two distinct superconducting phases, giving the first convincing signature of a second-order quantum phase transition deep inside the dome.

The thesis is structured as follows. In Chap. 2, we will give a brief account of the theory of superconductivity and magnetic penetration depth. In Chap. 3, we will briefly review the experimental and theoretical studies of iron-based superconductors. In Chap. 4, we will describe the details of experimental principles and methods for the magnetic penetration depth measurements including the tunnel diode oscillator and microwave cavity perturbation techniques. In Chap. 5, we will show the results of the penetration depth measurements and discuss the possible superconducting gap structure in isovalent-doped $BaFe_2(As_{1-x}P_x)_2$. We also argue the possibility of a quantum phase transition beneath the superconducting dome in $BaFe_2(As_{1-x}P_x)_2$. In Chap. 6, we will show the results of the end member of the hole-doped system, KFe_2As_2 . In Chap. 7, we show the results of the stoichiometric superconducting materials LiFeAs and LiFeP. We will summarize and conclude the present study in Chap. 8.

References

- 1. H.K. Onnes, Commun. Phys. Lab. Leiden 122, 124 (1911)
- 2. J. Bardeen, L.N. Cooper, J.R. Schriffer, Phys. Rev. 108, 1175 (1957)
- 3. J.G. Bednorz, K.A. Müller, Z. Phys. B 64, 189 (1986)
- 4. M. Sigrist, K. Ueda, Rev. Mod. Phys. 63, 239 (1991)
- 5. C.C. Tsuei, J.R. Kirtley, Rev. Mod. Phys. **72**, 969 (2000)
- 6. A. Damascelli, Z. Hussain, Z.X. Shen, Rev. Mod. Phys. 75, 473 (2003)
- 7. Y. Kamihara, T. Watanabe, M. Hirano, H. Hosono, J. Am. Chem. Soc. 130, 3296 (2008)
- 8. G.R. Stewart, Rev. Mod. Phys. 83, 1589 (2011)
- 9. P.J. Hirschfeld, M.M. Korshunov, I.I. Mazin, Rep. Prog. Phys. 74, 124508 (2011)
- K. Hashimoto, T. Shibauchi, T. Kato, R. Okazaki, H. Shishido, M. Ishikado, H. Kito, A. Iyo, H. Eisaki, S. Shamoto, Y. Matsuda, Phys. Rev. Lett. 102, 017002 (2009)
- K. Hashimoto, T. Shibauchi, S. Kasahara, K. Ikada, S. Tonegawa, T. Kato, R. Okazaki, C.J. van der Beek, M. Konczykowski, H. Takeya, K. Hirata, T. Terashima, Y. Matsuda, Phys. Rev. Lett. 102, 207001 (2009)

6 1 Introduction

K. Hashimoto, M. Yamashita, S. Kasahara, Y. Senshu, N. Nakata, S. Tonegawa, K. Ikada, A. Serafin, A. Carrington, T. Terashima, H. Ikeda, T. Shibauchi, Y. Matsuda, Phys. Rev. B 81, 220501 (2010)

- K. Hashimoto, A. Serafin, S. Tonegawa, R. Katsumata, R. Okazaki, T. Saito, H. Fukazawa, Y. Kohori, K. Kihou, C.H. Lee, A. Iyo, H. Eisaki, H. Ikeda, Y. Matsuda, A. Carrington, T. Shibauchi, Phys. Rev. B 82, 014526 (2010)
- K. Hashimoto, S. Kasahara, R. Katsumata, Y. Mizukami, M. Yamashita, H. Ikeda, T. Terashima,
 A. Carrington, Y. Matsuda, T. Shibauchi, Phys. Rev. Lett. 108, 047003 (2012)
- 15. S. Sachdev, B. Keimer, Phys. Today **64**, 29 (2011)
- P. Gegenwart, Q. Si, F. Steglich, Quantum criticality in heavy-fermion metals. Nat. Phys. 4, 186 (2008)
- S. Kasahara, T. Shibauchi, K. Hashimoto, K. Ikada, S. Tonegawa, H. Ikeda, H. Takeya, K. Hirata, T. Terashima, Y. Matsuda, Phys. Rev. B 81, 184519 (2010)
- H. Shishido, A.F. Bangura, A.I. Coldea, S. Tonegawa, K. Hashimoto, S. Kasahara, P.M.C. Rourke, H. Ikeda, T. Terashima, R. Settai, Y. Onuki, D. Vignolles, C. Proust, B. Vignolle, A. McCollam, Y. Matsuda, T. Shibauchi, A. Carrington, Phys. Rev. Lett. 104, 057008 (2010)
- 19. E.G. Moon, S. Sachdev, Phys. Rev. B **80**, 035117 (2009)
- K. Hashimoto, K. Cho, T. Shibauchi, S. Kasahara, Y. Mizumaki, R. Katsumata, T. Terashima, H. Ikeda, M.A. Tanatar, H. Kitano, N. Salovich, R.W. Giannetta, A. Carrington, R. Prozorov, Y. Matsuda, Science 336, 1554 (2012)

Chapter 2 Superconducting Gap Structure and Magnetic Penetration Depth

Abstract The BCS theory proposed by J. Bardeen, L. N. Cooper, and J. R. Schrieffer in 1957 is the first microscopic theory of superconductivity. In this theory, Fermi surface becomes gapped to avoid the instability caused even by an infinitely small interaction if it is attractive, which drives the system into the superconducting condensate state at low temperatures. The wave function that describes the electron pair, which serves as the order parameter, is related to the superconducting energy gap. Therefore, identifying the detailed superconducting gap structure is a major step toward clarifying the interactions that produce the pairing. Since the magnetic penetration depth is directly connected to the superfluid density, the measurement of the penetration depth is a powerful method to elucidate the superconducting gap structure, particularly the presence or absence of nodes. In this chapter, we will give a brief account of superconductivity and magnetic penetration depth.

Keywords Superconducting pairing symmetry · Superconducting gap structure · Low-energy quasiparticle excitations · Magnetic penetration depth

2.1 Superconducting Pairing Symmetry

In the BCS theory [1], the electron-phonon interaction leads to an effective attraction between electrons near the Fermi surface with opposite momenta and opposite spins, which eventually causes superconductivity. Below a critical temperature (T_c) , the electron pairs (the so-called Cooper pairs) condense into a coherent macroscopic quantum state, which is separated from the excited state by an energy gap 2Δ . This means that the amount of energy of at least 2Δ is required in order to break up one Cooper pair. Thus, the energy spectrum of quasiparticles E_k in a singlet superconducting state can be given by $E_k = \sqrt{\xi_k^2 + \Delta_k^2}$, where ξ_k represents the energy of an electron relative to the chemical potential with momentum k. Since the interaction of electrons with phonons is isotropic in the k-space, the Cooper pairs

are formed in a state with zero orbital angular momentum (*s*-wave pairing), which leads to a fully gapped superconducting state. On the other hand, unconventional superconductivity is mostly characterized by the anisotropic superconducting gap function with zeros (nodes) along certain directions in the momentum space. Thus, the superconducting gap structure is closely related to the paring interaction responsible for the superconductivity. Therefore detailed knowledge of the gap structure will give a strong guide to establishing the pairing mechanism of superconductivity.

The superconducting gap function $\Delta^\ell_{s_1,s_2}(k)$, which is proportional to the amplitude of the wave function of a Cooper pair $\Psi^\ell_{s_1,s_2}(k) = \langle \psi_{k,s_1} \psi_{-k,s_2} \rangle$, serves as an order parameter of the system [2]: it is non-zero only in the superconducting state. Here, k is the quasiparticle momentum, l is the orbital angular momentum, s_i is the electron spin, and ψ is the electron annihilation operator. In the simplest case where the spin-orbit coupling is negligible, the total angular momentum L and total spin $S = s_1 + s_2$ are good quantum numbers, and $\Psi^\ell_{s_1,s_2}(k)$ can be expressed in the form of a product of the orbital and spin parts,

$$\Psi_{s_1,s_2}^{\ell}(k) = g_{\ell}(k)\chi_s(s_1, s_2), \tag{2.1}$$

where $g_{\ell}(k)$ is the orbital wave function and $\chi_s(s_1, s_2)$ is the spin wave function. According to the Pauli's exclusion principle, the total wave function should change its sign under the exchange of two particles;

$$g_{\ell}(-k)\chi_s(s_2, s_1) = -g_{\ell}(k)\chi_s(s_1, s_2).$$
 (2.2)

The orbital part $g_{\ell}(k)$ can be expanded in terms of spherical harmonics $Y_{\ell m}(\hat{k})$, which are the eigenfunctions of the angular momentum operator with the momentum ℓ and its *z*-projections m,

$$g_{\ell}(k) = \sum_{m=-\ell}^{\ell} a_{\ell m}(k) Y_{\ell m}(\hat{k}), \qquad (2.3)$$

where $\hat{k} = k/k_{\rm F}$ represents the direction of the momentum. $g_\ell(k)$ is even for even values of ℓ and odd for odd values of ℓ , $g_\ell(k) = (-1)^\ell g_\ell(-k)$, and superconductors with $\ell = 0, 1, 2, \ldots$ are labeled as s, p, d, \ldots -wave, respectively. Hence, the spin component of a paired state with even (odd) orbital angular momentum ℓ should be antisymmetric (symmetric) under the exchange of particles.

The spin wave function of the Cooper pair $\chi_s(s_1, s_2)$ is a product of the one-particle spin wave functions,

$$\alpha_{\lambda} = \begin{pmatrix} 1 \\ 0 \end{pmatrix} = |\uparrow\rangle \text{ and } \beta_{\lambda} = \begin{pmatrix} 0 \\ 1 \end{pmatrix} = |\downarrow\rangle,$$
 (2.4)

which are eigenstates of the operators s^2 and s_z :

$$s_z = \frac{\hbar}{2} \begin{pmatrix} 1 & 0 \\ 0 & -1 \end{pmatrix}, \quad s_z \alpha_\lambda = \frac{\hbar}{2} \alpha_\lambda, \quad s_z \beta_\lambda = -\frac{\hbar}{2} \beta_\lambda.$$
 (2.5)

In the singlet state, S=0, the spin part of the wave function is antisymmetric with respect to the particle exchange. Therefore, the eigenfunction corresponding to the spin singlet state can be given by

$$\alpha_{1\lambda}\beta_{2\lambda} - \beta_{1\lambda}\alpha_{2\lambda} = |\uparrow\downarrow\rangle - |\downarrow\uparrow\rangle = \begin{pmatrix} 0 & 1 \\ -1 & 0 \end{pmatrix} = i\sigma_y,$$
 (2.6)

where σ_i (i = x, y, z) is the Pauli matrix,

$$\sigma_x = \frac{\hbar}{2} \begin{pmatrix} 0 & 1 \\ 1 & 0 \end{pmatrix}, \quad \sigma_y = \frac{\hbar}{2} \begin{pmatrix} 0 & -i \\ i & 0 \end{pmatrix}, \quad \sigma_z = \frac{\hbar}{2} \begin{pmatrix} 1 & 0 \\ 0 & -1 \end{pmatrix}. \tag{2.7}$$

As a result, the total wave function of the Cooper pair with S=0 is given by

$$\Psi_{singlet}^{\ell}(k) = g_{\ell}(k)i\sigma_{y}, \qquad (2.8)$$

where ℓ is even.

For spin triplet pairing (S=1), the spin wave functions corresponding to the three different spin projections on the quantization axis, which are symmetric under the exchange of particles, are given by

$$S_{z} = \begin{cases} 1, & \alpha_{1\lambda}\alpha_{2\mu} = |\uparrow\uparrow\rangle = \begin{pmatrix} 1 & 0 \\ 0 & 0 \end{pmatrix} \\ 0, & \alpha_{1\lambda}\beta_{2\mu} + \beta_{1\lambda}\alpha_{2\mu} = |\uparrow\downarrow\rangle + |\downarrow\uparrow\rangle = \begin{pmatrix} 0 & 1 \\ 1 & 0 \end{pmatrix} \\ -1, & \beta_{1\lambda}\beta_{2\mu} = |\downarrow\downarrow\rangle = \begin{pmatrix} 0 & 0 \\ 0 & 1 \end{pmatrix}. \end{cases}$$
 (2.9)

Consequently, the total wave function can be written as

$$\Psi_{triplet}^{\ell} = g_1(k) \mid \uparrow \uparrow \rangle + g_2(k)(\mid \uparrow \downarrow \rangle + \mid \downarrow \uparrow \rangle) + g_3(k) \mid \downarrow \downarrow \rangle = \begin{pmatrix} g_1(k) & g_2(k) \\ g_2(k) & g_3(k) \end{pmatrix}, \tag{2.10}$$

where $g_{\alpha}(k)$ is defined as the amplitudes of states with $S_z = 1, 0$, and -1, respectively,

$$g_{\alpha}(k) = \sum_{m=-l}^{l} a_{lm}^{\alpha} Y_{l}^{m}(\hat{k}) \qquad \alpha = 1, 2, 3.$$
 (2.11)

This equation can be rewritten as the following form by using the basis of the symmetric matrices $i\sigma\sigma_{\nu} = (i\sigma_{x}\sigma_{\nu}, i\sigma_{\nu}\sigma_{\nu}, i\sigma_{z}\sigma_{\nu})$,

$$\Psi_{triplet}^{\ell} = (d(k) \cdot \sigma) i \sigma_{y} = (d_{x}(k)\sigma_{x}, d_{y}(k)\sigma_{y}, d_{z}(k)\sigma_{z}) i \sigma_{y}$$

$$= \begin{pmatrix} -d_{x}(k) + i d_{y}(k) & d_{z}(k) \\ d_{z}(k) & d_{x}(k) + i d_{y}(k) \end{pmatrix}. \tag{2.12}$$

To summarize, the superconducting state can be characterized by its total spin S=0 (spin-singlet) and S=1 (spin-triplet). Thus, the superconducting gap functions for the singlet and triplet pairings are given by

$$\Delta_{k,\alpha\beta}^{s} = \Delta_{0}g(k)(i\sigma_{y})_{\alpha\beta}, \qquad (2.13)$$

$$\Delta_{k,\alpha\beta}^{t} = \Delta_0 d(k) (i\sigma\sigma_y)_{\alpha\beta}, \qquad (2.14)$$

where Δ_0 is the *k*-independent part of the gap. For the spin-singlet case, the energy of single particle excitation is given by

$$E_k = \sqrt{\xi_k^2 + \Delta_0^2 |g(k)|^2},\tag{2.15}$$

where ξ_k represents the band energy relative to the chemical potential. In the case of spin-triplet pairing state, if d is unitary it can be written as

$$E_k = \sqrt{\xi_k^2 + \Delta_0^2 |d(k)|^2}.$$
 (2.16)

If d is not-unitary, the excitation spectrum is given by

$$E_{k,\pm} = \sqrt{\xi_k^2 + \Delta_0^2(|d(k)|^2 \pm |d^*(k) \times d(k))|}.$$
 (2.17)

2.2 Superconducting Gap Structure and Quasiparticle Density of States

In this section, we focus on the quasiparticle density of states (QDOS) in a singlet superconducting state. The QDOS is defined as follows:

$$N(E) = \sum_{k} \delta(E - E_k). \tag{2.18}$$

From Eq. 2.15, if the superconducting order parameter Δ_k exhibits k-dependence, $\Delta_k \equiv \Delta_0 g(k)$, the quasiparticle energy in the spin-singlet state is given by

$$E_k = \sqrt{\xi_k^2 + \Delta_k^2}. (2.19)$$

Using Eqs. 2.18 and 2.19, we obtain

$$N(E) = \int \frac{d^3k}{(2\pi)^3} \delta(E - E_k) = N_0 \int \frac{d\Omega}{4\pi} \frac{E}{\sqrt{E^2 - \Delta_k^2}},$$
 (2.20)

where N_0 is the density of states in the normal state and Ω is the solid angle. It follows from Eq. 2.20 that for a conventional isotropic s-wave superconductor $(\Delta_k = \Delta_0)$,

$$N(E) = N_0 \begin{cases} 0 & (E < \Delta_0) \\ \frac{E}{\sqrt{E^2 - \Delta_0^2}} & (E > \Delta_0). \end{cases}$$
 (2.21)

The quasiparticle density of states for an s-wave superconductor drops abruptly to zero for $E < \Delta_0$. For a d-wave superconductor, $\Delta_k = \Delta_0 \cos{(2\varphi)}$, the quasiparticle density of states is given by

$$\frac{N(E)}{N_0} = \int_0^{2\pi} \frac{d\varphi}{2\pi} \frac{E}{\sqrt{E^2 - \Delta_k^2}} = \int_0^{2\pi} \frac{d\varphi}{2\pi} \frac{E}{\sqrt{E^2 - \Delta_0^2 \cos^2(2\varphi)}}.$$
 (2.22)

The last integral of Eq. 2.22 can be calculated by a numerical analysis. The result is given by

$$\frac{N(E)}{N_0} = \begin{cases}
\frac{2}{\pi} \frac{E}{\Delta_0} \kappa(\frac{E}{\Delta_0}) & (E < \Delta_0) \\
\frac{2}{\pi} \kappa(\frac{\Delta_0}{E}) & (E > \Delta_0).
\end{cases}$$
(2.23)

For $E \ll \Delta_0$, $\kappa(\frac{E}{\Delta_0}) \approx \frac{\pi}{2}$. Therefore we obtain

$$\frac{N(E)}{N_0} \approx \frac{E}{\Delta_0} \quad (E \ll \Delta_0). \tag{2.24}$$

In general, for the fully gapped state and nodal states with line node and point nodes, we obtain the following energy dependence of the density of states for $E \ll \Delta_0$ in the clean limit:

$$\frac{N(E)}{N_0} \propto \begin{cases}
0 & \text{(full gap)} \\
E & \text{(line node)} \\
E^2 & \text{(point node)}.
\end{cases}$$
(2.25)

The entire energy dependence of the quasiparticle states is summarized in Fig. 2.1.

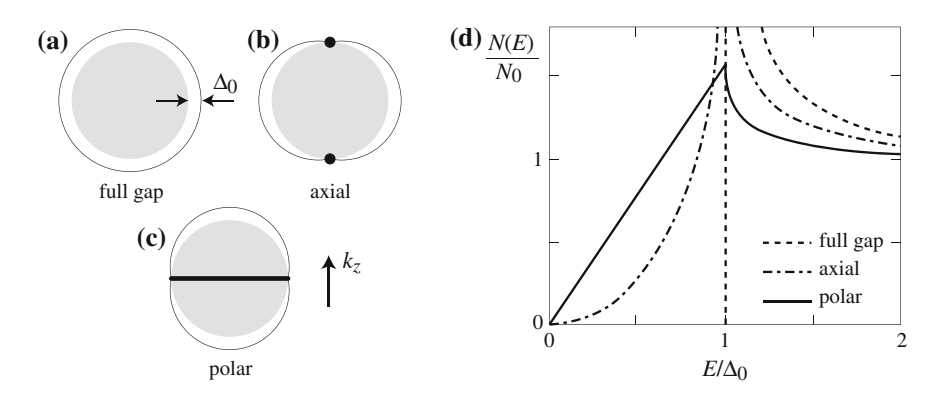


Fig. 2.1 Schematic pictures of the superconducting gap structure in a 3D spherical Fermi surface for **a** the fully gapped state and nodal state with **b** point nodes and **c** line node. The *shaded circles* represent the Fermi surface. The *thick line* and points represent the line node and point nodes, respectively. **d** The density of states of the quasiparticles N(E) for the fully gapped state and nodal state with point nodes and line node in the clean limit. N_0 represents the normal state density of states

2.3 Magnetic Penetration Depth

2.3.1 London Penetration Depth

The Meissner effect, which is one of the most striking and fundamental properties of superconductors, is the exclusion of a magnetic field from a superconducting material below its transition temperature. In a weak applied magnetic field, a superconductor expels nearly all magnetic flux, because the magnetic field induced by the supercurrents near its surface cancels the applied magnetic field within the bulk of the superconductor. However, near the surface, within a distance of the order of Angstroms, the magnetic field is not completely cancelled. Each superconducting material has its own characteristic penetration depth, which is the so-called London penetration depth λ_L . Since the penetration depth is directly connected to the superfluid density, the measurement of the penetration depth is a powerful method to elucidate the superconducting gap structure, particularly the presence or absence of nodes.

In the normal-state of a conventional metal, electrical conduction is well described by the Ohm's law $j = \sigma E$. On the other hand, in the superconducting state, the current density j is proportional to the applied vector potential A (the so-called London equation):

$$\mu_0 j = -\frac{ne^2}{m^*} A. \tag{2.26}$$

By combining the London equation with the Maxwell's equations, we obtain

$$\nabla^2 B = \frac{\mu_0 n e^2}{m^*} B. {(2.27)}$$

Let's discuss the penetration of a magnetic field into a superconductor by solving the London equation. Here we consider the simplest case, where the surface of the sample is defined by the xy plane, and the region of z < 0 is a vacuum [3]. We assume that the magnetic field is applied along the x direction. Since the field depends on only z, $B_x = B_x(z)$, we obtain

$$\frac{d^2z}{dz^2}B_x = \frac{1}{\lambda_L^2}B_x,\tag{2.28}$$

where the London penetration depth is defined as

$$\lambda_L = \left(\frac{\mu_0 n e^2}{m^*}\right)^{-1/2}. (2.29)$$

The solution of Eq. 2.28 gives the following form,

$$B_x(z) = B_x(0) \exp(-z/\lambda_L).$$
 (2.30)

The most striking consequence of the London equation is that the magnetic fields are screened from the interior of a bulk superconductor within a characteristic penetration depth λ_L , from which we can estimate the ratio of the concentration of the superconducting carriers to the effective mass, n/m^* .

2.3.2 Semiclassical Approach

In this subsection, we will describe the penetration depth in the framework of a semiclassical model given by Chandrasekhar and Einzel [4]. Here we focus on the case of the spin-singlet superconducting state [5]. This approach provides a general formula for all three spatial components of the penetration depth. In the London limit, the supercurrent j(r) is related to the vector potential A(r) through a tensor equation:

$$i = -\mathbb{R}A,\tag{2.31}$$

where the response tensor is given by

$$\mathbb{R}_{ij} = \frac{e^2}{4\pi^3\hbar} \oint_{FS} dS_k \left[\frac{v_F^i v_F^j}{|v_F|} \left(1 + 2 \int_{\Delta_k}^{\infty} \frac{\partial f(E_k)}{\partial E_k} \frac{N(E_k)}{N(0)} dE_k \right) \right]. \tag{2.32}$$

Here f is the Fermi function and v_F^i is the i-axis component of Fermi velocity v_F . $N(E)/N(0) = E/\sqrt{E^2 - \Delta_k^2}$ is the density of states normalized by its value at the Fermi level in the normal state. If we define λ_{ij}^{-2} as a response tensor in the London equation, $\mu_0 j_i = -\lambda_{ii}^{-2} A_i$, we obtain

$$\lambda_{ij}^{-2} = \frac{\mu_0 e^2}{4\pi^3 \hbar} \oint_{FS} dS_k \left[\frac{v_F^i v_F^j}{|v_F|} \left(1 + 2 \int_{\Delta(k)}^{\infty} \frac{\partial f(E_k)}{\partial E_k} \frac{N(E_k)}{N(0)} dE_k \right) \right]. \tag{2.33}$$

Here we note that the integral consists of two terms; the first term is diamagnetic and independent of temperature, while the second term is paramagnetic, temperature-dependent, and vanishes as the temperature goes to zero. If we assume that the effective mass m_{ii}^* is independent of temperature, then the normalized superfluid density are given by

$$\rho_{ii} = \frac{n_{ii}(T)}{n_{ii}(0)} = \left(\frac{\lambda_{ii}(0)}{\lambda_{ii}(T)}\right)^2.$$
 (2.34)

In the case of a 2D cylindrical Fermi surface, the normalized superfluid density is given by

$$\rho_{bb}^{aa} = 1 - \frac{1}{2\pi T} \int_0^{2\pi} \binom{\cos^2(\varphi)}{\sin^2(\varphi)} \int_0^\infty \cosh^{-2} \left(\frac{\sqrt{\varepsilon^2 + \Delta^2(T, \varphi)}}{2T} \right) d\varepsilon \, d\varphi, \quad (2.35)$$

where $\Delta(\varphi)$ is an angle-dependent gap function. For a 3D spherical Fermi surface and an anisotropic gap function $\Delta(\theta, \varphi)$, we obtain

$$\rho_{bb}^{aa} = 1 - \frac{3}{4\pi T} \int_0^1 (1 - z^2) \int_0^{2\pi} \begin{pmatrix} \cos^2(\varphi) \\ \sin^2(\varphi) \end{pmatrix}$$
$$\int_0^\infty \cosh^{-2} \left(\frac{\sqrt{\varepsilon^2 + \Delta^2(T, \theta, \varphi)}}{2T} \right) d\varepsilon \, d\varphi \, dz, \tag{2.36}$$

and

$$\rho_c = 1 - \frac{3}{2\pi T} \int_0^1 z^2 \int_0^{2\pi} \cos^2(\varphi) \int_0^\infty \cosh^{-2}\left(\frac{\sqrt{\varepsilon^2 + \Delta^2(T, \theta, \varphi)}}{2T}\right) d\varepsilon \, d\varphi \, dz,$$
(2.37)

where $z = \cos \theta$.

For an isotropic s-wave superconductor, both 2D and 3D expressions are given by [6]

$$\rho \approx 1 - \frac{1}{2T} \int_0^\infty \cosh^{-2} \left(\frac{\sqrt{\varepsilon^2 + \Delta^2(T)}}{2T} \right) d\varepsilon.$$
 (2.38)

Then we obtain the normalized fluid density for $T \ll T_c$,

$$\rho(T) = 1 - \sqrt{\frac{2\pi \Delta_0}{k_B T}} \exp\left(-\frac{\Delta_0}{k_B T}\right),\tag{2.39}$$

where Δ_0 is the magnitude of the superconducting gap at T=0 K. Hence, we obtain the penetration depth λ from Eq. 2.29,

$$\lambda(T) = \left(\frac{\mu_0 n e^2}{m^*}\right)^{-1/2}$$

$$\approx \lambda(0) \left[1 + \sqrt{\frac{\pi \Delta_0}{2k_B T}} \exp\left(-\frac{\Delta_0}{k_B T}\right)\right]. \tag{2.40}$$

For superconductors with line nodes, the normalized superfluid density ρ_s can be calculated as follows:

$$\rho_s \approx 1 - \frac{2\ln 2}{\Delta_0} T \quad (T \ll T_c), \tag{2.41}$$

which gives

$$\lambda(T) \approx \lambda(0) \left(1 + \frac{\ln 2}{\Delta_0} T \right). \tag{2.42}$$

For the fully gapped s-wave state, nodal state with line node and point nodes, we can summarize the temperature dependence of the penetration depth as follows:

$$\lambda(T) \propto \begin{cases} \exp\left(-\Delta_0/k_B T\right) & \text{(full gap)} \\ T & \text{(line node)} \\ T^2 & \text{(point node)}. \end{cases}$$
 (2.43)

Thus, we can distinguish types of the superconducting gap structure from the differences arising from the quasiparticle excitations.

2.3.3 Impurity Effect

The above discussion is restricted to pure systems without impurities. The introduction of controlled disorder has long been used as a probe of the gap structure

of unconventional superconductors. For conventional superconductors disorder has relatively little effect, however for unconventional superconductors the effects can be dramatic. Besides driving down T_c , disorder affects the low energy quasiparticle dynamics, for example, changing a T-linear behavior of the penetration depth to a quadratic T^2 behavior at low temperatures [7].

In unconventional superconductors where the gap has significant anisotropy or especially where it changes sign on different parts of the Fermi surface, non-magnetic impurities act as pair breakers, similar to magnetic impurities in conventional s-wave superconductors. For nodal superconductors in the strong scattering limit (unitary limit), quasiparticle density of states are bound to the non-magnetic impurity level with an energy close to E_F [8], which is a consequence of the interference of particle-like and hole-like excitations that undergo Andreev scattering arising from the sign changing order parameter and the scattering due to the impurities. A finite number of impurities broadens the bound state to the impurity band with bandwidth γ . As a result, a finite density of state appears at zero energy.

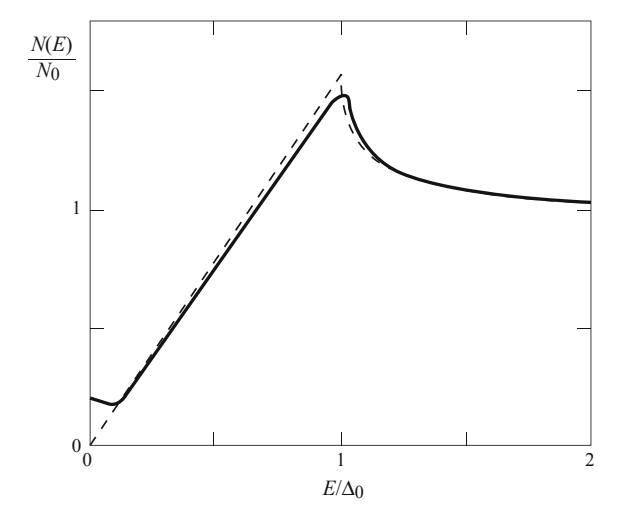
For superconductors with line nodes, γ and the density of quasiparticle bound states at zero energy N(0) become finite for any amount of impurity concentration. The energy dependence of the quasiparticle density of states is modified, as shown in Fig. 2.2. Due to the appearance of N(0), the density of states near Δ_0 is reduced.

In a two-dimensional d-wave superconductor, N(0) in the unitary limit is given by

$$\frac{N(0)}{N_0} = \frac{2\gamma}{\pi \Delta_0} \ln \left(\frac{\Delta_0}{\gamma}\right),\tag{2.44}$$

which is approximately given by $N(0)/N_0 \sim \gamma/\Delta_0$ at $\gamma \ll \Delta_0$. Therefore the impurity scattering modifies the temperature dependence of physical quantities at the

Fig. 2.2 $N(E)/N_0$ for an unconventional superconductor with line nodes in the superconducting gap. The *dashed line* represents the density of states in the absence of impurities. The *solid line* represents the density of states in the presence of dilute non-magnetic impurities $(\Gamma/\Delta_0 = 0.01)$ in the strong scattering limit (unitary limit). A finite density of states at zero energy N(0) appears



Quantity	9 8F m	Temperature dependence		
•		Clean limit	Unitary limit	
Specific heat	С	T^2	T	
NMR relaxation rate	$1/T_{1}$	T^3	T	
Penetration depth	λ	T	T^2	

Table 2.1 Temperature dependence of several physical quantities in superconductors with line nodes in the superconducting gap in a clean limit and unitary limit

region of $k_BT < \gamma$, where the impurity-induced N(0) dominates the transport and thermodynamic properties. For instance, the penetration depth changes from a T-linear behavior to a quadratic T^2 behavior at low temperatures. In Table 2.1, we summarize the power-law behaviors of the specific heat C, NMR relaxation rate $1/T_1$, and magnetic penetration depth λ for superconductors with line nodes in the superconducting gap, both in pure system and in the presence of impurities.

References

- 1. J. Bardeen, L.N. Cooper, J.R. Schrieier, Phys. Rev. 108, 1175 (1957)
- V.P. Mineev, K.V. Samokhin, Introduction to Unconventional Superconductivity, (Gordon and Breach Science Publishers, New York, 1999)
- 3. M. Tinkham, Introduction to Superconductivity, 2nd edn. (McGraw-Hill, New York, 1996)
- 4. B.S. Chandrasekhar, D. Einzel, Ann. Physik. 2, 535 (1993)
- For the case of a spin-triplet superconductor, see, for example, D. Einzel, P.J. Hirschfeld, F. Gross, B.S. Chandrasekhar, K. Andres, H.R. Ott, J. Beuers, Z. Fisk, J.L. Smith, Phys. Rev. Lett. 56, 2513 (1986)
- 6. R. Prozorov, R.W. Giannetta, Supercond. Sci. Technol. 19, R41 (2006)
- D.A. Bonn, S. Kamal, K. Zhang, R. Liang, D.J. Baar, E. Klein, W.N. Hardy, Phys. Rev. B 50, 4051 (1994)
- 8. P.J. Hirschfeld, N. Goldenfeld, Phys. Rev. B 48, 4219 (1993)

Chapter 3 Iron-Based Superconductors

Abstract Since the discovery of superconductivity in LaFeAsO $_{1-x}F_x$, which generated a new route to solve the problem of high- T_c superconductivity, tremendous efforts have been devoted for identifying the pairing mechanism of this new class of superconductors. So far, various theories have been proposed for the pairing symmetry in this system, ranging from an s_\pm -wave state with opposite signs between hole and electron pockets or s_{++} -wave state without sign change, to nodal s_\pm -wave or d-wave state, and more exotic order parameter such as p-wave state, but a consensus for the pairing symmetry in this system is still lacking. Therefore, the first experimental task is to clarify the superconducting pairing symmetry in the iron-based superconductors. In this chapter, we will briefly review the experimental and theoretical studies of iron-based superconductors.

Keywords Iron-based superconductors · Superconducting pairing symmetry · Superconducting gap structure

3.1 Crystal Structure of Iron-Based Superconductors

Since the discovery of superconductivity in LaFeAsO_{1-x}F_x with $T_c = 26 \,\mathrm{K}$ [1], a series of REFeAsO superconductors (the so-called '1111' system, RE: rare earth such as La, Ce, Pr, Nd, and Sm) have been reported [2–10]. REFeAsO has a tetragonal ZrCuSiAs-type crystal structure (space group P4/nmm) with alternating layers of REO and FeAs, stacked sequentially along the c-axis, as shown in Fig. 3.1a. The chemical formula can be expressed as $(RE^{3+}O^{2-})^{+}(\text{FeAs})^{-}$. The parent materials show an antiferromagnetic spin-density-wave (SDW) transition [11] as well as a tetragonal-to-orthorhombic structural phase transition, and exhibit no superconductivity. With electron doping by replacing oxygen with fluorine or creating oxygen deficit, or hole doping achieved by substituting, for example, La for Sr, superconductivity appears. In addition, it has been reported that superconductivity emerges by

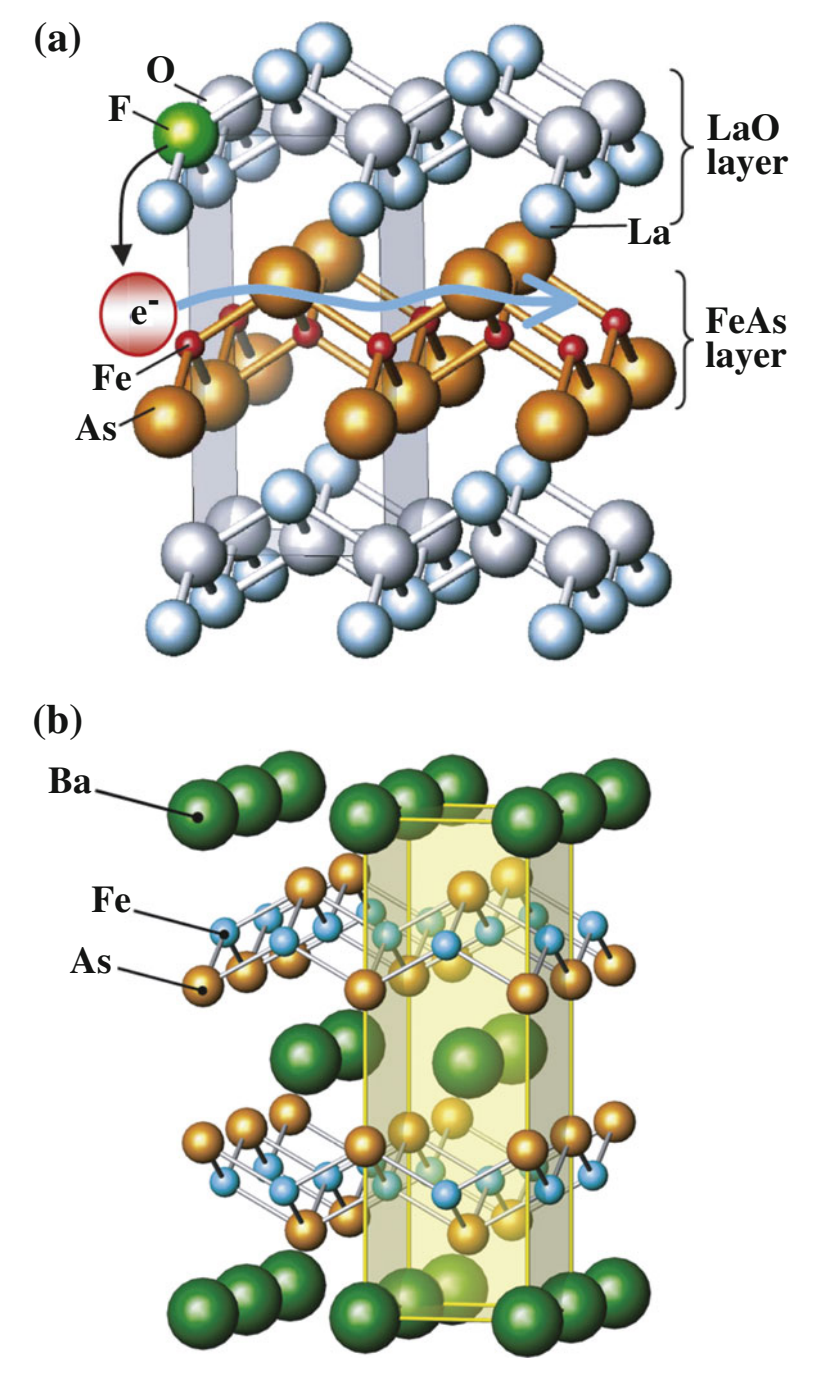


Fig. 3.1 Schematic crystal structures of a LaFeAsO $_{1-x}F_x$ and b BaFe $_2$ As $_2$. FeAs tetrahedra form two-dimensional layers, surrounded by the layers of LaO or Ba. Fe ions inside tetrahedra form square lattice. The figures are taken from Refs. [2, 12]

applying pressure [2]. The superconducting transition temperature in the '1111' system was immediately raised to 56 K.

Subsequently, oxygen-free iron-based superconductor $Ba_{1-x}K_xFe_2As_2$ ('122' system) was discovered [13]. The parent material AFe_2As_2 (A=Ba, Sr, Ca) has a tetragonal ThCr₂Si₂-type structure with space group I4/mmm, as shown in Fig. 3.1b. By replacing the alkaline earth element A of the parent compound AFe_2As_2 with K, Cs, and Na, which corresponds to hole doping, superconductivity up to 38 K was reported. Soon after that, with electron doping by replacing Fe with transition metal such as Co, Ni, Rh, and Pd, superconductivity with $T_c \le 25$ K was discovered. The so-called isovalent doping achieved by substituting P for As or Ru for Fe in AFe_2As_2 also induces superconductivity. These compounds are also formed by the layers of $(FeAs)^-$ interlaced with the layers of A^{2+} , which lead to a simple chemical formula $Ba^{2+}(Fe_2As_2)^{2-}$. Thus, both in the '1111' and '122' systems, $FeAs_4$ tetrahedra network forms two-dimensional layers surrounded by the layers of REO or A. Therefore, the FeAs layer is responsible for the antiferromagnetism and superconductivity in the iron-based superconductors.

In addition to the '1111' and '122' systems, other iron-based superconductors, such as LiFeAs [14, 15] ('111'), FeSe [16] ('11'), and Sr_2VO_3FeAs [17] ('21311'), have been discovered (see Fig. 3.2). The common feature of the crystal structure for all classes of these compounds is that the FeAs₄/FeSe₄ tetrahedra form the two-dimensional planes. In LiFeAs ($T_c = 18\,\mathrm{K}$) and LiFeP ($T_c = 5\,\mathrm{K}$) of the '111' family, superconductivity occurs in stoichiometric composition without either a magnetic transition or a structural transition. In Table 3.1, we summarize the lattice parameters of each parent compound.

3.2 Electronic Structure of Iron-Based Superconductors

3.2.1 Band Structure Calculations

A knowledge of the electronic structure in novel superconductors is essential for clarifying the superconducting pairing mechanism. Detailed band structure calculations for all classes of these compounds [18–21] have been performed. The obtained results are similar in all studies, which are characterized by quasi-two-dimensionality and multi-band nature. In Fig. 3.3, we show the band structure of LaFeAsO [22] near the Fermi level. The Fermi level is crossed by five bands, which are formed by five-fold degenerated Fe 3d orbitals. The Fermi surface consists of five quasi-cylindrical pockets: three hole pockets at the center of the Brillouin zone (Γ point), and two electron pockets centered at its corners (M point), as shown in Fig. 3.4. Thus, although the two dimensional nature in iron-based superconductors is similar to the high- T_c cuprates, superconductivity in this system is formed in multiple band system with electron and hole pockets, which is drastically different from the simple one-band picture in high- T_c cuprates. The hole-like cylinders at the Γ point and electron-like

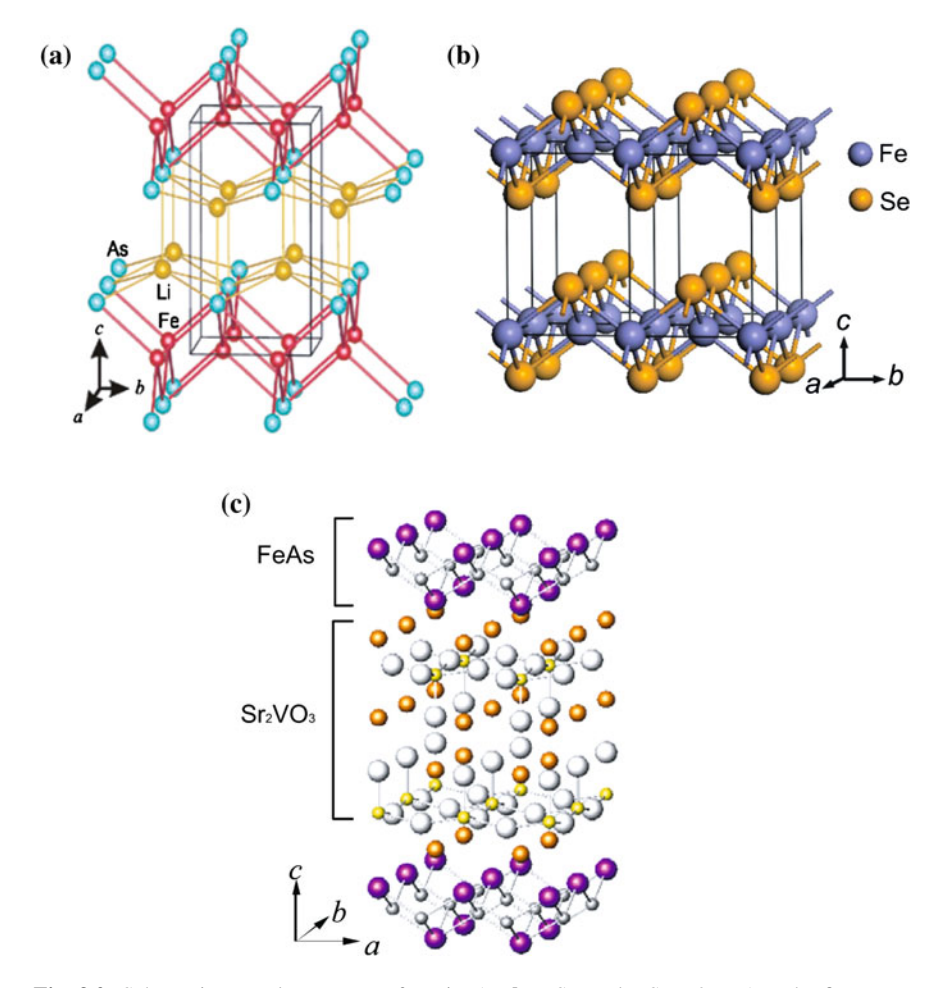


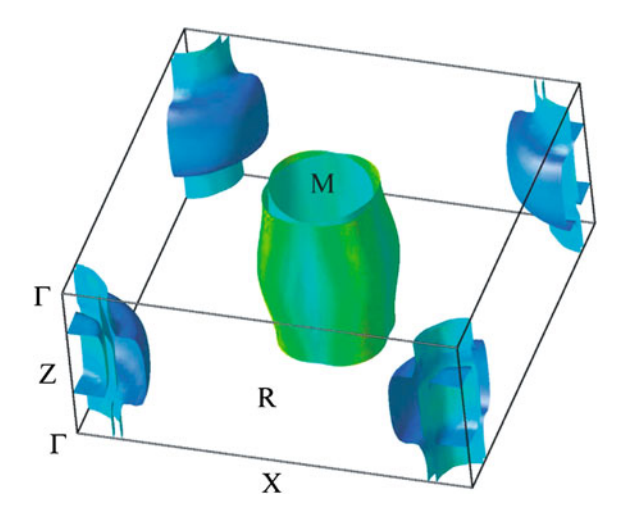
Fig. 3.2 Schematic crystal structures of a LiFeAs, b FeSe, and c Sr₂VO₃FeAs. The figures are taken from Refs. [16, 17]

Table 3.1 Lattice parameters of LaFeAsO, BaFe₂As₂, LiFeAs, FeSe, and Sr₂VO₃FeAs

Compound	Group	a(Å)	c(Å)
LaFeAsO	P4/nmm	4.03533	8.74090
$BaFe_2As_2$	I4/mmm	3.9090	13.2122
LiFeAs	P4/nmm	3.776	6.349
FeSe	P4/nmm	3.7693	5.4861
Sr ₂ VO ₃ FeAs	P4/nmm	3.9296	15.6732

Fig. 3.3 Band structure of LaFeAsO around E_F . The unshifted band structure is indicated by the *black solid line*, while the band structures for the As planes shifted by 0.035 Å towards and away from the Fe planes are indicated by the *blue* and *green dotted lines*, respectively. The figure is taken from Ref. [22]

Fig. 3.4 Fermi surface of LaFeAsO based on the LDA calculations. The *shading* represents the Fermi velocity [darker (*blue*) is low velocity]. The symmetry points are $\Gamma = (0, 0, 0)$, Z = (0, 0, 1/2), X = (1/2, 0, 0), R = (1/2, 0, 1/2), M = (1/2, 1/2, 0). The figure is taken from Ref. [22]



ones at the M point are nearly nested and can yield strong nesting peaked at (π, π) in the folded Brillouin zone (two Fe atoms in the unit cell), which lead to enhanced spin fluctuations at this nesting vector. Sufficiently strong spin fluctuations can cause a stripe-type SDW ordering, which is indeed observed as ground states for the parent materials [11]. The main effect of doping or applying pressure is a change in the relative sizes of the electron and hole Fermi surfaces, which causes a reduction in the degree of nesting in the Fermi surface.

3.2.2 Comparison with Experimental Fermi Surface

Angle resolved photoemission spectroscopy (ARPES) and de Haas-van Alphen (dHvA) measurements provide us valuable information on the Fermi surface topology and its volume. Soon after the discovery of LaFeAsO_{1-x}F_x, ARPES measurements were performed on single crystals of NdFeAsO_{0.9}F_{0.1} with $T_c \sim 53$ K [23]. In Fig. 3.5, we show the maps of the ARPES intensity, which are in reasonable agreement with the results of the local density approximation (LDA) band calculations, although the number of the Fermi surface sheets is unclear because of the poor resolution. The main disagreement is the size of the hole pocket and the ratio of its radius to that of the electron pocket, which is perhaps attributed to the surface effect. The band structures of the other iron-based superconductors have been so far investigated by several ARPES groups, and it has been reported that there are two or three hole

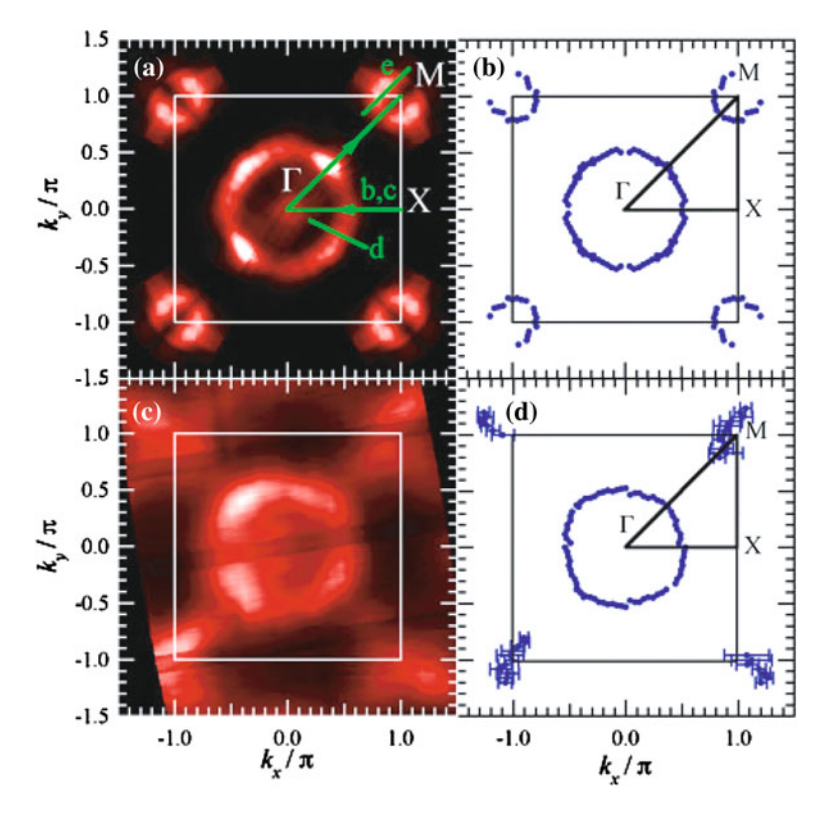


Fig. 3.5 a Fermi surfaces of NdFeAsO $_{0.9}$ Fo $_{0.1}$ determined by using 22 eV photon at 70 K. **b** The locations of the Fermi surfaces extracted from the raw data by fitting to the momentum distribution curves. **c**, **d** The same data in **a** and **b**, but obtained with 77 eV photon. The figure is taken from Ref. [23]

pockets centered at the Γ point and two electron pockets near the zone corners, which are in reasonable agreement with the band calculations.

dHvA measurements were first reported for the P-analogue LaFePO [24, 25]. The observed five Fermi surfaces are in agreement with the band calculations with the quasiparticle mass enhanced by a factor \sim 2, which reveal that the quasi-two dimensional Fermi surface consist of nearly nested electron and hole pockets. It has been established that the conventional density functional theory (DFT) band structure calculations using LDA with appropriate band energy shifts are almost in exact agreement with the dHvA results. In the isovalent doping system BaFe₂(As_{1-x}P_x)₂, dHvA oscillations have been observed in a wide range of x (0.4 < x < 1), covering the superconducting dome [26]. Recently, the Fermi surface in the antiferromagnetic phase of BaFe₂As₂ has been revealed by Shubnikov-de Haas (SdH) oscillation measurements on detwinned single crystals [27], which can be accounted for by a standard band structure calculation within the local spin density approximation (LSDA).

3.3 Phase Diagram

In the iron-based superconductors, the parent materials exhibit an antiferromagnetic (AFM) SDW transition (T_N) and a tetragonal-to-orthorhombic structural phase transition (T_s). Both T_N and T_s are suppressed by doping or pressure, and then superconductivity appears. In Fig. 3.6a, we show the typical temperature dependence of the electrical resistivity for the electron-doped LaFeAsO_{1-x}F_x [28] with different concentrations of fluorine x. The resistivity of the parent compound LaFeAsO shows a weak temperature dependence, and exhibits a sharp drop at around 150 K.

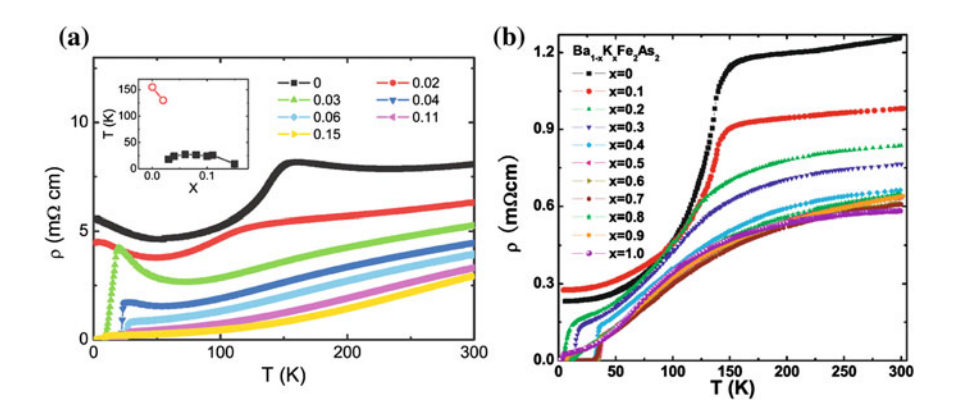


Fig. 3.6 a Resistivity of LaFeAsO_{1-x}F $_x$ for several doping levels x as a function of temperature [28]. **b** Resistivity for Ba_{1-x}K $_x$ Fe₂As₂ with several doping levels x [29]. The figures are taken from Refs. [28, 29]

With increasing doping level, the anomaly shifts to lower temperatures, and becomes less pronounced. When the anomaly is suppressed, superconductivity appears. This anomaly is attributed to the structural phase transition, or the resulting SDW transition. The hole-doped $Ba_{1-x}K_xFe_2As_2$ [29] also demonstrates the characteristic anomaly in the vicinity of $T \sim 150 \, \text{K}$ as shown in Fig. 3.6b, which is connected to the SDW or structural phase transition.

The first detailed phase diagram was obtained from the neutron scattering experiments. We demonstrate the results of the electron-doped LaFeAsO system [11], which reveals that the structural transition from tetragonal P4/nmm into orthorhombic Cmma structure takes place at 150 K, and afterwards antiferromagnetic ordering appears at 134 K. In Fig. 3.7, we show the reported antiferromagnetic structure, as well as the temperature dependence of the square of the magnetic moment μ^2 at Fe site. The spin ordering in the ab plane takes the form of characteristic chains,

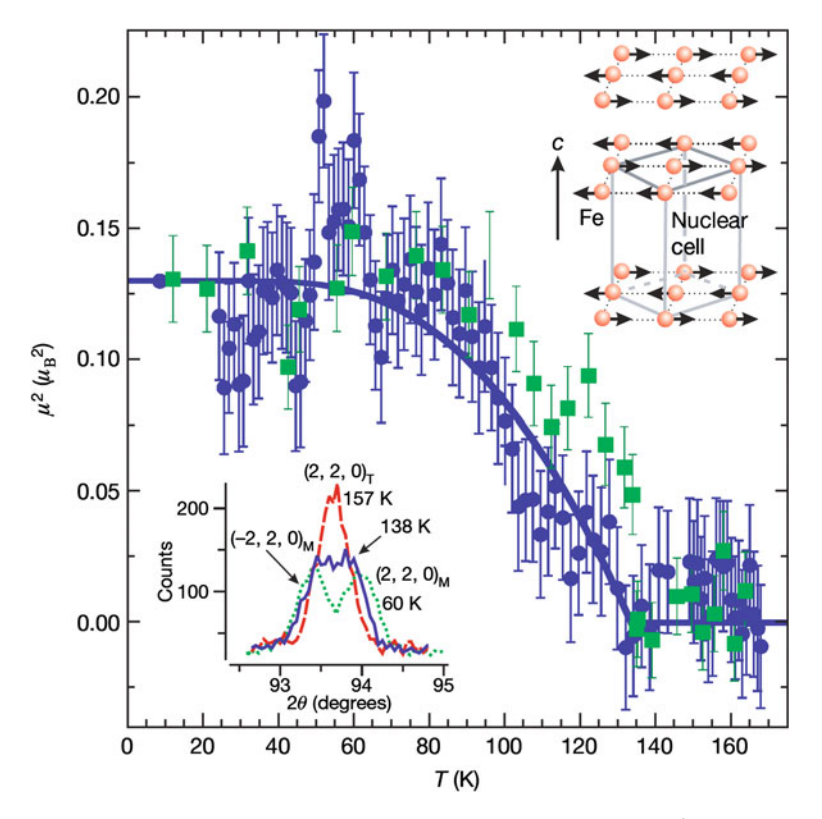


Fig. 3.7 Temperature dependence of the AFM order parameter at $Q=1.53~\text{Å}^{-1}$ determined by the neutron scattering measurements on the undoped LaFeAsO [11]. The inset in the *upper right corner* shows the AFM structure, giving a $\sqrt{2}a \times \sqrt{2}b \times \sqrt{2}c$ unit cell. Distortion of the nuclear scattering peak shown in the inset in the *lower left corner* indicates that the structural transition precedes the magnetic transition. The figure is taken from Ref. [11]

3.3 Phase Diagram 27

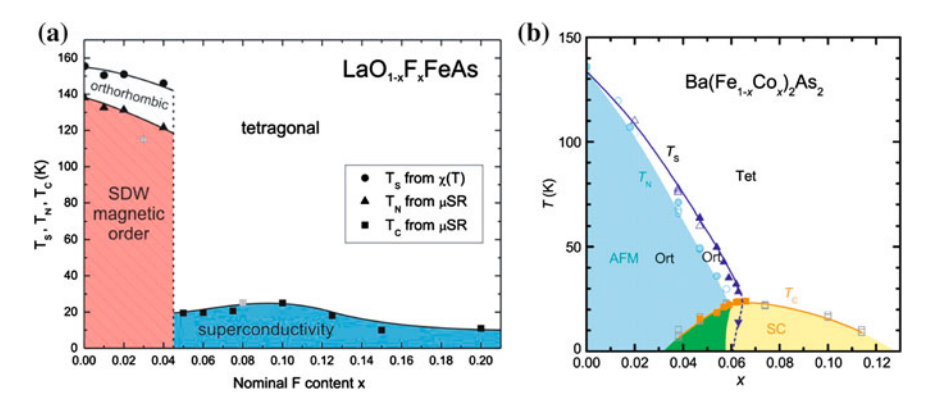


Fig. 3.8 Phase diagrams of **a** the electron-doped LaFeAsO_{1-x}F_x series obtained from the μ SR measurements [30] and **b** the electron-doped Ba(Fe_{1-x}Co_x)₂As₂ system [31]. The figures are taken from Refs. [30, 31]

which is ferromagnetically oriented with opposite spin orientations in the neighboring chains (stripe-type AFM). Both structural and antiferromagnetic transitions in the FeAs planes are suppressed by doping or applying pressure.

In Fig. 3.8a we show the phase diagram of the LaFeAsO_{1-x}F_x system, obtained from μ SR experiments [30]. It can be seen that the temperatures of the structural and magnetic transitions are clearly separated, while the superconducting phase does not overlap with the SDW phase. Similar phase diagram has been obtained for PrFeAsO_{1-x}F_x and CeFeAsO_{1-x}F_x from neutron scattering experiments, where the superconducting state also does not coexist with the SDW state. On the other hand, in the electron-doped Ba(Fe_{1-x}Co_x)₂As₂ system, x-ray, neutron scattering, and electrical resistivity measurements [31] have been performed. The obtained phase diagram is shown in Fig. 3.8b, where the coexistence of the superconducting and SDW states is observed. Thus, in the iron-based superconductors there are some differences between systems with respect to the phase diagram. The complete understanding of the phase diagram will be a subject of further studies.

3.4 Superconducting Pairing Mechanism and Types of Pairing Symmetry

So far, various theories have been proposed for the pairing mechanism in iron-based superconductors, ranging from an s_{\pm} -wave state [32, 33] with opposite signs between hole and electron pockets or s_{++} -wave state [34] without sign change, to a nodal s_{\pm} -wave [35] or d-wave [36] state and more exotic order parameters such as p-wave state [37, 38]. The marked feature of the iron-based superconductors is the multi-band nature. As confirmed by dHvA and ARPES measurements the iron-based superconductors have hole pockets at the center of the Brillouin zone (BZ)

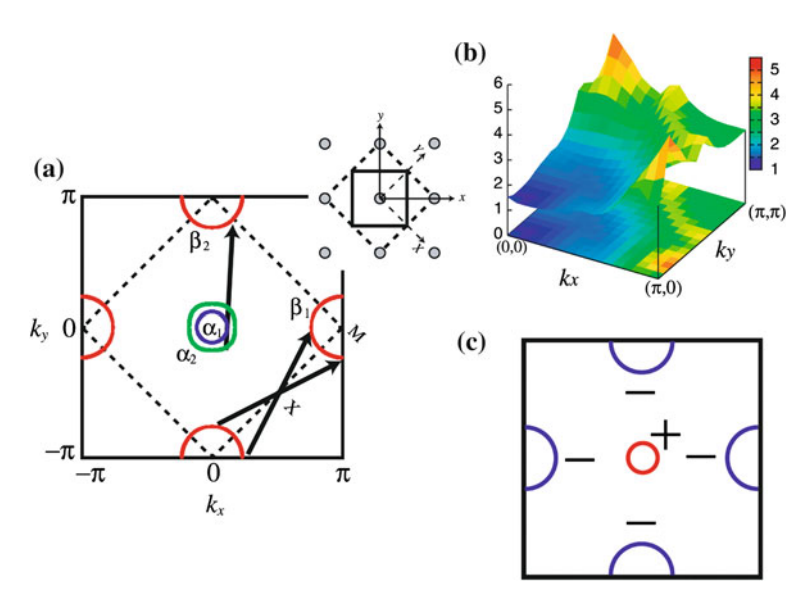


Fig. 3.9 a Fermi surface of LaFeAsO_{1-x}F $_x$ shown in the 2D unfolded BZ. The *arrows* indicate the nesting vectors. The *dashed* and *solid lines* represent the original and unfolded BZ, respectively. The inset depicts the original (*dashed lines*) and reduced (*solid lines*) unit cell in the real space. **b** Spin susceptibility χ_s based on the multi-orbital RPA calculation. **c** Schematic picture of the fully gapped s_{\pm} -wave symmetry [33]. The figure is taken from Ref. [33]

and electron pockets centered at its corners [20]. Figure 3.9a shows the Fermi surface of LaFeAsO_{1-x}F_x in the 2D unfolded Brillouin zone, which contains one Fe atom in the unit cell. The multi-orbital random-phase approximation (RPA) calculations based on the 2D Fermi surface [33] have revealed that the spin susceptibility χ_s has peaks around $(k_x, k_y) = (\pi, 0), (0, \pi)$ in the unfolded BZ, which is related to the nesting vectors between the hole and electron pockets (see Fig. 3.9a, b).

Here we consider the case where the susceptibility χ_s is strongly peaked near some wavevector Q. If we assume $U\chi_0(q) \to 0$ near the RPA instability, then the form of the singlet pairing interaction (NMR Knight-shift results rule out the spin-triplet pairing in the iron-base superconductors) can be given by [39]

$$V(k, k') = \frac{3}{2}U^2 \frac{\chi_0(q)}{1 - U\chi_0(q)},\tag{3.1}$$

where U is the Coulomb matrix element and χ_0 is the susceptibility in the absence of interactions. This implies that V(k, k') also has a peak at the wavevector Q, but is always repulsive. Since the BCS gap equation for this interaction can be given by

$$\Delta_k = -\sum_{k'} V(k, k') \frac{\Delta_{k'}}{2E_{k'}} \tanh \frac{E_{k'}}{2T},$$
 (3.2)

the order parameter Δ_k is required to have opposite signs on some regions of the Fermi surface connected by the wavevector Q,

$$\Delta_k = -\Delta_{k+O}. (3.3)$$

The sign change is a result of the anisotropic pairing interaction which is repulsive in some momentum directions. In high- T_c cuprates, where the electronic structure is essentially described by a single quasi-two-dimensional Fermi surface and χ_s is peaked at $Q=(\pi,\pi)$ [40], the sign change of order parameter leads to a $d_{\chi^2-y^2}$ -wave symmetry. In the iron-based superconductors, however, the Fermi surface has disconnected hole and electron sheets. In this case, based on the spin fluctuation theory, since the nesting vector between the hole and electron sheets leads to an s_{\pm} -wave order parameter having opposite signs between these pockets, the condition for a sign changing gap can be fulfilled without nodes as shown schematically in Fig. 3.9c.

An alternative approach to the spin fluctuation model has been proposed on the basis of the orbital fluctuation theory [34]. Based on the five-orbital Hubbard-Holstein model, the moderate electron-phonon interaction due to the Fe-ion oscillation can induce the strong orbital fluctuations by taking account of the d-orbital degree of freedom. These fluctuations give rise to the strong pairing interaction for an s-wave superconducting state without sign change (s_{++} -wave state). In this model, when the spin fluctuations are strong, the superconducting state shows a smooth crossover from the s_{\pm} -wave state to the s_{++} -wave state as impurity concentration increases (see Fig. 3.10).

Many experimental results are in good correspondence with the s_{\pm} -wave superconducting state with no nodes in the gap, but it has been pointed out that there are several discrepancies for the s_{\pm} -wave scenario. For example, although the s_{\pm} -wave state is expected to be very fragile against impurities due to the interband scattering, the superconducting state seems to be robust against impurities [41]. Moreover, in most iron-based superconductors, a broad neutron scattering resonance has been observed [42], which can be reproduced by considering the strong correlation effect via quasiparticle damping without sign change in the superconducting gap [43]. These facts indicate that a conventional s_{++} -wave state without sign change is also a possible candidate for the iron-based superconductors.

In Fig. 3.11 we summarize the candidates for the superconducting gap structure in the iron-based superconductors. The arrows represent the nesting vectors that induce the sign change of the gap. As discussed above, Fig. 3.11a, b represent the s_{++} -wave and s_{\pm} -wave state, respectively. In the spin-fluctuation scenario the nodal s_{\pm} -wave state can be caused due to the competition between the dominant Q_{he} and subdominant Q_{ee} fluctuations, whereas spin fluctuations induced by Q_{ee} may give rise to the d-wave state. Moreover, it has been pointed out that c-axis Fermi-surface dispersion could also generate horizontal line nodes. Note that the s_{++} , s_{\pm} , and nodal s_{\pm} , all have the same A_{1g} symmetry; the order parameters do not change sign under rotation by 90° (see Fig. 3.11a–c). In contrast, it changes sign in the d-wave state (see Fig. 3.11d). Therefore, nodes in Fig. 3.11c (nodal s_{\pm}) are sometimes described

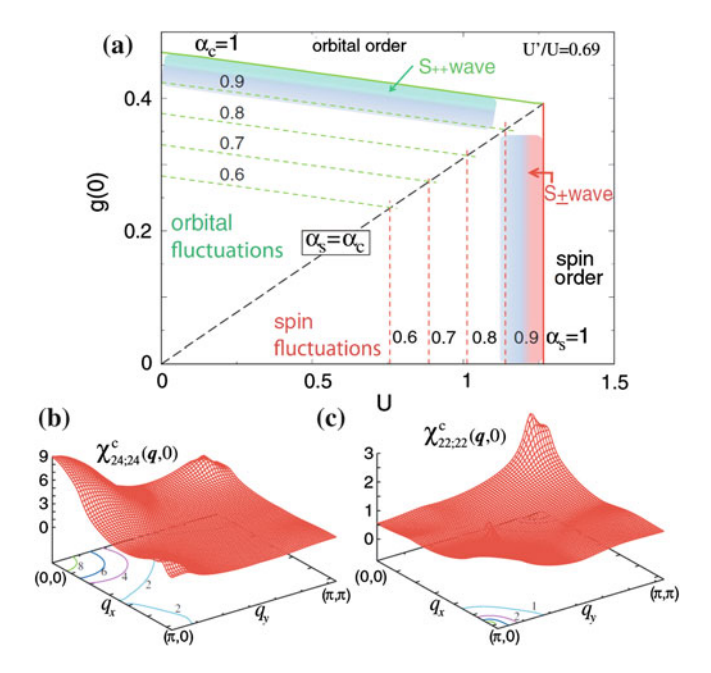


Fig. 3.10 a Phase diagram in the Hubbard-Holstein model. g(0) is the bare electron-electron interaction due to electron-phonon coupling. **b** Inter-orbital susceptibility mixing the xz and xy orbitals. **c** Intra-orbital susceptibility for the xz orbital. The figures are taken from Ref. [34]

as 'accidental' nodes, since the presence of nodes is not dictated by symmetry, but rather by the details of the pairing interaction.

So far, many theories have been proposed for the pairing symmetry in the iron-based superconductors, but a consensus for the pairing symmetry in the iron-based superconductors is still lacking. Therefore, the first experimental task is to clarify the superconducting pairing symmetry and how it varies as a function of material parameters.

3.5 Superconducting Gap Structure of Iron-Based Superconductors

In the iron-based superconductors, theories based on antiferromagnetic spin fluctuations have suggested that the nesting vector between hole and electron pockets favors the s_{\pm} -wave order parameter having opposite signs between these pockets. On the other hand, it has been argued that orbital fluctuations promote the s_{++} gap without sign change. In both cases, each Fermi surface is fully gapped, preventing low-energy excitations of quasiparticles. Indeed, in most iron-based superconductors, such as optimally doped $(Ba_{1-x}K_x)Fe_2As_2$ and $Ba(Fe_{1-x}Co_x)_2As_2$, strong

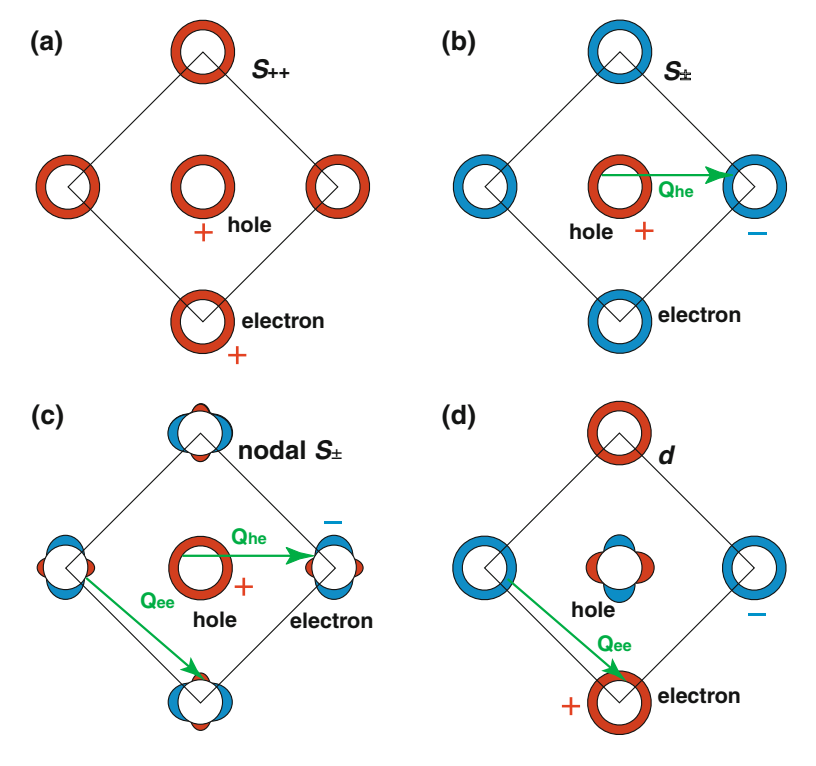


Fig. 3.11 Schematic pictures of the proposed order parameters in the iron-based superconductors represented in the 2D one-iron Brillouin zone. **a** s_{++} -wave symmetry. **b** s_{\pm} -wave symmetry. **c** Nodal s_{\pm} -wave symmetry. **d** d-wave symmetry. The *arrows* represent the nesting vectors that induce the sign change of the gap

evidence for a fully gapped superconducting state has been observed from several experiments. In contrast, low-energy quasiparticle excitations due to nodes in the gap have been revealed in this study for several iron-based superconductors, such as $BaFe_2(As_{1-x}P_x)_2$, KFe_2As_2 , and LiFeP. In this section, we mainly review the superconducting gap structure of the former materials, which were investigated in the comparatively early stage of research by several experiments, including the penetration depth, thermal conductivity, nuclear magnetic resonance (NMR), angle resolved photoemission spectroscopy (ARPES), and neutron scattering.

3.5.1 Penetration Depth

The magnetic penetration depth λ , which is a direct measure of low-energy quasiparticle excitations, is a powerful probe to elucidate the superconducting gap structure, particularly the presence or absence of nodes. In the early stage of

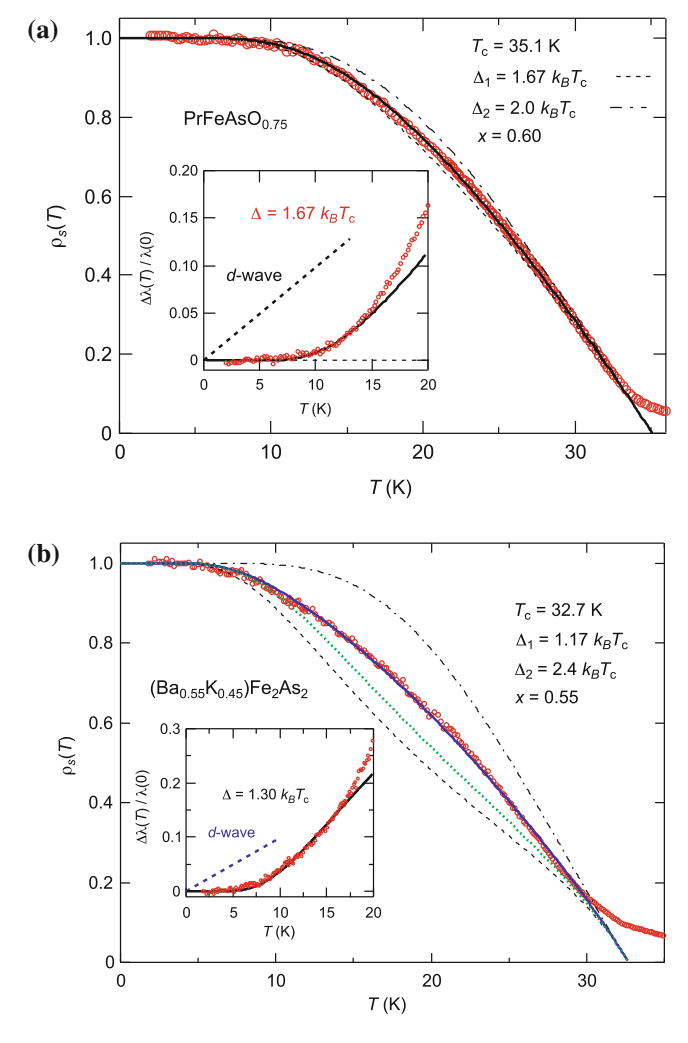


Fig. 3.12 Normalized superfluid density ρ_s for a PrFeAsO_{0.75} and b Ba_{0.55}K_{0.45}Fe₂As₂. The both data can be well fitted to the *two*-gap *s*-wave model. The *dashed lines* and *dashed-dotted lines* represent the temperature dependence expected in *s*-wave superconductors with the smaller and lager gaps shown in the main panels, respectively. The *green dotted line* in b is the single-gap fit using $1.30k_BT_c$. Above T_c , the normal-state skin-depth contribution gives a finite tail. The insets show the change in the penetration depth $\Delta\lambda(T)/\lambda(0)$ at low temperatures. The *solid lines* are fits to Eq. 2.40. The *dashed lines* represent a T-linear dependence expected in a clean d-wave superconductor [47] with maximum gap $\Delta_0 = 2.0k_BT_c$ [48]

research on iron-based superconductors, we performed the surface impedance measurements of the electron-doped $PrFeAsO_{0.75}$ [44] ('1111' system) and the hole-doped $Ba_{0.55}K_{0.45}Fe_2As_2$ [45] ('122' system) single crystals. Figure 3.12a shows the results for the electron-doped $PrFeAsO_{0.75}$. The very flat temperature dependence

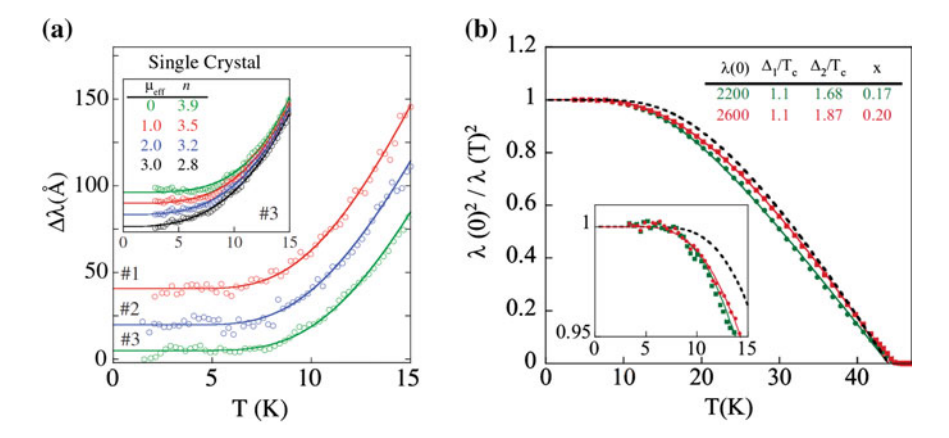


Fig. 3.13 a In-plane penetration depth of three different single crystals of SmFeAsO_{0.8}F_{0.2}. The *solid lines* are fits to Eq. 2.40. The inset shows the data for sample #3, in which paramagnetic contributions assuming the magnetic moment values listed in the inset are subtracted above 3.2 K. **b** Calculated normalized superfluid density using different assumed values for the zero temperature penetration depth $\lambda(0)$. The *solid lines* are fits to the *two* gap model. The fitting parameters are shown in the table. The dashed line represents the temperature dependence expected in a *s*-wave superconductor. The inset shows the low-temperature data. The figure is taken from Ref. [49]

of the penetration depth $\lambda(T)$ and superfluid density $\rho_s(T)$ at low temperatures are observed, which demonstrate that the finite superconducting gap opens up all over the Fermi surface. The overall temperature dependence of the superfluid density is well fitted to the simple two-gap s-wave model, which provide strong evidence for the multi-gap nature of superconductivity in this system. Very similar behaviors have been observed also in the hole-doped $Ba_{0.55}K_{0.45}Fe_2As_2$ (see Fig. 3.12b). Moreover, we have revealed that the temperature dependence of the penetration depth for $Ba_{0.55}K_{0.45}Fe_2As_2$ is very sensitive to degrees of disorder and the exponential behavior in the cleanest sample evolves toward a power-law behavior with increasing degrees of disorder [45]. Such impurity effects have also been reported in the electron-doped $Ba(Fe_{1-x}Co_x)_2As_2$ and $Ba(Fe_{1-x}Ni_x)_2As_2$ irradiated with Pb ions [46]. These results exclude the p-wave and d-wave pairing states with nodes in the gap, and are consistent with s_+ -wave state.

In the '1111' system, soon after the completion of our study on PrFeAsO_{0.75}, measurements of the penetration depth in SmFeAsO_{0.8}F_{0.2} [49] using a tunnel diode oscillator technique were reported. In Fig. 3.13, we show the temperature dependence of the penetration depth λ and the superfluid density ρ_s for SmFeAsO_{0.8}F_{0.2}. The very flat low-temperature behavior of λ is very similar to our data, suggesting fully gapped superconductivity. The overall temperature dependence of ρ_s is well fitted to the simple two-gap model with the small gap of value $\Delta_1 = 1.1 k_B T_c$ and large gap $\Delta_2 = 1.7 - 1.9 k_B T_c$, which is also consistent with our results.

The situation in the '122' system is somewhat more controversial. It has been reported that the penetration depth $\lambda(T)$ in Ba(Fe_{1-x}Co_x)₂As₂ exhibits a non-

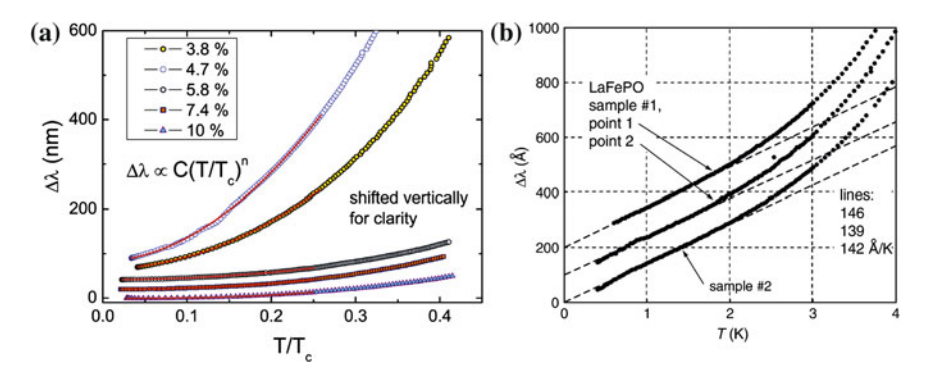


Fig. 3.14 a Changes in the penetration depth for $Ba(Fe_{1-x}Co_x)_2As_2$ at several doping levels. The lines are fits to the power-law T^n with n=2. The figure is taken from Ref. [50]. **b** Changes in the penetration depth for *three* single crystals of LaFePO. The figure is taken from Ref. [53]

exponential behavior [50], as shown in Fig. 3.14a. $\lambda(T)$ shows a power-law temperature dependence close to T^2 . In conventional s-wave superconductors, the effect of non-magnetic impurities on the temperature dependence of λ is small. On the other hand, in the s_+ -wave state, the situation is qualitatively different because interband scattering mixes the order parameters with opposite signs between hole and electron sheets, and non-magnetic impurities should act as pair-breaking centers. Therefore, the interband impurity scattering acts in the same way as a magnetic impurity in conventional s-wave superconductors. Consequently, the scattering by non-magnetic impurities in the s_+ -wave superconductors affects T_c , DOS, and the temperature dependence of λ . It has been pointed out that when the ration of the interband scattering Γ_{π} to the gap Δ becomes larger than a critical value, gapless superconductivity appears, and the exponential behavior of λ disappears [51, 52]. In the framework of this model, with increasing interband scattering, the range of the exponential behavior in $\rho_s(T)$ progressively shrinks to lower temperatures as shown in Fig. 3.15b, and ρ_s exhibits a T^2 behavior over a wide temperature range (see Fig. 3.15c). The superfluid density near the gapless regime and in the gapless regime (for $\Gamma_{\pi}/2\pi T_{c0} > 0.064$, gapless superconductivity emerges, see Fig. 3.15a) exhibits a power-law dependence T^n with $n \sim 2$ down to low temperatures.

In the P-analogue LaFePO ($T_c = 6 \, \text{K}$) [53, 54], however, a clear T-linear dependence of λ has been reported (see Fig. 3.14b). The low-temperature behavior of ρ_s in this material has been fitted to a power-law T^n with n = 1.2 down to very low temperatures. Since the material is stoichiometric, crystals are of high quality, as demonstrated by the observation of quantum oscillations [24, 25]. Therefore, such behaviors can not be explained by the above calculation. According to band-structure calculations, it has been pointed out that the d_{xy} orbital character of one of the hole sheets is very sensitive to the pnictogen height as As is substituted by P. This can cause significant changes in the spin-fluctuation spectrum and hence can change the pairing state to the nodal s_{\pm} state. In this case, the nodal gap functions are expected

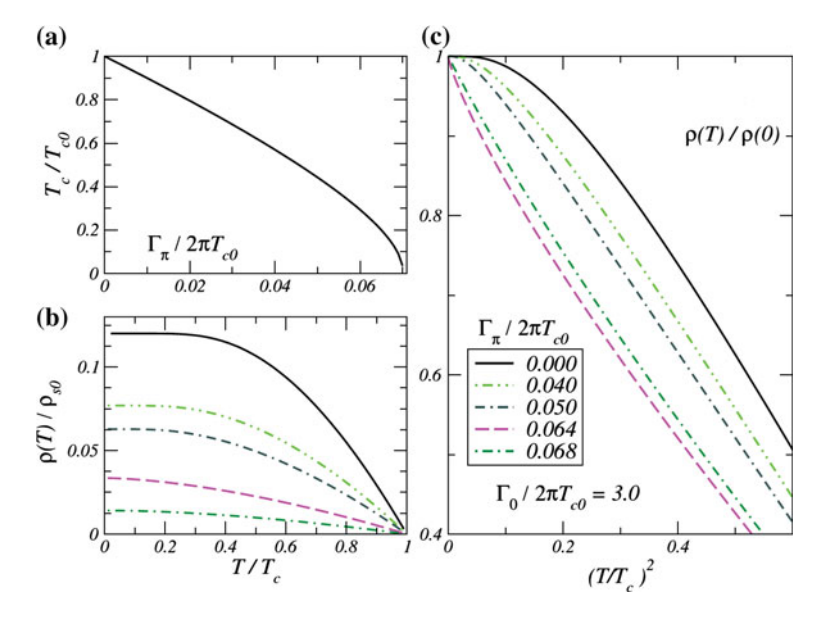


Fig. 3.15 a Suppression of T_c by interband scattering in a two-band model. b Superfluid density $\rho_s(T)$ in a dirty s_\pm -wave superconductor with intraband impurity scattering Γ_0 and interband scattering Γ_π for a fixed value of $\Gamma_0/2\pi T_{c0}=3$ and various values of $\Gamma_\pi/2\pi T_{c0}$. c The low-temperature superfluid density ρ_s as a function of T^2 . The figure is taken from Ref. [51]

to give a much lower T_c , which is consistent with the observation of a nodal pairing state in LaFePO with lower T_c .

3.5.2 Thermal Conductivity

The thermal conductivity, which is a bulk probe sensitive to the low-energy quasiparticle excitations, also provides important information on the superconducting gap structure. In the '122' system, in-plane thermal conductivity measurements have been reported in both the hole-doped (Ba_{1-x}K_x)Fe₂As₂ [55] and electron-doped Ba(Fe_{1-x}Co_x)₂As₂ [56]. Figure 3.16a shows the temperature dependence of κ/T as a function of T^2 at several magnetic fields for the optimally doped Ba_{0.6}K_{0.4}Fe₂As₂. In zero magnetic field, a small residual linear term $\kappa_0/T \sim 10~\mu\text{W/K}^2$ is observed. The normal-state thermal conductivity κ_N/T is estimated from the Wiedemann-Franz law $\kappa_N/T = L_0/\rho_0$, where ρ_0 is the electrical resistivity and $L_0 = \frac{\pi^2}{3}(\frac{k_B}{e})^2$, which gives $\kappa_N/T = 520~\mu\text{W/K}^2$ and the ratio $(\kappa_0/T)/(\kappa_N/T) \simeq 2~\%$. Such a negligible residual linear term, which immediately excludes the presence of low-energy quasiparticle excitations, is consistent with the fully gapped superconducting state.

In Fig. 3.16b we show the field dependence of κ_0/T for Ba_{0.6}K_{0.4}Fe₂As₂. In a d-wave superconductor with line nodes where the density of states has a linear

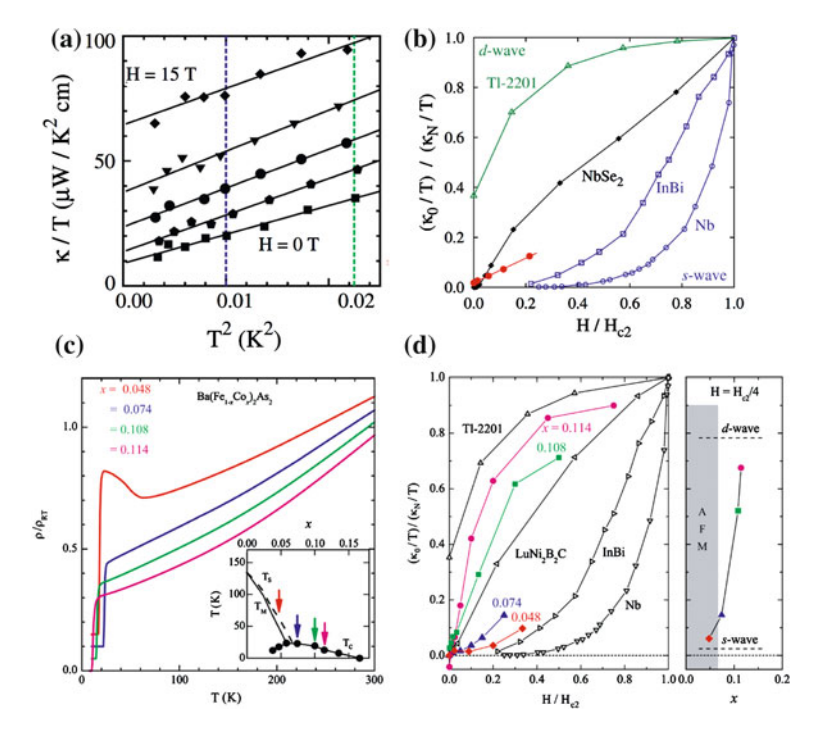


Fig. 3.16 a κ/T vs. T^2 for Ba_{0.6}K_{0.4}Fe₂As₂ at several magnetic fields (0, 1, 4, 10, and 15 T from bottom to top). Solid lines are a linear fit to each curve. Blue and green vertical dashed lines indicate T=0.1 K and T=0.15 K, respectively. **b** $(\kappa_0/T)/(\kappa_N/T)$ as a function of magnetic field H/H_{c2} for Ba_{0.6}K_{0.4}Fe₂As₂. The data for the clean and dirty isotropic s-wave superconductors Nb and InBi are shown. The data for the d-wave superconductor Tl-2201 and multi-band superconductor NbSe₂ are also plotted. **c** The in-plane resistivity for Ba(Fe_{1-x}Co_x)₂As₂ with different doping levels x. Arrows in the inset indicate the composition of the four samples. **d** Left panel: $(\kappa_0/T)/(\kappa_N/T)$ versus H/H_{c2} for Ba(Fe_{1-x}Co_x)₂As₂ with different x. Right panel: $(\kappa_0/T)/(\kappa_N/T)$ at $H/H_{c2}=0.25$ of Ba(Fe_{1-x}Co_x)₂As₂. The figures are taken from Refs. [55, 56]

energy dependence $N(E) \propto E$, N(H) increases steeply in proportion to $H^{1/2}$ due to the Doppler shift of the quasiparticle energy, which leads to a $H^{1/2}$ dependence of κ/T . In contrast, in an isotropic s-wave superconductor such as Nb, $\kappa_0(H)/T$ increases exponentially at low fields because the thermal transport relies on the tunneling of quasiparticles between localized states inside adjacent vortex cores. The field dependence for $Ba_{0.6}K_{0.4}Fe_2As_2$ is somehow stronger than that expected for an isotropic s-wave superconductor. In multi-band superconductors, such as MgB_2 and NbSe₂, the magnitude of the gap is different on two sheets of the Fermi surface. The small gap is roughly one third of the large gap in these materials, so that a field $H \simeq H_{c2}/9$ is sufficient to suppress superconductivity on the small gap, which gives rise to a moderate field dependence of κ/T . Therefore it has been suggested that the stronger field dependence observed in $Ba_{0.6}K_{0.4}Fe_2As_2$ than that in conventional

s-wave superconductors can be originated from a small gap on one Fermi surface sheet. It has also been theoretically proposed that such results can be naturally explained in terms of an anisotropic gap with deep minima on the electron or hole sheets.

In Fig. 3.16d we show the field dependence of κ_0/T in the electron-doped Ba(Fe_{1-x}Co_x)₂As₂ with different doping levels x (see Fig. 3.16c). In zero magnetic field, the residual linear terms are extremely small for all doping levels, which indicate that the fully gapped superconducting state, as in the case of the hole-doped Ba_{0.6}K_{0.4}Fe₂As₂. The slow H-dependence of κ_0/T in the optimally doped regime is consistent with the superconducting gap structure which has comparatively large gap everywhere on the Fermi surface, while the rapid increase in $\kappa_0(H)/T$ observed in the overdoped regime suggests that the superconducting gap on a certain Fermi surface sheet has a deep minimum somewhere or is very small. We note that recent c-axis thermal conductivity measurements [57] have revealed the presence of lowenergy quasiparticle excitations in the overdoped Ba(Fe_{1-x}Co_x)₂As₂. The authors have pointed out that the c-axis Fermi-surface dispersion could generate horizontal line nodes in this regime.

3.5.3 Nuclear Magnetic Resonance

So far many groups have performed NMR measurements in the iron-based superconductors. The sharp drop of the NMR Knight-shift below T_c is observed in all classes of these compounds [48, 58-63], which provides definite evidence for the spinsinglet pairing in this system. Figure 3.17 shows the typical temperature dependence of $1/T_1$ in the superconducting state for the polycrystalline samples of LaFeAsO_{0.7} and single crystals of Ba_{0.6}K_{0.4}Fe₂As₂ [63]. It can be seen that no Hebel-Slichter coherence peak, which is expected for a conventional s-wave superconductor, is observed for both compounds. On the other hand, the temperature dependence of $1/T_1$ doesn't show the same simple power-law for these materials; in LaFeAsO_{0.7} a clear T^3 dependence of $1/T_1$ in the superconducting state is observed, while the temperature dependence of $1/T_1$ for Ba_{0.6}K_{0.4}Fe₂As₂ exhibits a T^5 -like behavior, which is close to an exponential law. The sharp decrease in $1/T_1$ just below T_c and the T^3 dependence in the superconducting state can be characterized by unconventional superconductivity with line nodes such as high- T_c cuprates. Indeed, the observed T^3 dependence of $1/T_1$ for LaFeAsO_{0.7} can be reproduced by assuming a d-wave symmetry with $\Delta(\phi) = \Delta_0 \sin 2\phi$ [48]. However, the residual density of states which can be induced by a small amount of impurities is not observed.

Theoretical studies based on antiferromagnetic spin fluctuations suggest that the lack of the Hebel-Slichter peak and the observed power-law dependence of $1/T_1$ can be understood in terms of a fully gapped s_{\pm} -wave state with impurity scattering [64]. As demonstrated in Fig. 3.17, the observed $1/T_1$ data for Ba_{0.6}K_{0.4}Fe₂As₂ and LaFeAsO_{0.7} are consistently explained by a two-gap s_{\pm} -wave model with impu-

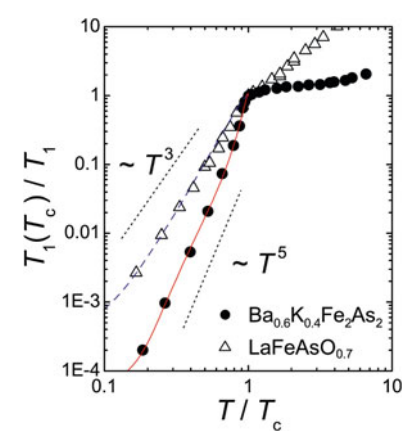


Fig. 3.17 Temperature dependence of $1/T_1$ normalized by the value at T_c for Ba_{0.6}K_{0.4}Fe₂As₂ and LaFeAsO_{0.7}. The solid and dashed lines represent the fits to the anisotropic two-gap s_{\pm} -wave model, in which one of the gaps is anisotropic and the other isotropic for Ba_{0.6}K_{0.4}Fe₂As₂ and LaFeAsO_{0.7}, respectively. The figure is taken from Ref. [63]

rity scattering. The $1/T_1$ in the s_{\pm} -wave state should decrease exponentially at low temperatures in the clean limit, which has been indeed observed in Ba_{0.6}K_{0.4}.

In the s_{\pm} -wave state, the Hebel-Slichter coherence peak can be severely suppressed by the existence of the sign-inverse superconducting gaps between hole and electron sheets. For simplicity, we assume that the superconducting gaps have the same magnitude with opposite sign, $\Delta_{\rm el} = -\Delta_{\rm hole} = \Delta_0$. We further assume that the main contribution to $1/T_1$ comes from interband interactions. Then, we obtain

$$\frac{1}{T_1} \propto \int_{\Delta}^{\infty} \left(1 + \frac{\Delta_{\text{el}} \Delta_{\text{hole}}}{EE'} \right) \frac{E^2}{E^2 - \Delta_0^2} f(E) (1 - f(E')) dE \tag{3.4}$$

$$= \int_{\Delta}^{\infty} \frac{E^2 + \Delta_0^2}{E^2 - \Delta_0^2} \operatorname{sech}^2\left(\frac{E}{2T}\right) dE$$
 (3.5)

$$= \int_{A}^{\infty} \operatorname{sech}^{2}\left(\frac{E}{2T}\right) dE, \tag{3.6}$$

where E and E' represent the quasiparticle energy in the superconducting state on the hole and electron bands, respectively. As temperature is lowered, the integral decreases monotonically, which leads to the absence of Hebel-Slichter coherence peak. The same result can be reproduced for a more general s_{\pm} case of $|\Delta_k| \neq |\Delta_{k'}|$ [64].

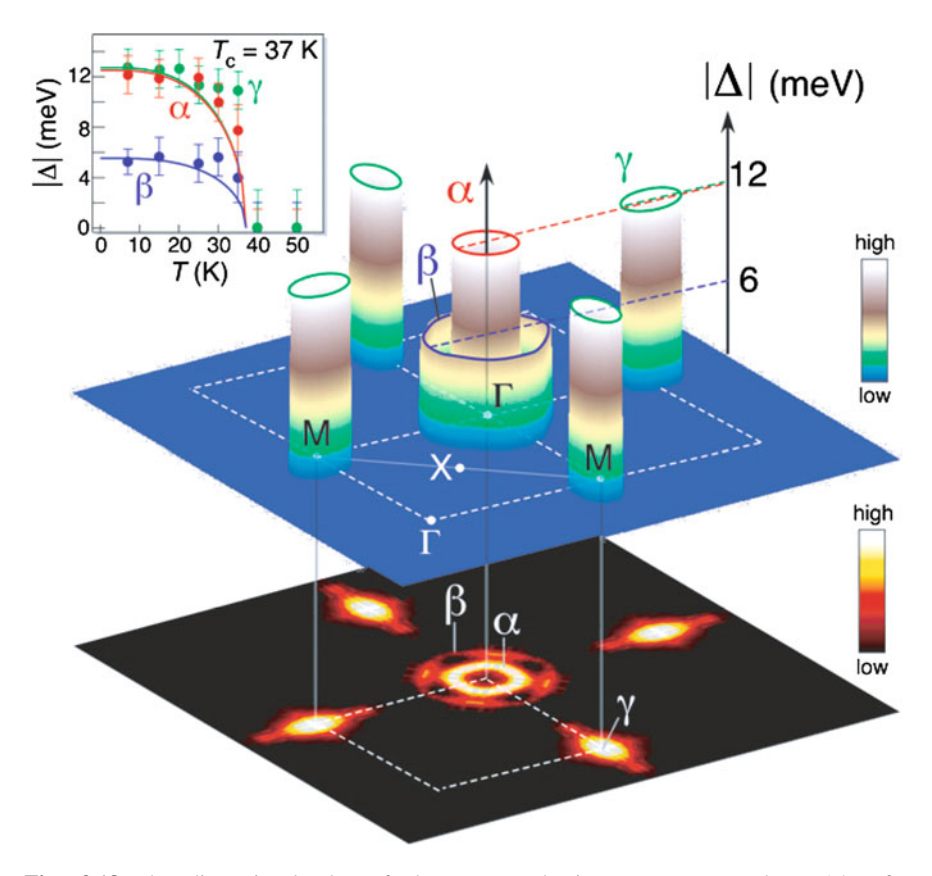


Fig. 3.18 Thee-dimensional plot of the superconducting gaps measured at $15\,\mathrm{K}$ for $\mathrm{Ba_{0.6}K_{0.4}Fe_2As_2}$. The observed *three* Fermi surfaces are shown at the *bottom* as an intensity plot. The inset depicts the temperature dependence of these *three* gaps. The figure is taken from Ref. [65]

3.5.4 Angle Resolved Photoemission Spectroscopy (ARPES)

Figure 3.18 shows the results of the ARPES measurements for Ba_{0.6}K_{0.4}Fe₂As₂ [65]. Two hole pockets at the center of the Brillouin zone (BZ) and one electron pocket centered at its corners are observed. As shown in Fig. 3.18, nearly isotropic and nodeless superconducting gaps with different values open at T_c on all three observed Fermi surfaces; a large gap ($\Delta \sim 12 \, \mathrm{meV}$) on the inner hole pocket around the Γ point and electron pocket centered at the BZ corners, and a small gap ($\Delta \sim 6 \, \mathrm{meV}$) on the outer hole sheet around the Γ point. Thus, the nature of multi-gap superconductivity is observed. Since the same and large superconducting gap on the hole and electron sheets, which are connected by the (π , 0) SDW vector, Ding et al. have suggested that the pairing mechanism in this system originates from the interband interaction between these two nested Fermi surfaces. Similar experimental results have been

reported from different groups. However, recent bulk-sensitive laser-ARPES measurements [66] have been revealed that the magnitudes of the superconducting gaps on the observed three hole sheets at the Z point are identical. The authors have pointed out that the orbital-independent superconducting gap magnitude implies the important role of orbital degrees of freedom on the electron-pairing mechanism. One possibility of the discrepancy between these experiments is that the electronic structure at the surface is different from that of the bulk. The bulk and surface band structures of $BaFe_2As_2$ have been calculated by density functional theory, which reveal that the surface bands include an additional pocket of xy orbital character at the Fermi level. Further studies will be required for the complete understanding of the surface problem.

3.5.5 Neutron Scattering

Neutron scattering is a powerful tool to measure the dynamical spin susceptibility $\chi_s(q,\omega)$. For the local interaction U_s , χ_s can be given by

$$\chi_s(q,\omega) = (I - U_s \chi_0(q,\omega))^{-1} \chi_0(q,\omega), \tag{3.7}$$

where I is a unit matrix in the orbital space and $\chi_0(q, \omega)$ is a 4×4 matrix formed by the interband and intraband bare susceptibilities. Importantly, $\chi_0(q, \omega)$ describes particle-hole excitations, which are gapped below approximately $2\Delta_0$; $\text{Im}\chi_0(q, \omega)$ becomes nonzero at T=0 above this threshold $2\Delta_0$. The term arising from the anomalous Green's functions is proportional to

$$\sum_{k} \left(1 - \frac{\Delta_k \Delta_{k+q}}{E_k E_{k+q}} \right). \tag{3.8}$$

At the Fermi level, $E_k = \sqrt{\varepsilon_k^2 + \Delta_k^2} = |\Delta_k|$. If Δ_k and Δ_{k+q} have the same sign, the coherence factor in Eq. 3.8 vanishes, which leads to a smooth increase of the magnetic response above the threshold value of $\Omega_c = \min(|\Delta_k| + |\Delta_{k+q}|)$. In the case of $\operatorname{sgn}\Delta_k \neq \operatorname{sgn}\Delta_{k+q}$ the coherence factor is nonzero and the imaginary part of χ_0 shows a discontinuous jump at Ω_c . In this case, the real part exhibits a logarithmic singularity, which results in the divergence of $\operatorname{Im}\chi(q,i\omega_m)$. Such an enhancement of the spin susceptibility is the so-called spin resonance peak.

The scattering between nearly nested hole and electron Fermi surfaces in ironbased superconductors causes a peak in the normal state magnetic susceptibility near $q = Q = (\pi, 0)$. In isotropic s-wave superconductors, since $\operatorname{sgn}\Delta_k = \operatorname{sgn}\Delta_{k+Q}$, there is no resonance peak. In contrast, in the case of s_{\pm} -wave superconductors, Q connects Fermi surface sheets with mostly opposite signs of the gaps. This fulfills the resonance condition for the interband susceptibility, and a well-defined spin resonance peak is formed. Moreover, the intraband bare susceptibilities are small at

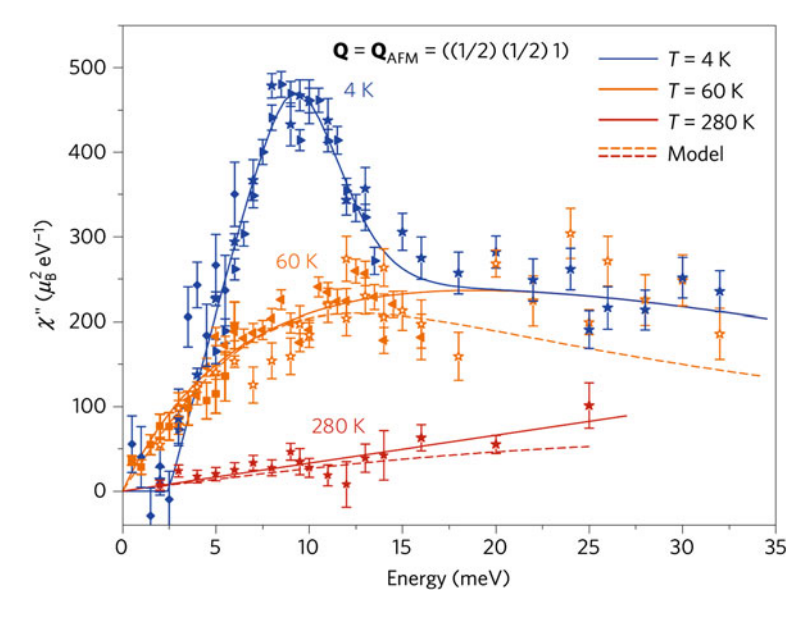


Fig. 3.19 Imaginary part of the spin susceptibility $\chi(Q_{\rm AFM},\omega)$ in the superconducting $(T=4\,{\rm K})$ and the normal state $(T=60~{\rm and}~280~{\rm K})$ for the optimally doped BaFe_{1.85}Co_{0.15}As₂. The figure is taken from Ref. [67]

this wavevector Q because there are no regions connected by the intraband scattering with wavevector Q. Therefore, a single pole will occur for all components of the spin susceptibility at $\Omega \leq \Omega_c$. Figure 3.19 shows the imaginary part of the spin susceptibility $\chi(Q_{\rm AFM},\omega)$ in the superconducting state $(T=4\,{\rm K})$ and normal state $(T=60\,{\rm and}\,280\,{\rm K})$ [67] for the optimally doped BaFe_{1.85}Co_{0.15}As₂. In the superconducting state, a clear resonance peak is observed. The obtained value of $\Omega_{\rm res}/2\Delta_0=0.79$ is in good agreement with the predictions for the s_\pm -wave gap. However, it has been pointed out that most iron-based superconductors show a broader neutron scattering resonance [42, 67] than that expected in the s_\pm -wave state. Onari et al. [43] have suggested that the experimental results can be reproduced by considering the strong correlation effect via quasiparticle damping without sign change in the superconducting gap $(s_{++}$ -wave). Thus, a consensus for the pairing symmetry in the iron-based superconductors is still lacking.

References

- 1. Y. Kamihara, T. Watanabe, M. Hirano, H. Hosono, J. Am. Chem. Soc. 130, 3296 (2008)
- 2. H. Takahashi, K. Igawa, K. Arii, Y. Kamihara, M. Hirano, H. Hosono, Nature 453, 376 (2008)
- 3. X.H. Chen, T. Wu, G. Wu, R.H. Liu, H. Chen, D.F. Fang, Nature 453, 761 (2008)
- 4. H.H. Wen, G. Mu, L. Fang, H. Yang, X.Y. Zhu, Eur. Phys. Lett. 82, 17009 (2008)

- Z.A. Ren, J. Yang, W. Lu, W. Yi, X.L. Shen, Z.G. Li, G.C. Che, X.L. Dong, L.L. Sun, F. Zhou, Z.X. Zhao, Europhys. Lett. 82, 57002 (2008)
- G.F. Chen, Z. Li, D. Wu, G. Li, W.Z. Hu, J. Dong, P. Zheng, J.L. Luo, N.L. Wang, Phys. Rev. Lett. 100, 247002 (2008)
- Z.A. Ren, J. Yang, W. Lu, W. Yi, G.C. Che, X.L. Dong, L.L. Sung, Z.X. Zhao, Mater. Res. Innov. 12, 106 (2008)
- 8. R.H. Liu, G. Wu, T. Wu, D.F. Fang, H. Chen, S.Y. Li, K. Liu, Y.L. Xie, X.F. Wang, R.L. Yang, L. Ding, C. He, D.L. Feng, X.H. Chen, Phys. Rev. Lett 101, 087001 (2008)
- 9. H. Kito, H. Eisaki, A. Iyo, J. Phys. Soc. Jpn. 77, 063707 (2008)
- C. Wang, L. Li, S. Chi, Z. Zhu, Z. Ren, Y. Li, Y. Wang, X. Lin, Y. Luo, S. Jiang, X. Xu, G. Cao, Z. Xu, Europhys. Lett. 83, 67006 (2008)
- 11. C. de la Cruz, Q. Huang, J.W. Lynn, J. Li, W. Ratcliff II, J.L. Zarestky, H.A. Mook, G.F. Chen, J.L. Luo, N.L. Wang, P. Dai, Nature 453, 899 (2008)
- 12. T. Mine, H. Yanagi, T. Kamiya, Y. Kamihara, M. Hirano, H. Hosono, Sol. State Comm. 147, 111 (2008)
- 13. M. Rotter, M. Tegel, D. Johrendt, Phys. Rev. Lett. 101, 107006 (2008)
- X.C. Wang, Q.Q. Liu, Y.X. Lv, W.B. Gao, L.X. Yang, R.C. Yu, F.Y. Li, C.Q. Jin, Solid State Comm. 148, 538 (2008)
- J.H. Tapp, Z. Tang, B. Lv, K. Sasmal, B. Lorenz, C.W. Chu, A.M. Guloy, Phys. Rev. B 78, 060505 (2008)
- F.C. Hsu, J.Y. Luo, K.W. Yeh, T.K. Chen, T.W. Huang, P.M. Wu, Y.C. Lee, Y.L. Huang, Y.Y. Chu, D.C. Yan, M.K. Wu, Proc. Natl. Acad. Sci. U.S.A. 105, 14262 (2008)
- H. Ogino, Y. Katsura, S. Horii, K. Kishio, J. Shimoyama, Supercond. Sci. Technol. 22, 085001 (2009)
- 18. L. Boeri, O.V. Dolgov, A.A. Golubov, Phys. Rev. Lett. **101**, 026403 (2008)
- 19. G. Xu, W. Ming, Y. Yao, X. Dai, S.C. Zhang, Z. Fang, Europhys. Lett. 82, 67002 (2008)
- 20. D.J. Singh, Phys. Rev. B 78, 094511 (2008)
- 21. A. Subedi, L. Zhang, D.J. Singh, M.H. Du, Phys. Rev. B 78, 134514 (2008)
- 22. D.J. Singh, M.H. Du, Phys. Rev. Lett. 100, 237003 (2008)
- C. Liu, T. Kondo, M.E. Tillman, R. Gordon, G.D. Samolyuk, Y. Lee, C. Martin, J.L. McChesney, S. Bud'ko, M.A. Tanatar, E. Rotenberg, P.C. Canfield, R. Prozorov, B.N. Harmon, A. Kaminski, Physica C 469, 491 (2009)
- 24. A.I. Coldea, J.D. Fletcher, A. Carrington, J.G. Analytis, A.F. Bangura, J.H. Chu, A.S. Erickson, I.R. Fisher, N.E. Hussey, R.D. McDonald, Phys. Rev. Lett. 101, 216402 (2008)
- 25. H. Sugawara, R. Settai, Y. Doi, H. Muranaka, K. Kitayama, H. Yamagami, Y. Onuki, J. Phys. Soc. Jpn. 77, 113711 (2008)
- H. Shishido, A.F. Bangura, A.I. Coldea, S. Tonegawa, K. Hashimoto, S. Kasahara, P.M.C. Rourke, H. Ikeda, T. Terashima, R. Settai, Y. Onuki, D. Vignolles, C. Proust, B. Vignolle, A. McCollam, Y. Matsuda, T. Shibauchi, A. Carrington, Phys. Rev. Lett. 104, 057008 (2010)
- T. Terashima, N. Kurita, M. Tomita, K. Kihou, C.-H. Lee, Y. Tomioka, T. Ito, A. Iyo, H. Eisaki, T. Liang, M. Nakajima, S. Ishida, S. Uchida, H. Harima, S. Uji, Phys. Rev. Lett. 107, 176402 (2011)
- 28. J. Dong, H.J. Zhang, G. Xu, Z. Li, G. Li, W.Z. Hu, D. Wu, G.F. Chen, X. Dai, J.L. Luo, Z. Fang, N.L. Wang, Europhys. Lett. **83**, 27006 (2008)
- H. Chen, Y. Ren, Y. Qiu, W. Bao, R.H. Liu, G. Wu, T. Wu, Y.L. Xie, X.F. Wang, Q. Huang, X.H. Xhen, Europhys. Lett. 85, 17006 (2009)
- H. Luetkens, H.H. Klauss, M. Kraken, F.J. Litterst, T. Dellmann, R. Klingeler, C. Hess, R. Khasanov, A. Amato, C. Baines, J.H. Borrero, N. Leps, A. Kondrat, G. Behr, J. Werner, B. Buchner, Nat. Mater. 8, 305 (2009)
- S. Nandi, M.G. Kim, A. Kreyssig, R.M. Fernandes, D.K. Pratt, A. Thaler, N. Ni, S.L. Bud'ko, P.C. Canfield, J. Schmalian, R.J. McQueeney, A.I. Goldman, Phys. Rev. Lett 104, 057006 (2010)
- 32. I.I. Mazin, D.J. Singh, M.D. Johannes, M.H. Du, Phys. Rev. Lett. 101, 057003 (2008)

References 43

 K. Kuroki, S. Onari, R. Arita, H. Usui, Y. Tanaka, H. Kontani, H. Aoki, Phys. Rev. Lett. 101, 087004 (2008)

- 34. H. Kontani, S. Onari, Phys. Rev. Lett. 104, 157001 (2010)
- 35. K. Kuroki, H. Usui, S. Onari, R. Arita, H. Aoki, Phys. Rev. B 79, 224511 (2009)
- 36. H. Ikeda, R. Arita, J. Kunes, Phys. Rev. B 82, 024508 (2010)
- 37. X. Dai, Z. Fang, Y. Zhou, F.C. Zhang, Phys. Rev. Lett. 101, 057008 (2008)
- 38. P.A. Lee, X.G. Wen, Phys. Rev. B 78, 144517 (2008)
- 39. S. Nakajima, Prog. Theor. Phys. **50**, 1101 (1973)
- 40. D.J. Scalapino, Phys. Rep. **250**, 329 (1995)
- A. Kawabata, S.C. Lee, T. Moyoshi, Y. Kobayashi, M. Sato, J. Phys. Soc. Jpn. 77, 103704 (2008)
- 42. A.D. Christianson, E.A. Goremychkin, R. Osborn, S. Rosenkranz, M.D. Lumsden, C.D. Malliakas, I.S. Todorov, H. Claus, D.Y. Chung, M.G. Kanatzidis, R.I. Bewley, T. Guidi, Nature (London) 456, 930 (2008)
- 43. S. Onari, H. Kontani, M. Sato, Phys. Rev. B 81, 060504(R) (2010)
- 44. K. Hashimoto, T. Shibauchi, S. Kasahara, K. Ikada, S. Tonegawa, T. Kato, R. Okazaki, C.J. van der Beek, M. Konczykowski, H. Takeya, K. Hirata, T. Terashima, Y. Matsuda, Phys. Rev. Lett. **102**, 207001 (2009)
- K. Hashimoto, T. Shibauchi, S. Kasahara, K. Ikada, T. Kato, R. Okazaki, C.J. van der Beek, M. Konczykowski, H. Takeya, K. Hirata, T. Terashima, Y. Matsuda, Phys. Rev. Lett. 102, 207001 (2009)
- H. Kim, R.T. Gordon, M.A. Tanatar, J. Hua, U. Welp, W.K. Kwok, N. Ni, S.L. Bud'ko, P.C. Canfield, A.B. Vorontsov, R. Prozorov, Phys. Rev. B 82, 060518 (2010)
- 47. W.N. Hardy, D.A. Bonn, D.C. Morgan, R. Liang, K. Zhang, Phys. Rev. Lett. 70, 3999 (1993)
- 48. Y. Nakai, K. Ishida, Y. Kamihira, M. Hirano, H. Hosono, J. Phys. Soc. Jpn. 77, 073701 (2008)
- L. Malone, J.D. Fletcher, A. Serafin, A. Carrington, N.D. Zhigadlo, Z. Bukowski, S. Katrych, J. Karpinski, Phys. Rev. B 79, 140501(R) (2009)
- R.T. Gordon, C. Martin, H. Kim, N. Ni, M.A. Tanatar, J. Schmalian, I.I. Mazin, S.L. Bud'ko, P.C. Canfield, R. Prozorov, Phys. Rev. B 79, 100506(R) (2009)
- 51. A.B. Vorontsov, M.G. Vavilov, A.V. Chubukov, Phys. Rev. B 79, 140507(R) (2009)
- 52. Y. Bang, Europhys. Lett. **86**, 47001 (2009)
- C.W. Hicks, T.M. Lippman, M.E. Huber, J.G. Analytis, J.-H. Chu, A.S. Erickson, I.R. Fisher, K.A. Moler, Phys. Rev. Lett. 103, 127003 (2009)
- J.D. Fletcher, A. Serafin, L. Malone, J.G. Analytis, J.-H. Chu, A.S. Erickson, I.R. Fisher, A. Carrington, Phys. Rev. Lett. 102, 147001 (2009)
- X.G. Luo, M.A. Tanatar, J.-Ph. Reid, H. Shakeripour, N. Doiron-Leyraud, N. Ni, S.L. Bud'ko,
 P.C. Canfield, H. Luo, Z. Wang, H.-H. Wen, R. Prozorov, L. Taillefer, Phys. Rev. B 80, 140503(R) (2009)
- M.A. Tanatar, J.P. Reid, H. Shakeripour, X.G. Luo, N. Doiron-Leyraud, N. Ni, S.L. Bud'ko,
 P.C. Canfield, R. Prozorov, L. Taillefer, Phys. Rev. Lett. 104, 067002 (2010)
- J.P. Reid, M.A. Tanatar, X.G. Luo, H. Shakeripour, N.D. Leyraud, N. Ni, S.L. Bud'ko, P.C. Canfield, R. Prozorov, L. Taillefer, Phys. Rev. B 82, 064501 (2010)
- H.J. Grafe, D. Paar, G. Lang, N.J. Curro, G. Behr, J. Werner, J.H. Borrero, C. Hess, N. Leps, R. Klingeler, B. Buechner, Phys. Rev. Lett. 101, 047003 (2008)
- K. Matano, Z.A. Ren, X.L. Ding, X.L. Dong, L.L. Sun, Z.X. Zhao, G.G. Zheng, Europhys. Lett. 83, 570001 (2008)
- H. Mukuda, N. Terasaki, H. Kinouchi, M. Yashima, Y. Kitaoka, S. Suzuki, S. Miyasaka, S. Tajima, K. Miyazawa, P.M. Shirage, H. Kito, H. Eisaki, A. Iyo, J. Phys. Soc. Jpn. 77, 093704 (2008)
- F.L. Ning, K. Ahilan, T. Imai, A.S. Sefat, R. Jin, M.A. McGuire, B.C. Sales, D. Mandrus, J. Phys. Soc. Jpn. 77, 103705 (2008)
- 62. H. Kotegawa, S. Masaki, Y. Awai, H. Tou, Y. Mizugichi, Y. Takano, J. Phys. Soc. 77, 11 (2008)
- 63. M. Yashima, H. Nishimura, H. Mukuda, Y. Kitaoka, K. Miyazawa, P.M. Shirage, K. Kiho, H. Kito, H. Eisaki, A. Iyo, J. Phys. Soc. Jpn. **78**, 103702 (2009)

- D. Parker, O.V. Dolgov, M.M. Korshunov, A.A. Golubov, I.I. Mazin, Phys. Rev. B 78, 134524 (2008)
- H. Ding, P. Richard, K. Nakayama, T. Sugawara, T. Arakane, Y. Sekiba, A. Takayama, S. Souma, T. Sato, T. Takahashi, Z. Wang, X. Dai, Z. Fang, G.F. Chen, J.L. Luo, N.L. Wang, Europhys. Lett. 83, 47001 (2008)
- 66. T. Shimojima, F. Sakaguchi, K. Ishizaka, Y. Ishida, T. Kiss, M. Okawa, T. Togashi, C.-T. Chen, S. Watanabe, M. Arita, K. Shimada, H. Namatame, M. Taniguchi, K. Ohgushi, S. Kasahara, T. Terashima, T. Shibauchi, Y. Matsuda, A. Chainani, S. Shin, Science 332, 564 (2011)
- 67. D.S. Inosov, J.T. Park, P. Bourges, D.L. Sun, Y. Sidis, A. Schneidewind, K. Hradil, D. Haug, C.T. Lin, B. Keimer, V. Hinkov, Nature Phys. 6, 178 (2009)

Chapter 4 Experimental Method

Abstract Even though the absolute penetration depth of a superconductor is several thousands of Angstroms, at low temperatures its length can change by only a few Angstroms. Therefore extremely sensitive experimental techniques are required to perform accurate measurements of the penetration depth. In this study, we have used two different techniques: the tunnel diode oscillator technique provides very precise measurements of the relative change in the penetration depth, $\Delta \lambda = \lambda(T) - \lambda(0)$, while the microwave cavity perturbation technique gives important information on its absolute value, $\lambda(T)$. In both techniques, we measure the perturbative change caused by the introduction of a sample into a coil or cavity. Through this study, the tunnel diode oscillator technique has also been extended to obtain the absolute value of the penetration depth. We can obtain $\lambda(0)$ from the tunnel diode oscillator technique by measuring a superconductor whose surfaces are coated with a thin film of aluminum having a lower critical temperature ($T_c = 1.2 \,\mathrm{K}$) and a known value of $\lambda(0) = 55$ nm. In this chapter, we describe the details of experimental principles and methods to extract the magnetic penetration depth from the tunnel diode oscillator and microwave cavity perturbation techniques.

Keywords Tunnel diode oscillator technique · Microwave cavity perturbation technique · Aluminium coating method · Magnetic penetration depth

4.1 Tunnel Diode Oscillator Technique

4.1.1 Principle

The magnetic penetration depth measurements have been performed mainly using the tunnel diode oscillator (TDO) [1] with a noise level of one part in 10⁹ in the ³He-⁴He dilution refrigerator or ³He cryostat. The tunnel diode oscillator technique [2, 3] is able to extract the relative change of the penetration depth with temperature,

 $\Delta\lambda(T) = \lambda(T) - \lambda(0)$. The TDO operates with an extremely small ac probe field $(H_{ac} < 10 \,\text{mOe})$ so that the sample is always in the Meissner state. To measure the inplane penetration depth, H_{ac} is applied along the crystal c axis, which generates the supercurrents in the plane. The change in the resonant frequency Δf is proportional to the change in the penetration depth $\Delta\lambda$, $\Delta f = G\Delta\lambda$. The calibration factor G is determined from the geometry of the sample [4].

Firstly, in this subsection, we introduce the linear relationship between the magnetic penetration depth and the resonant frequency of the LC circuit, $\Delta f = G\Delta\lambda$ [5]. Secondly, we derive the expression for the relationship between the calibration factor G and the sample geometry [4].

In general, when a current I flows in a coil, the total energy stored inside the coil can be given by

$$U = \frac{1}{2}LI^2,\tag{4.1}$$

where L is the inductance of the coil. This energy is also equal to the total magnetic energy inside the coil,

$$U = \frac{1}{2} \int B \cdot H d^3 r. \tag{4.2}$$

The energy difference between the empty coil and the coil containing the sample is given by

$$\Delta U = \frac{1}{2} \int (B_s \cdot H_s - B_0 \cdot H_0) d^3 r, \tag{4.3}$$

where the subscripts '0' and 's' denote before and after the insertion of the sample, respectively. Equation 4.3 can be written in terms of an integral only over the sample as follows [6]:

$$\Delta U = \frac{1}{2} \int_{V_s} \mu_0 M \cdot H_0 d^3 r, \tag{4.4}$$

where M is the magnetization in the sample and V_s is the sample volume. Therefore the change in the inductance is given by

$$(L_s - L_0)I^2 = \int_{V_s} \mu_0 M \cdot H_0 d^3 r. \tag{4.5}$$

The current I can be eliminated by assuming a uniform field B_0 inside the empty coil and zero field outside. Then we obtain

$$\frac{1}{2}L_0I^2 = \frac{B_0^2V_c}{2\mu_0},\tag{4.6}$$

where V_c is the coil volume. If the sample shape is ellipsoidal and the volume is small enough so that the sample can be identified with part of the coil, then the magnetization inside the coil should be uniform,

$$M = \frac{\chi}{1 + N\chi} H_0,\tag{4.7}$$

where N is the demagnetization factor and χ is the linear susceptibility. Hence we obtain

$$\frac{L_s - L_0}{L_0} = \frac{\chi}{1 + N\chi} \frac{V_s}{V_c}.$$
 (4.8)

Since we are assuming a small variation in the total inductance before and after the insertion of the sample, the change in the resonant frequency $f = 1/(2\pi\sqrt{LC})$ can be expanded to the first order in ΔL , which leads to

$$\frac{f_0 - f_s}{f_0} = \frac{1}{2} \frac{L_s - L_0}{L_0}. (4.9)$$

Therefore the resonant frequency and the susceptibility are linked by the following relation:

$$\frac{f_0 - f_s}{f_0} = \frac{\chi}{2(1 + \chi N)} \frac{V_s}{V_c}.$$
 (4.10)

Since we are interested in a linear relationship between the resonant frequency and the susceptibility, we linearize Eq. 4.10. The factor χ in the denominator of Eq. 4.10 is taken to be equal to -1, which is the value for the perfect Meissner screening. Hence we obtain

$$\frac{f_0 - f_s}{f_0} = \frac{\chi}{2(1 - N)} \frac{V_s}{V_c}.$$
 (4.11)

Here we consider an infinite slab with thickness of 2d placed in a uniform magnetic field H_0 applied parallel to its surface. The boundary conditions impose the following equation on Eq. 2.28:

$$B(\pm d) = H_0. \tag{4.12}$$

Therefore the solution of Eq. 2.28 can be written as [7]

$$B(z) = H_0 \frac{\cosh(z/\lambda)}{\cosh(d/\lambda)}.$$
 (4.13)

Let us now derive the susceptibility χ from Eq. 4.13. The magnetization M of the slab can be calculated from [8]

$$\mu_0 M = \frac{1}{2d} \int_{-d}^{d} (B - H_0) dz, \tag{4.14}$$

which gives

$$M = -\frac{H_0}{\mu_0} \left(1 - \frac{\lambda}{d} \tanh \frac{d}{\lambda} \right). \tag{4.15}$$

Thus the susceptibility $\chi = \mu_0 M/H_0$ is given by

$$-\chi = 1 - \frac{\lambda}{d} \tanh \frac{d}{\lambda} \tag{4.16}$$

In our measurements, the magnetic field is almost applied perpendicular to the sample surface, which introduces an additional factor 1/(1-N) as mentioned above. This factor can be included into the definition of $\chi = \frac{\mu_0 M}{H_0/(1-N)}$. Equation 4.16 applies only to an infinite slab. For a $2 \times 2 w$ slab with thickness of 2d and the magnetic field perpendicular to the plane, the field penetrates into the lateral directions. Therefore the quantity d in Eq. 4.16 must be replaced by the effective dimension of the sample, R_{3D} , which is of the same order of magnitude as w. A semi-analytical approach for the effective dimension $R_{3D}[4]$ gives the approximate solution for thin slabs $(2d \ll w)$ as follows:

$$R_{3D} = \frac{w}{2f(2d/w)},\tag{4.17}$$

where the correction factor $f\left(\frac{2d}{w}\right)$ is given by

$$f\left(\frac{2d}{w}\right) = 1 + \left[1 + \left(\frac{2d}{w}\right)^2\right] \arctan\left(\frac{w}{2d}\right) - \frac{2d}{w}.$$
 (4.18)

Thus we obtain

$$-\chi = 1 - \frac{\lambda}{R_{3D}} \tanh\left(\frac{R_{3D}}{\lambda}\right). \tag{4.19}$$

For our single crystals, $\lambda \ll R_{3D}$ is satisfied, which leads to $\tanh(R_{3D}/\lambda) = 1$. Therefore we get

$$-\chi = 1 - \frac{\lambda}{R_{3D}} \quad (\lambda \ll R_{3D}).$$
 (4.20)

By combining Eq. 4.10 and Eq. 4.20, we finally obtain

$$\frac{\Delta f(T)}{f_0} = -\frac{V_s}{2(1-N)V_c} \frac{\Delta \lambda(T)}{R_{3D}} \quad (\lambda \ll R_{3D}), \tag{4.21}$$

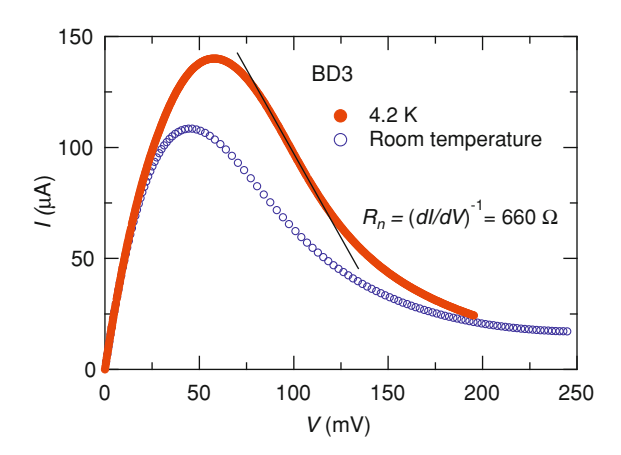
where $\Delta f(T) \equiv f(T) - f(T_{min})$ and $\Delta \lambda(T) \equiv \lambda(T) - \lambda(T_{min})$. Equation 4.21 relates Δf to the actual change in the penetration depth $\Delta \lambda$. From Eq. 4.21 the relationship between $\Delta \lambda$ and Δf can be give by

$$\Delta\lambda(T) = -G\Delta f(T), \tag{4.22}$$

where

$$G = \frac{2R_{3D}(1-N)}{f_0} \frac{V_c}{V_s}. (4.23)$$

Fig. 4.1 I-V characteristic of the tunnel diode BD3 at room temperature and 4.2 K. The value of $R_n = (dI/dV)^{-1}$ at 4.2 K is calculated from the inverse of the slope (*solid line*)



For a 2×2 w slab with thickness of 2d, N can be estimated from the expression [4]

$$\frac{1}{1-N} \approx 1 + \frac{w}{2d}.\tag{4.24}$$

In the thin limit ($d \ll w$), R_{3D} is independent of the thickness d, $R_{3D} \approx 0.2w$ [4]. Therefore, in thin platelet samples the geometric factor G can be written in terms of w^2 ,

$$G \propto \frac{R_{3D}(1-N)}{Vs} \approx \frac{0.2w \times 2d/(2d+w)}{(2w)^2 \cdot 2d} \propto \frac{1}{w^2},$$
 (4.25)

4.1.2 Tunnel Diode LC Oscillator

The essential components of the tunnel diode oscillator are a tank circuit and a tunnel diode (see Fig. 4.2). The circuit is formed by an inductor and a capacitor, which has a resonance frequency $f = 1/2\pi\sqrt{LC}$. The tunnel diode is biased appropriately in the negative differential resistance region so that it serves as an ac-power source for the tank circuit.

The I-V characteristic of the tunnel diode can be described by a combination of the usual forward-biased characteristic of a semiconductor diode and quantum mechanical tunneling [9]. We show the I-V curves of the tunnel diode used in our study at room temperature and 4.2 K in Fig. 4.1. The important feature of the tunnel diode is that there exists the region of negative differential resistance dV/dI, where the tunnel diode operates to cancel the dissipative losses in the tank circuit, so that the oscillation can be sustained. The dc power supply functions to bias the tunnel diode into the negative dV/dI region.

The original setup was designed by Craig Van Degrift [1] for dielectric constant measurements. This system was developed by Antony Carrington [2] in order to

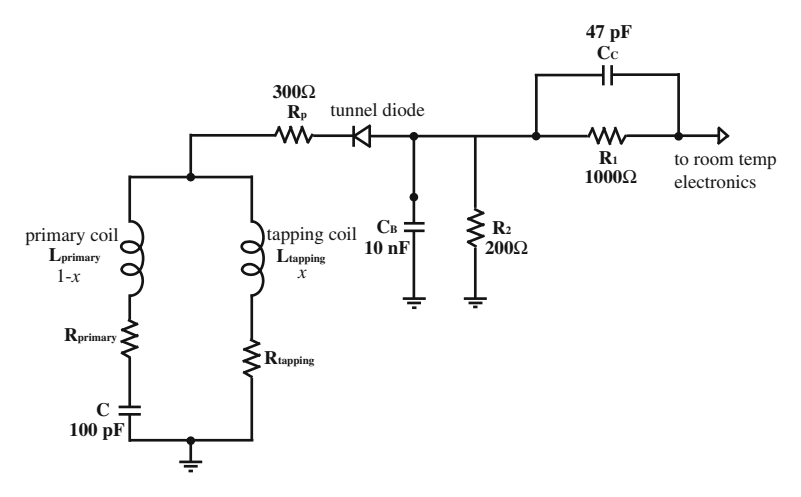


Fig. 4.2 Low-temperature electronics of the tunnel diode oscillator

perform precise measurements of the magnetic penetration depth at low temperatures. Figure 4.2 shows the electronics of the tunnel diode oscillator, which is inside the cryostat so as to sustain the temperature at a constant value precisely. Resistor R₁ serves as an rf isolation of the circuit while the direct currents pass through it. R2 acts as a voltage divider with R_1 to provide the proper dc bias for the tunnel diode. Bypass capacitor C_B is so large that it essentially works as a short circuit at the operating frequency of 13 MHz. Capacitor C_c allows only a small portion of the rf signal to pass through a semi-rigid coaxial cable and reach at the room-temperature electronics. If C_c is too large, the oscillation waveform can be distorted, so C_c must be small enough that only a small portion of the rf signal is coupled out to the room-temperature electronics. Thus, the tank circuit is almost isolated from the roomtemperature electronics. Resistor R_p is required to prevent the parasitic oscillation of the tuned circuit which can be formed by the tapping coil and the stray capacitance of the tunnel diode, but it requires attention that a large capacitance will disturb the fundamental oscillation. In this study, we used the following parameters for each element: $R_1 = 1000 \Omega$, $R_2 = 200 \Omega$, $C_C = 47 pF$, $C_B = 10 nF$, and $R_p = 300 \Omega$.

Figure 4.3 shows the components of the room-temperature electronics. The dc bias for the tunnel diode circuit is generated by a room-temperature current source (Burr-Brown model REF102), which provides a very stable 10 V output. This voltage is buffered with a low noise Op-Amp (OPA177) and filtered before passing through the coaxial cable. The rf oscillation signal (\sim 13 MHz) is carried back through the same coaxible cable. The ac component is coupled through a capacitor to an rf amplifier and then to a balanced mixer. The frequency output from the mixer is the difference between the signal frequency and the local oscillator frequency from a synthesizer (Stanford Research Systems model DS345). The local oscillator frequency is adjusted so as to set the mixer output frequency at around 3 kHz. The signal passes through a bandpass filter and then reaches at a universal frequency counter (Hewlett-Packard

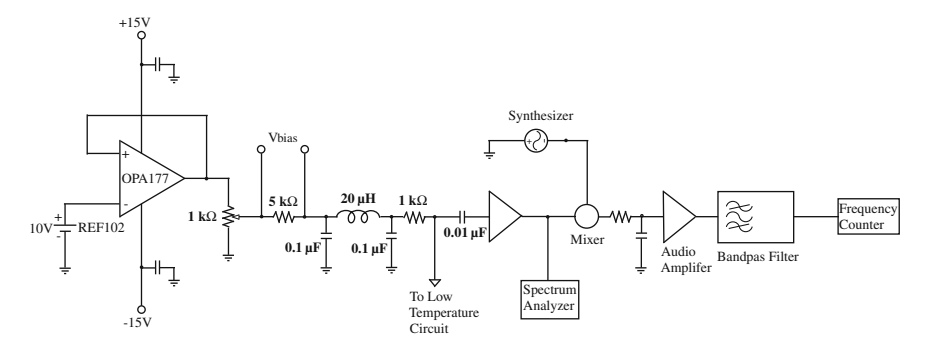


Fig. 4.3 Schematic diagram of room temperature electronics. The parameters for each component used in our system are also shown

model 53131A). The frequency counter is equipped with an optional 10 MHz high stability time base (stability of 1 ppb). This time base signal is also used to generate the synthesized local oscillator signal.

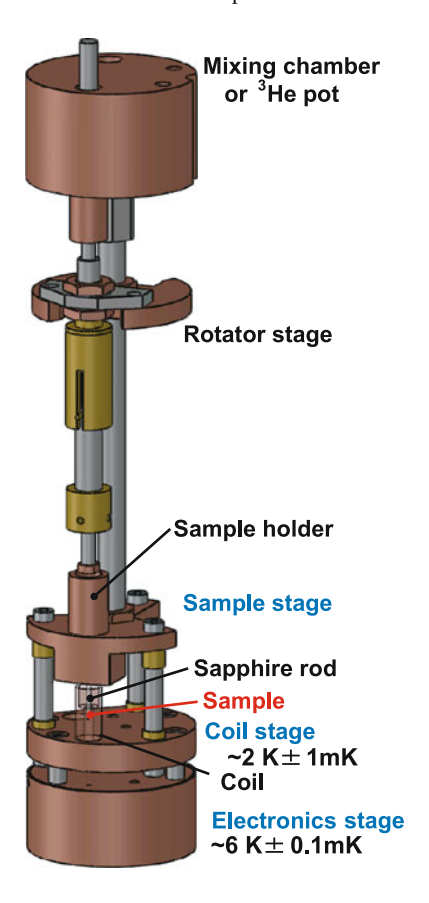
4.1.3 Experimental Setup

The mechanical design of the low temperature part of the system is restricted by the requirement that each part must be maintained at different temperatures. Figure 4.4 shows the schematic picture of the low-temperature apparatus, which can be divided into three parts: the sample, coil, and electronics stages. These stages are separated by rods made from Vespel SP-22, which is selected owing to its extremely low thermal conductivity.

The sample stage is thermally connected to the mixing chamber (\sim 60 mK) of an Oxford Kelvinox 40 dilution refrigerator or 3 He pot (\sim 300 mK) of an Oxford Heliox via a copper wire. The sample is mounted on a sapphire rod of the sample holder with a small amount of Apiezon N grease and inserted into the primary coil. The sample holder is thermally connected to the sample stage using a silver wire, which allows the sample temperature to vary from the base temperature of the stage up to $10\,\mathrm{K}$ (Kelvinox) or $100\,\mathrm{K}$ (Heliox), depending on the cryostat. Two different kinds of thermometers are placed near the sample. The sample temperature is monitored using a RuO2 resistor at low temperatures (0.06–2 K), and a Cernox thermometer at higher temperatures (0.3–100 K). A heater is also placed in the vicinity of the thermometers to change the sample temperature.

The primary coil is made from a thin copper wire (diameter: 0.07 mm). The turns are spaced two wire diameters apart to prevent stray capacitance. The copper can containing the primary coil is glued with GE varnish on the coil stage made from gold-plated oxygen free high conductivity (OFHC) copper. A Cernox thermometer and a heater $(10 \, \text{k}\Omega)$ are placed on the stage to monitor and control the temperature.

Fig. 4.4 Schematic picture of the low-temperature apparatus. For clarity, the copper and silver wires for thermal anchor are not shown. Also, the coaxial cable is omitted



The coil is maintained at a lower temperature (\sim 2 K) than other circuit components (\sim 6 K) to prevent sample heating due to thermal radiation. In order to provide a proper cooling power, a thick silver wire is connected to the 1 K pot of the cryostat. The temperature is maintained within \pm 0.5 mK using a Lakeshore model 340 temperature controller. The magnitude of the ac field inside the coil is estimated to be \sim 10 mOe, so that the sample is always in the Meissner state. The cryostat was surrounded by a bilayer Mumetal shield that reduced the dc field to less than 1 mOe.

All the components of the oscillator part except for the primary coil, i.e., the tunnel diode, capacitors, resistors, and tapping coil, are housed inside a gold-plated copper block. The electronics stage acts as the ground for the circuit. A stainless-steel coaxial cable is connected to the electronics, the end of which is thermally anchored to the 1 K pot. Since self-heating is generated in the oscillator circuit, the temperature is warmer than the coil stage. Therefore a proper cooling power is provided via the coaxial cable and the rods made from Vespel SP-22 between the coil and electronics stages. The electronics temperature is controlled by a Lakeshore

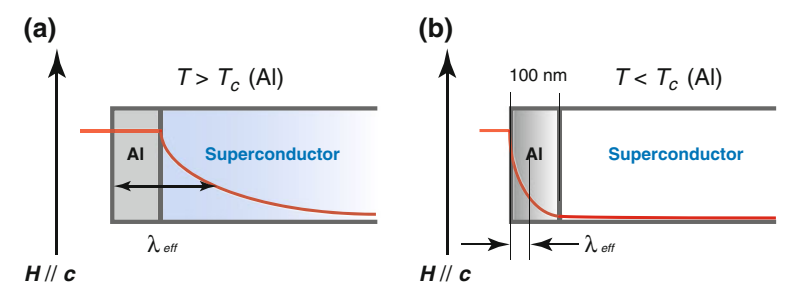


Fig. 4.5 Schematic picture of the principle of the Al coated method. **a** $T > T_c^{\text{Al}}$. **b** $T < T_c^{\text{Al}}$

model 370 temperature controller using a Cernox thermometer and a heater (10 k Ω), which is capable of controlling within ± 0.05 mK at 6 K.

Temperature stability of the primary coil and the electronics is of utmost importance in our experiments, because it determines the noise level of the signal at low temperatures, where our signal is very small. Usually we can achieve a temperature stability of 0.1 mK in the electronics part. We found that for the same temperature change away from the set-point of the thermometer, the frequency change caused by the temperature change of the electronics is about 50 times larger than that of the primary coil. Hence it is important to sustain the electronics temperature more stable than that of the primary coil.

4.1.4 Al-Coating Method

As mentioned previously, we cannot extract the absolute penetration depth from the tunnel diode oscillator technique. The experimental determination of $\lambda(0)$ is a challenging task. In this study, we have performed the absolute penetration depth measurements for the series of the isovalent-doped BaFe₂(As_{1-x}P_x)₂ by using the Al-coated method [10, 11].

To determine the absolute value of the penetration depth, we prepared the BaFe₂(As_{1-x}P_x) samples coated with the Al ($T_c = 1.2\,\mathrm{K}$) film of thickness of ~100 nm. In Fig. 4.5 we show the schematic picture of the principle of the Al-coating method. When the Al film is a normal metal ($T > T_c^{\mathrm{Al}}$, see Fig. 4.5a), it doesn't participate in the screening of the magnetic fields because its thickness (~100 nm) is much less than the normal-state skin depth at the operating frequency of 13 MHz, where δ_{Al} ~75µm for $\rho_0^{\mathrm{Al}} = 10\,\mathrm{\mu}\Omega$ cm. On the other hand, when the Al film is superconducting ($T < T_c^{\mathrm{Al}}$, see Fig. 4.5b), it acts together with the coated superconductor to screen the magnetic fields. The effective magnetic penetration depth $\lambda_{\mathrm{eff}}(T)$ for $T < T_c^{\mathrm{Al}}$ can be given by

$$\lambda_{eff}(T) = \lambda_{Al}(T) \frac{\lambda(T) + \lambda_{Al}(T) \tanh \frac{t}{\lambda_{Al}(T)}}{\lambda_{Al}(T) + \lambda(T) \tanh \frac{t}{\lambda_{Al}(T)}},$$
(4.26)

where t is the thickness of the Al film and $\lambda(T)$ is the penetration depth of the coated superconductor and $\lambda_{\rm Al}(T)$ is the penetration depth of the Al film. We have already known the absolute value of $\lambda(0)$ for Al, then we can extract the absolute penetration depth of the coated superconductors.

4.2 Microwave Cavity Perturbation Technique

4.2.1 Principle

The absolute penetration depth can also be determined by the measurements of the microwave surface impedance. We have measured the surface impedance by using cavity perturbation of superconducting and dielectric resonators. The resonant cavity, which is a hollow enclosed by metal walls, can sustain many standing wave modes. Near each resonant frequency the power absorption spectrum has a Lorentzian shape [6],

$$A(\omega) = \frac{1}{4(\omega - \omega_0)^2 + (2\pi \Gamma)^2},$$
(4.27)

where $f_0 = \omega_0/2\pi$ is the center frequency and Γ is the full frequency width at half-maximum. f_0 and Γ are the two characteristics of the resonator and their ratio gives the quality factor Q of the cavity, which is defined as

$$Q \equiv \frac{f_0}{\Gamma} = \frac{\omega_0 \langle W \rangle}{L},\tag{4.28}$$

where $\langle W \rangle$ is the time-averaged energy stored in the cavity and L is the energy loss per cycle.

Here we introduce a complex frequency notation:

$$\hat{\omega} \equiv \omega_0 - i \frac{\omega_0}{2Q}.\tag{4.29}$$

The principle of the cavity perturbation technique is to measure separately the cavity characteristics both before and after the insertion of the sample. The change in the complex frequency is given by

$$\Delta \hat{\omega} = \hat{\omega_s} - \hat{\omega_0},\tag{4.30}$$

where the subscripts '0' and 's' denote before and after the insertion of the sample, respectively. If the change $\Delta \hat{\omega}$ is adiabatic, then the product of the period and the

time-averaged energy stored is invariant [12],

$$\frac{\langle W \rangle}{\omega_0} = \text{constant.}$$
 (4.31)

This implies that

$$\frac{\Delta \langle W \rangle}{\langle W \rangle} = \frac{\Delta \hat{\omega}}{\hat{\omega}} \sim \frac{\Delta f}{f_0} - \frac{i}{2} \Delta \left(\frac{1}{Q}\right),\tag{4.32}$$

where $\Delta f = f_s - f_0$ is the frequency shift and $\Delta \Gamma = \Delta(1/Q) = 1/Q_s - 1/Q_0$ is the change in the width of the resonance.

For an ellipsoidal sample, $\langle W \rangle$ and the change $\Delta \langle W \rangle$ are given by the external electric field E_0 and magnetic field H_0 , and the polarization P and magnetization M of the sample as follows:

$$\langle W \rangle = \frac{1}{16\pi} \int_{V_c} (|E_0(r)|^2 + |H_0(r)|^2) d^3r,$$
 (4.33)

$$\Delta \langle W \rangle = -\frac{1}{4} \int_{V_s} (P \cdot E_0(r)^* + M \cdot H_0(r)^*) d^3 r, \tag{4.34}$$

where V_c and V_s are the volume of the cavity and sample, respectively. The internal electric field E and magnetic field H of the sample are obtained by solving the Helmholtz differential equations [6],

$$\nabla^2 E(r) + \hat{k} E(r) = 0, \tag{4.35}$$

$$\nabla^2 H(r) + \hat{k}H(r) = 0, (4.36)$$

where \hat{k} is the complex wavevector of the microwave. Since outside the sample $\hat{k} = 0$, the differential equation is so-called the Laplace equation.

In the case of spherical sample, we can solve the equations rigorously,

$$\frac{\Delta \langle W \rangle}{\langle W \rangle} = -\frac{\gamma}{n} \frac{\hat{\varepsilon}_{\text{eff}} - 1}{\hat{\varepsilon}_{\text{eff}} + 2},\tag{4.37}$$

where n = 1/3 (the depolarization factor of a sphere), and also

$$\gamma = \frac{V_c \mid E_0 \mid^2}{2 \int_{V_c} \mid E_0 \mid^2 d^3 r},\tag{4.38}$$

$$\hat{\varepsilon}_{\text{eff}} \equiv \hat{\beta}\hat{\varepsilon},\tag{4.39}$$

$$\hat{\beta} = -2 \left(\frac{-(\hat{k}a)\cos(\hat{k}a) + \sin(\hat{k}a)}{-(\hat{k}a)\cos(\hat{k}a) + \sin(\hat{k}a) - (\hat{k}a)^2\sin(\hat{k}a)} \right). \tag{4.40}$$

Here, $\hat{\varepsilon}_{\text{eff}}$ is the effective permittivity and a is the radius of the sphere. Depending on the ratio of the skin depth δ to sample size a, we can distinguish two limiting case.

- 1. Depolarization Regime: $\hat{k}a \ll 1$ In this limit the fields penetrate uniformly throughout the sample and we can effectively neglect the second term in Eq. 4.35. Therefore, it is only necessary to solve the Laplace's equation. Under this condition the sample is in the so-called depolarization regime, where we can obtain the dielectric constant of the sample.
- **2. Skin depth Regime:** $\hat{k}a \gg 1$ In the skin depth regime where the sample size is much larger than the skin depth, \hat{k} cannot be neglected. Therefore we must solve the full set of Helmholtz equations. As shown in Eq. 4.32, the energy dissipated in the sample is responsible for the variation of the complex frequency of the resonator. For a sample in the skin depth regime, $\Delta \hat{\omega}$ is simply related to the normalized surface impedance \hat{Z}_s ,

$$\frac{\Delta \langle W \rangle}{\langle W \rangle} = \frac{\Delta \hat{\omega}}{\omega_0} = \zeta \, \hat{Z}_s + \lim_{|\hat{\sigma}| \to \infty} \frac{\Delta \hat{\omega}}{\omega_0},\tag{4.41}$$

where ζ is a characteristic constant for the resonator and $\lim_{|\hat{\sigma}| \to \infty} \Delta \hat{\omega} / \omega_0$ represents a shift of the resonance frequency caused by the excluded volume of the field assuming the presence of a perfectly conducting body which has the same size and shape as the sample. In general, ζ and $\lim_{|\hat{\sigma}| \to \infty} \Delta \hat{\omega} / \omega_0$ depend on the detailed size and shape of the sample. However, we can obtain the appropriate form which relates an experimentally measurable quantity $\Delta \hat{\omega} / \omega_0$ to an intrinsic quantity \hat{Z}_s . If we have known certain properties of the material under investigation, we can determine the characteristic constants, as discussed later. To simplify the notation, we define a new variation

$$\frac{\Delta'\hat{\omega}}{\omega_0} \equiv \zeta \, \hat{Z}_s = \frac{\Delta\hat{\omega}}{\omega_0} - \lim_{|\hat{\sigma}| \to \infty} \frac{\Delta\hat{\omega}}{\omega_0},\tag{4.42}$$

where $\Delta'\hat{\omega}/\omega_0$ is the complex frequency shift from a perfectly conducting body having the same size and shape as the sample. The solutions of the real and imaginary parts of Eq. 4.42 give

$$\Delta'(1/Q) = \Delta(1/Q), \tag{4.43}$$

$$\Delta' f = \Delta f - \lim_{|\hat{\sigma}| \to \infty} \Delta f, \tag{4.44}$$

where $\Delta'Q$ and $\Delta'f$ represent the shifts from a perfect conductor.

4.2.2 Surface Impedance

The surface impedance Z_s is given by the surface resistance R_s and the surface reactance X_s ,

$$Z_s = R_s + iX_s. (4.45)$$

On the other side, the surface impedance is defined as the ratio of the electric field to magnetic field at the surface of the metal [13],

$$\hat{Z}_s \equiv \frac{E_{\parallel}}{H_{\parallel}},\tag{4.46}$$

where the sign \parallel denotes the field component within the plane of the surface. Here, \hat{Z}_s , which is normalized by the impedance of the vacuum $Z_0 = \mu_0 c$, is independent of the surface geometry. In the previous subsection, we described how the change in the complex frequency is related to the surface impedance. As shown in Eqs. 4.32–4.44, the surface impedance R_s and the surface reactance X_s are given by

$$R_s = G\left(\frac{1}{2Q_s} - \frac{1}{2Q_0}\right),\tag{4.47}$$

$$X_s = G\left(-\frac{f_s - f_0}{f_0}\right) + C, (4.48)$$

where G is the geometric factor and C is the metallic shift. In order to determine the absolute values of R_s and X_s , we have to determine these two constants. In the case where $\omega \tau \ll 1$ (Hagen-Rubens limit), the surface resistance and reactance are given by simple forms,

$$R_s = X_s = \sqrt{\frac{\mu_0 \omega \rho_n}{2}} = \frac{\mu_0 \omega \delta_n}{2},\tag{4.49}$$

where τ is the relaxation time of electrons, $\delta = \sqrt{2\rho_n/\mu_0\omega}$ is the skin depth in the normal state, and ρ_n is the resistivity. Therefore, if ρ_n is a known quantity, we can obtain the geometric factor G and metallic shift C, and then determine the absolute values of R_s and X_s .

At high frequency, the electromagnetic field penetrates into the sample on a characteristic length scale; this length is either the skin depth δ in the normal state or the penetration depth λ in the superconducting state. In the superconducting state, the following relationship between the surface reactance X_s and the penetration depth λ holds:

$$X_{s} = \mu_{0}\omega\lambda. \tag{4.50}$$

Thus we can obtain the absolute value of the penetration depth, $\lambda(0) = X_s(0)/\mu_0\omega$, from the microwave surface impedance measurements.

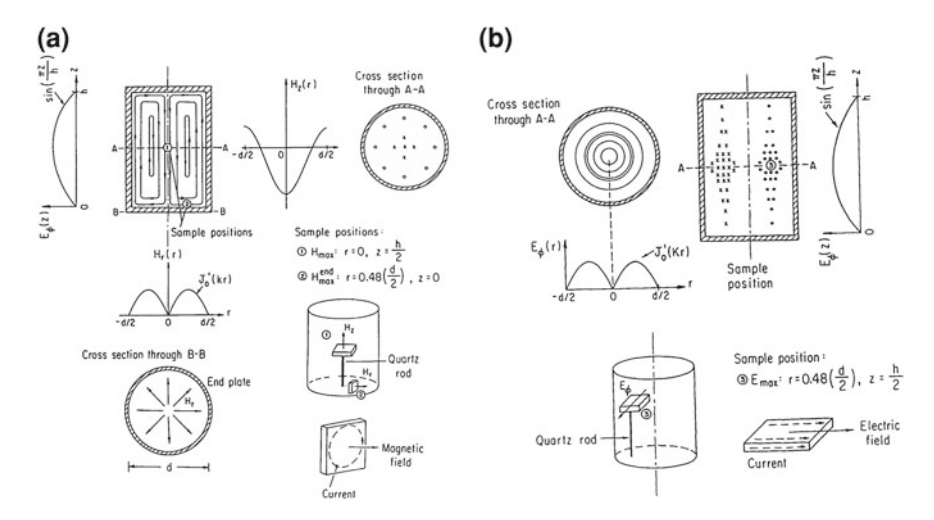


Fig. 4.6 a Distribution of the magnetic field inside a cylindrical cavity resonator for the TE_{011} mode. The maximum magnetic field H_{max} in the cavity (position 1), and the maximum magnetic field H_{max}^{end} on the endplate (position 2) are illustrated. **b** Distribution of the electric field inside a cylindrical cavity resonator for the TE_{011} mode. The position of the maximum field E_{max} (position 3) is shown. The figure is taken from Ref. [17]

4.2.3 Experimental Setup

In the cavity perturbation technique, to get a high quality factor the resonator must be surrounded by materials with extremely low microwave absorption such as superconductors and low-loss dielectrics. In this study we used a superconducting cavity resonator made of Pb-plated OFHC copper [14, 15] and a dielectric cavity resonator constructed from a high-permittivity single crystal of rutile (TiO₂) [16], both of which have high quality factors Q in excess of 10^6 .

The microwave input is carried through the coupling hole via the waveguide or coaxial cable, and confined inside the cavity. The field distributions for the TE_{011} mode used in this study are shown in Fig. 4.6. At the center of the cavity, the magnetic field is maximum and the electric field is nearly zero. When the crystal is placed in the antinode of the microwave magnetic field H_{ω} ($\parallel c$ axis), the shielding current I_{ω} is excited in the ab planes of the sample as shown in the expanded view of Fig. 4.8.

A schematic diagram of the room-temperature setup is shown in Fig. 4.7. We used Hewlett-Packard 83640A synthesized sweeper as a microwave generator. The input signal is carried to the cavity through the coaxial cable and waveguide, and the output is read by Agilent 8757D scalar network analyzer, where the difference between the output and reference signals is picked up. We can extract the resonance frequency f and the quality factor Q from the full frequency width at half-maximum Γ . Lakeshore model 340 or 336 were used to control each temperature of the sample

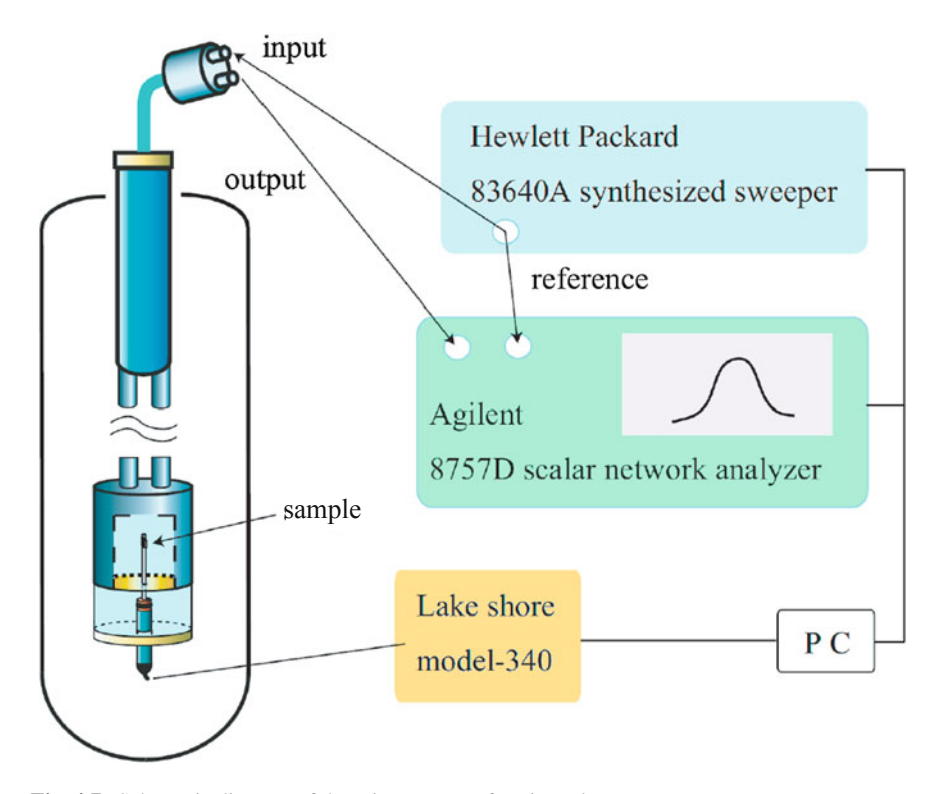


Fig. 4.7 Schematic diagram of the microwave surface impedance measurement

and cavity. In this study, we performed all the measurements at zero dc magnetic field.

Figure. 4.8 shows the schematic picture of the superconducting cavity and its sample holder. The superconducting resonator is soaked in the superfluid 4 He at 1.6 K, so the resonator functions as the superconducting cavity. For the TE₀₁₁ mode, the resonant frequency and the quality factor of the superconducting cavity are operated with $f \sim 27\,\text{GHz}$ and $Q \sim 0.8 \times 10^6$, respectively, in the absence of samples. The sample is placed at the center of the cavity and mounted on a sapphire rod with a tiny dot of Apiezon N grease. The sapphire rod is thermally disconnected with the cavity, but in contact with the block of copper which is thermally weakly coupled to the superfluid 4 He. The thermometer and heater are installed on the block of copper and we can control the temperature of the sample within $\pm 1\,\text{mK}$. This is the so-called hot finger technique [18, 19] and known to have high precision to measure the temperature dependence of both the surface resistance R_s and the surface reactance X_s even in small single crystals. The wires of the thermometer and heater pass through the stainless-steel pipe, whose one edge is covered with stycast 2850FT for maintaining vacuum inside the cavity, and reach to the room-temperature apparatus.

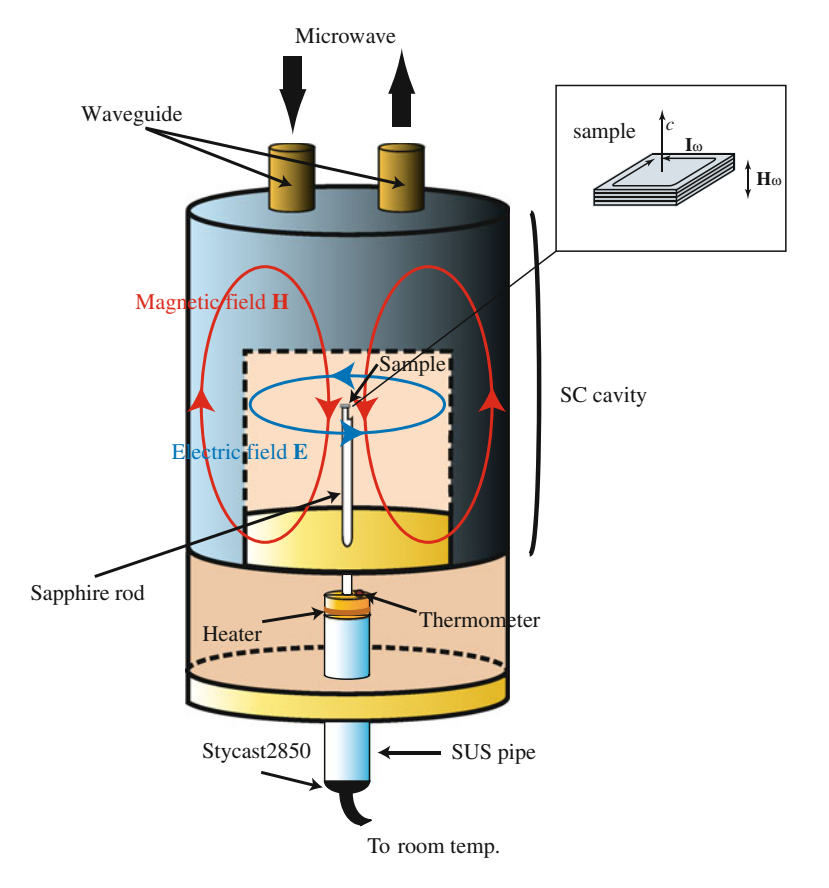
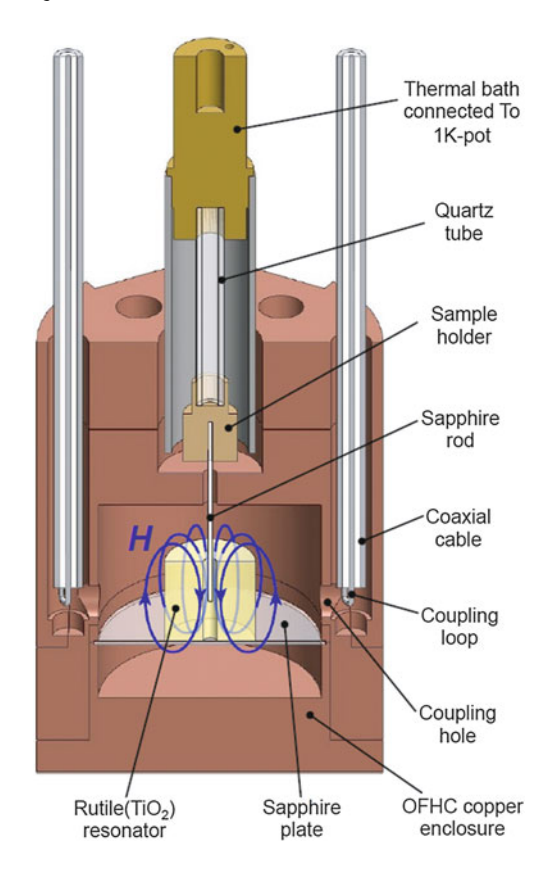


Fig. 4.8 Schematic picture of the superconducting Pb cavity with the sample holder. The enlarged picture indicates the sample configuration

In this study, we also built up a new system for the surface impedance measurements by using a dielectric resonator. In Fig. 4.9, we show the schematic picture of the rutile cavity. The cavity in the absence of samples is operated with $f \sim 5\,\mathrm{GHz}$ and $Q \sim 1.2 \times 10^6$, respectively. The cylindrical dielectric resonator with an access hole for sample introduction is mounted with GE varnish on a sapphire plate, which ensures good thermal contact between the resonator and cavity. A pair of stainless-steel coaxial cables terminate in loops near the cavity. Microwave input and output are coupled to the resonator through a pair of coupling holes of the enclosure. The coupling strength can be varied by adjusting the vertical position of the coaxial cables. We optimized the position and orientation of the coupling loops to get a strong signal and good frequency stability. The temperature of the sample is controlled using the hot finger technique. A sapphire rod is weakly thermally connected to the base of the 1 K pot via a quartz tube. The temperature of the sample is measured with a Cernox thermometer and maintained between 1.8 and 100 K by Lakeshore

Fig. 4.9 Schematic picture of the dielectric cavity resonator constructed from a high-permittivity single crystal of rutile (TiO₂)



model 336. By withdrawing the sample completely from the resonator, the background microwave absorption of the resonator can be measured directly, allowing the absolute microwave absorption of the sample to be determined in situ.

References

- 1. C.T. Van Degrift, Rev. Sci. Instrum. 46, 599 (1975)
- A. Carrington, I.J. Bonalde, R. Prozorov, R.W. Giannetta, A.M. Kini, J. Schlueter, H.H. Wang, U. Geiser, J.M. Williams, Phys. Rev. Lett. 83, 4172 (1999)
- E.M.E. Chia, Penetration depth studies of unconventional superconductors, PhD thesis, University of Illinois at Urbana-Champaign, 2004
- 4. R. Prozorov, R.W. Gianetta, A. Carrington, F.M.A. Moreira, Phys. Rev. B 62, 115 (2000)
- 5. F. Habbal, G.E. Watson, P.R. Elliston, Rev. Sci. Instrum. 46, 192 (1975)
- 6. J. D. Jackson, Classical Electrodynamics, 3rd edn. (John Wiley, New York, 1998)
- 7. V.V. Schmidt, The Physics of Superconductors (Springer, Berlin, 1997)
- 8. D. Shoenberg, Superconductivity, 2nd edn. (Cambridge University Press, 1962)
- 9. W.F. Chow, Principles of Tunnel Diode Circuits (John Wiley, New York, 1964)

- 10. R. Prozorov, R.W. Giannetta, Supercond. Sci. Technol. 19, R41 (2006)
- R.T. Gordon, H. Kim, N. Salovich, R.W. Giannetta, R.M. Fernandes, V.G. Kogan, T. Prozorov, S.L. Bud'ko, P.C. Canfield, M.A. Tanatar, R. Prozorov et al., Phys. Rev. B 82, 054507 (2010)
- 12. G.H. Papas, J. Appl. Phys. 25, 1552 (1954)
- 13. L.D. Landau, E.M. Lifschitz, Electrodynamics of Continuous Media (Pergmon, Oxford, 1984)
- K. Hashimoto, T. Shibauchi, S. Kasahara, K. Ikada, S. Tonegawa, T. Kato, R. Okazaki, C.J. van der Beek, M. Konczykowski, H. Takeya, K. Hirata, T. Terashima, Y. Matsuda, Phys. Rev. Lett. 102, 207001 (2009)
- K. Hashimoto, T. Shibauchi, S. Kasahara, K. Ikada, T. Kato, R. Okazaki, C.J. van der Beek, M. Konczykowski, H. Takeya, K. Hirata, T. Terashima, Y. Matsuda, Phys. Rev. Lett. 102, 207001 (2009)
- W.A. Huttema, B. Morgan, P.J. Turner, W.N. Hardy, Xiaoqing Zhou, D.A. Bonn, R. Liang, D.M. Broun, Rev. Sci. Instrum. 77, 023901 (2006)
- S. Donovan, O. Klein, M. Dressel, K. Holczer, G. Gruner, Int. J. Infrared Millimeter Waves 14, 2423 (1993)
- T. Shibauchi, H. Kitano, K. Uchinokura, A. Maeda, T. Kimura, K. Kishio, Phys. Rev. Lett. 72, 2263 (1994)
- Y. Shimono, T. Shibauchi, Y. Kasahara, T. Kato, K. Hashimoto, Y. Matsuda, J. Yamaura, Y. Nagao, Z. Hiroi, Phys. Rev. Lett. 98, 257004 (2007)

Chapter 5 Superconducting Gap Structure and Quantum Critical Point in $BaFe_2(As_{1-r}P_r)_2$

Abstract In order to investigate the detailed gap structure of the isovalently-doped system BaFe₂ $(As_{1-x}P_x)_2$, we have performed high precision measurements of the magnetic penetration depth in BaFe₂($As_{1-x}P_x$)₂ over a wide range of x, which provide strong evidence that this material has line nodes in the gap. We find that the presence of line nodes in the superconducting gap is a robust signature in this Psubstituted system, which is consistent with the nodes being on the electron sheets rather than the hole sheets whose shapes significantly change with x. We have also found that the x-dependence of the absolute penetration depth at zero temperature exhibits a sharp peak at the optimum composition x = 0.30 ($T_c = 30$ K), demonstrating the first convincing signature of a second-order quantum phase transition deep inside the dome, which separates two distinct superconducting phases. Moreover, the ratio of T_c to the effective Fermi temperature T_F at x = 0.3 marks the highest record among superconductors, implying a possible crossover towards the Bose-Einstein condensate driven by quantum criticality. In this chapter, we will show the results of the penetration depth measurements and discuss the possible superconducting gap structure in isovalent-doped BaFe₂ $(As_{1-x}P_x)_2$, as well as the possibility of a quantum phase transition beneath the superconducting dome in this system.

Keywords Isovalent-doped system \cdot BaFe₂(As_{1-x}P_x)₂ \cdot Magnetici penetration depth \cdot Superconducting gap structure \cdot Line nodes \cdot Quantum critical point \cdot Uemura plot

5.1 Isovalent-Doped BaFe₂ $(As_{1-x}P_x)_2$

The most important question concerning the iron-based superconductors is what is the interaction that glues the electrons into Cooper pairs. Conventional phonon-mediated pairing leads to the superconducting gap opening all over the Fermi surface, while unconventional pairing mechanisms, such as spin fluctuations, can lead to a

gap which has opposite signs on some regions of the Fermi surface. The sign change is a result of the anisotropic pairing interaction which is repulsive in some momentum directions. In high- T_c cuprate superconductors, where the electronic structure is essentially described by a single quasi-two-dimensional Fermi surface, the sign change of order parameter inevitably produces line nodes in the gap function. In iron-based superconductors, however, the Fermi surface has disconnected hole and electron sheets and so the condition for a sign changing gap can be fulfilled without nodes. In fact, a simple picture based on spin fluctuations predicts a distinct type of unconventional order parameter with sign change between these sheets, known as the s_{\pm} -wave state [1, 2]. In this case, each Fermi surface is fully gapped, preventing low-energy excitation of quasiparticles [3–6].

Many experimental studies of iron-based superconductors indicate a fully-gapped superconducting state. On the other hand, some measurements have suggested low-lying quasiparticle excitations [7, 8], which may indicate the presence of nodes in the gap. However, it has been pointed out that disorder may strongly influence the low-energy excitations in the s_{\pm} -wave state [9, 10]. The observation of an unusual resonance mode in neutron data has been interpreted as evidence of the sign-changing s_{\pm} gap [11, 12], but an alternative interpretation based on sign-preserving s_{++} state [13] has also been proposed. In addition, LaFePO with much lower T_c (\sim 6 K) has been reported to have line nodes [14–16] showing apparent contradiction with the fully-gapped s_{\pm} state. Thus, the gap function remains far from settled and the nature of the superconductivity in iron-based superconductors is yet to be determined.

To understand the nature of superconductivity in iron-based superconductors, systematic studies on the superconducting gap structure using high-quality single crystals are required. Although low-lying quasiparticle excitations have been reported in single crystals of the overdoped $Ba(Fe_{1-x}Co_x)_2As_2$, the interpretations are yet controversial, because the scattering effect of the substituted atoms within the Fe planes is still unclear. Moreover, the carrier doping, which gives rise to the imbalance between the electron and hole carrier numbers, makes the electronic structure rather complicated. Therefore, systematic studies on the gap structure in a system without any of impurities or changes in the electronic structure have been highly desirable.

Recently, high-quality single crystals of the isovalent pnictogen substitution system BaFe₂(As_{1-x}P_x)₂ was grown [17]. As with the electron-doped and hole-doped materials, by substituting isovalent P for As, the SDW state is suppressed and the superconducting phase $T_c = 30 \, \text{K}$ appears. The isovalent-doped system BaFe₂(As_{1-x}P_x)₂ is the most suitable system to study the pairing mechanism of the iron-based superconductors as the following reasons. The system can be assumed as a compensated metal, i.e., essentially the same number of electrons and holes, $n_e = n_h$ for any x, which is supported by the band-structure calculations. Therefore we can tune magnetic and superconducting properties without changing charge-carrier concentrations. Moreover, in this system very clean single crystals are available, as demonstrated by the observation of quantum oscillations [18] over a wide range of x (0.41 $\le x \le 1$) including the superconducting region. This indicates that the substitution in the pnictogen sites induces less impurity scattering than that in the carrier-doped system such as $(Ba_{1-x}K_x)Fe_2As_2$ and $Ba(Fe_{1-x}Co_x)_2As_2$.

5.1.1 Phase Diagram

In Fig. 5.1a we show the in-plane resistivity $\rho_{xx}(T)$ in BaFe₂(As_{1-x}P_x)₂ at several P concentrations x ($0 \le x \le 0.71$) [17]. An anomaly of ρ_{xx} in the parent compound BaFe₂As₂ at T = 137 K corresponds to the structural transition (T_0) and simultaneous SDW transition (T_N) . With increasing x, the anomaly is replaced by a step like increase at T_0 , followed by a sharp peak at T_N . The increase in x suppresses these anomalies towards lower temperatures. At x = 0.2, the resistivity data shows a coexistence of SDW and superconductivity, which is observed up to $x \sim 0.28$. For $x \ge 0.3$, no anomaly associated with the SDW transition is observed. The superconducting dome extends over a wide doping range $0.2 \le x \le 0.7$, with maximum $T_c = 30 \,\mathrm{K}$ at x = 0.30. In Fig. 5.1b, we show the temperature dependence of the electrical resistivity $\rho_{xx}(T)$ at low temperatures for x = 0.33, 0.41, 0.56, 0.64, 0.71. At x = 0.33, $\rho_{xx}(T)$ exhibits a T-linear dependence in a wide temperature range above T_c . In the standard Fermi-liquid theory, the resistivity can be described by $\rho_{xx}(T) = \rho_0 + AT^{\alpha}$ with $\alpha = 2$. Therefore the T-linear resistivity is a typical non-Fermi-liquid behavior. For x = 0.33, R_H exhibits a marked T-dependence that can be fitted to $-R_H(H) = C_1/T + C_2$, as depicted in the inset of Fig. 5.1b, which is also a hallmark of the non-Fermi liquid behaviors. With increasing x, the power-law α increases and the Fermi-liquid behavior is recovered at x = 0.71. The contour plot of α in Fig. 5.1c demonstrates this evolution against x, which indicates that the deviations continue to lower temperatures for $x \sim 0.3$. These results suggest the non-Fermi-liquid behaviors governed by quantum fluctuations in BaFe₂(As_{1-x}P_x)₂.

In this system, with increasing x, the lattice constants as well as the pnictogen height h_{Pn} decrease linearly, as shown in the upper and middle panels of Fig. 5.1c, which suggest that the isovalent substitution of P for As is identical to the pressure effect. Indeed, the obtained phase diagram (see Fig. 5.1c) bears striking resemblance to that of the pressure dependence of BaFe₂As₂.

5.1.2 Electronic Structure

A systematic study on the electronic structure of BaFe₂(As_{1-x}P_x)₂ covering a wide range of x (0.41 $\le x \le 1$) has been reported by dHvA measurements using high-quality single crystals [18]. Figure 5.2 shows the angle dependence of the experimentally observed dHvA frequencies F as well as the band structure calculations of the Fermi surface of the BaFe₂(As_{1-x}P_x)₂ series. The observed dHvA frequencies F are related to the extremal cross sectional areas A_k of the Fermi surface orbits via the Onsager relations $F = (\hbar/2\pi e)A_k$. The evolution of these frequencies as the magnetic field is rotated from $B \mid\mid c$ axis ($\theta = 0^{\circ}$) to $B \perp c$ ($\theta = 90^{\circ}$) shows clearly that they originate from quasi-two-dimensional Fermi surface sheets ($F \sim 1/\cos\theta$) as expected from the band structure calculations. A comparison of the dHvA data with the calculated dHvA frequencies for BaFe₂(As_{1-x}P_x)₂ reveals that the splitting of the principal dHvA peaks coming from the c axis dispersion (minimal and maximal

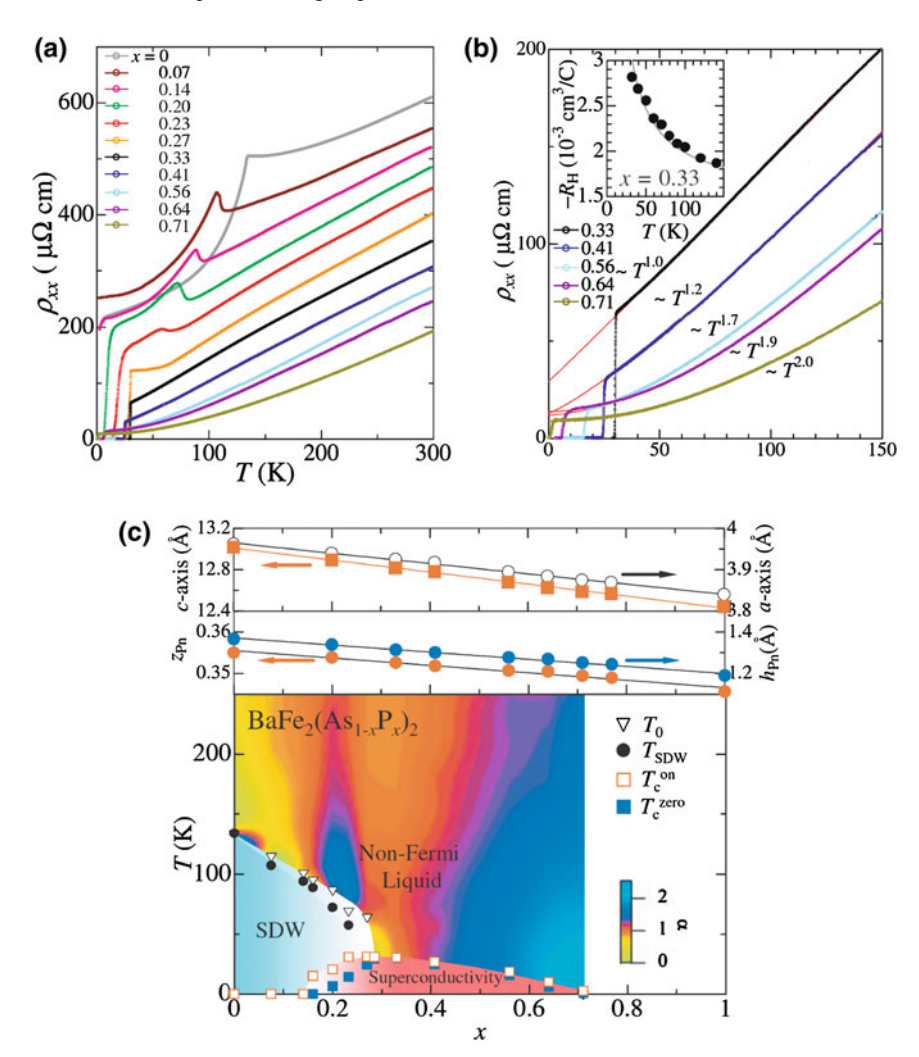


Fig. 5.1 a dc resistivity $\rho_{xx}(T)$ of BaFe₂(As_{1-x}P_x)₂ in the normal-state for several doping levels x. b $\rho_{xx}(T)$ for x=0.33,0.41,0.56,0.64, and 0.71 at low temperatures. Solid lines represent the fits to the power-law. The inset shows T-dependence of $-R_H(T)$ for x=0.33. Solid line indicates the fit to $-R_H(T) = C_1/T + C_2$ with $C_1 = 0.048$ K cm³/C and $C_2 = 1.5 \times 10^{-2}$ cm³/C. c Upper panel lattice constants of c-axis (left axis) and a-axis (right axis) determined from x-ray measurements as a function of x. Middle panel the z coordinate of pnictogen atoms in the unit cell z_{Pn} (left axis) and the pnictogen height from the iron plane $h_{Pn} = (z_{Pn} - 0.25) \times c$ (right axis). Bottom panel phase diagram of BaFe₂(As_{1-x}P_x)₂ against the P content x. The open triangles show the structural transition at T_0 . The closed black circles show T_{SDW} , where the resistivity show reductions due to the reduced spin scattering at the SDW transition. The onset of superconductivity, T_c^{on} , and the zero resistivity temperature, T_c^{zero} , are displayed as open red and closed blue squares. The shade in the nonmagnetic normal state represent evolution of the exponent in resistivity fitted to the power-law. The figure is taken from Ref. [17]

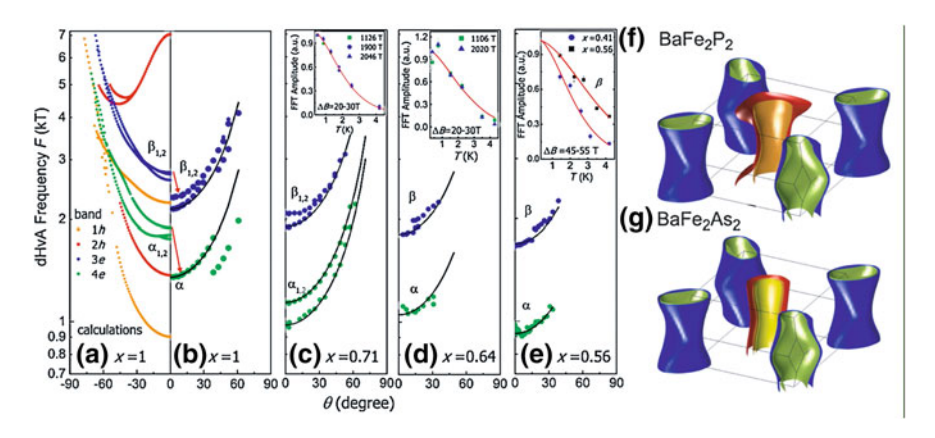


Fig. 5.2 a Angle dependence of the predicted orbits from $B \mid \mid [001] \ (\theta = 90^{\circ})$ for BaFe₂P₂(x = 1) and the electron orbits observed experimentally for $\mathbf{b} \ x = 1$, $\mathbf{c} \ x = 0.72$, $\mathbf{d} \ x = 0.64$, $\mathbf{e} \ x = 0.56$. Solid lines represent the fits to $F(\theta = 0)/\cos\theta$. The insets show the temperature dependence of the Fourier amplitudes for each composition x, which are fitted (solid line) to the Lifshitz-Kosevich formula $X/\sinh X$ with $X = 14.69 \ \mathrm{m}^* T/B$ to determine the effective masses. The calculated Fermi surfaces of the end members, $\mathbf{f} \ \mathrm{BaFe_2P_2}$ and $\mathbf{g} \ \mathrm{BaFe_2As_2}$ (paramagnetic) are also shown. The figure is taken from Ref. [18]

areas) is in good agreement with the calculation for the electron sheets. This is most clearly demonstrated for x=0.71 (see Fig. 5.2a, c). Moreover, the band structure calculations (see Fig. 5.2f, g) suggest that the two electron sheets at the zone corner are quite similar in size and shape in BaFe₂As₂ and BaFe₂P₂ but there are significant differences between the hole sheets. In BaFe₂As₂ three quasi-two-dimensional hole sheets are located at the zone center. On the other side, in BaFe₂P₂ the inner one of these sheets is absent, whereas the outer sheet has become extremely warped.

ARPES measurements [19] have also reported the FSs of BaFe₂(As_{0.62}P_{0.38})₂. By changing the tunable photon energies of synchrotron radiation, three-dimensional Fermi surfaces have been observed. Figure 5.3a, b show the $k_X - k_Y$ planes around the Z point and Γ point, respectively, where X and Y represent the tetragonal unit cell axes, and $k_X = k_Y = \pi/a$. At least two hole sheets around the center of the Brillouin zone (BZ) and two electron sheets around the corner of the BZ are observed. A smaller size of the hole sheets around the Γ point (Fig. 5.3a) compared to those around the Z point (Fig. 5.3b) suggest strong three dimensionality of the Fermi surfaces.

Figure 5.4 shows the k_z dependence of the Fermi surfaces for the x=0.38 sample. Figure 5.4a, b illustrate the cross sections of the Fermi surfaces by the $k_{||}-k_z$ plane around the center and the corner of the BZ, respectively, where $k_{||}$ represents the cuts A-D in Fig. 5.4a, b. By symmetrizing the maps in Fig. 5.4a–c is obtained. For comparison, band-structure calculations for x=0.4 and 0.6 are also shown in Fig. 5.4d, e, respectively. As shown in Fig. 5.4c, the inner electron sheet ε exhibits warping qualitatively consistent with the calculations. As for the hole sheets, the γ sheet is highly three-dimensional, while the β sheet is nearly two dimensional.

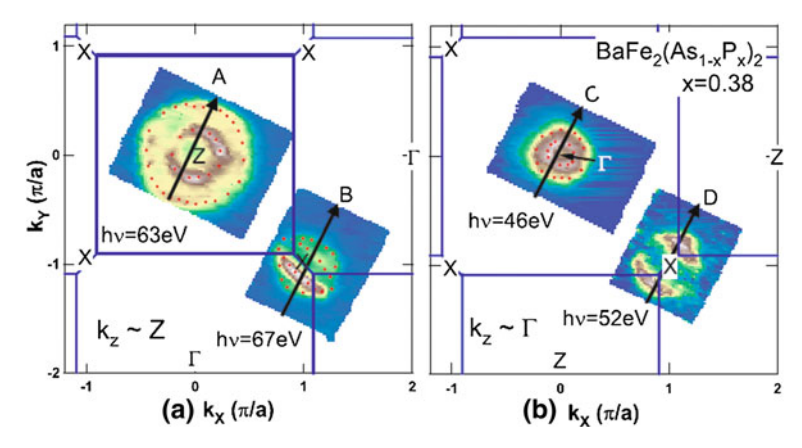


Fig. 5.3 ARPES intensity at E_F mapped in the $k_X - k_Y$ plane taken around **a** the Z point and **b** Γ point. Blue lines represent the BZ. Red dots indicate k_F positions. The figure is taken from Ref. [19]

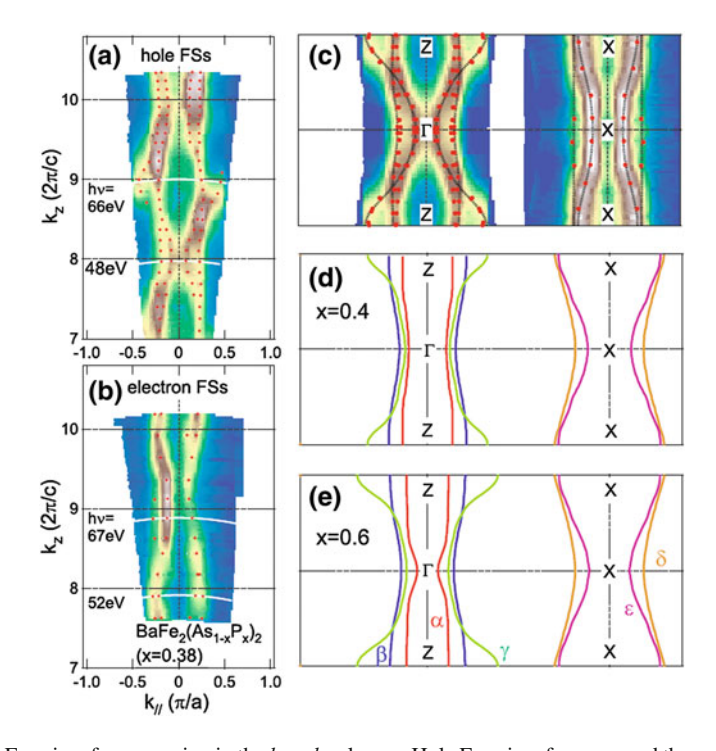


Fig. 5.4 Fermi surface mapping in the $k_{||} - k_z$ plane. a Hole Fermi surfaces around the center of the Brillouin zone (Γ point). b Electron Fermi surfaces around the corner of the Brillouin zone (X point). The directions of $k_{||}$ are the same cuts in the Fig. 5.3. c Fermi surfaces obtained by symmetrizing the plots in $\bf a$ and $\bf b$. d, $\bf e$ Band-structure calculations for x=0.4 and 0.6. respectively. The figure is taken from Ref. [19]

These results give rise to a poor nesting between the electron and hole sheets, but alternatively lead to a partial nesting between the δ electron sheets.

5.1.3 Quantum Criticality

To explore a possible presence of a QCP within the dome, $BaFe_2(As_{1-x}P_x)_2$ appears to be a most suitable system, in which the isovalent substitution of P for As in parent compound $BaFe_2As_2$ offers an elegant way to suppress magnetism and induce superconductivity [17], and the non-Fermi liquid properties have been seen in the normal state above the superconducting dome (see Fig. 5.1c). In contrast to most other members of the iron-based superconductors, very clean and homogeneous crystals of $BaFe_2(As_{1-x}P_x)_2$ are available [17], and the de Haas-van Alphen (dHvA) oscillations [18] have been observed over a wide x range including the superconducting compositions, which give detailed information on the electronic structure. Since P and As are isoelectric, the system remains compensated for all values of x.

The normal-state electronic structure of BaFe₂(As_{1-x}P_x)₂ determined by the dHvA experiments is significantly modified from that by the band calculation [18]. Figure 5.5a, b show the doping evolution of the cross sectional area A_k and the effective mass m_e^* for $0.41 \le x \le 1$, respectively, which are determined by the dHvA oscillations arising from the extremal orbit on the outer electron Fermi surface (β -orbit in Fig. 5.14). In contrast to no essential x-dependence expected from the band calculations, a shrinkage of the electron sheets as well as a critical-like behavior of the mass renormalization are observed as the system is tuned towards the optimal composition $x \sim 0.3$. At the same time T_c increases and shows a maximum at the boundary of the magnetic order (see Fig. 5.5c). These results suggest a significant increase in the strength of the many-body interactions toward to the SDW phase boundary, which is most likely caused by a quantum spin fluctuations.

Indeed, such AF fluctuations have been probed by recent NMR measurements [23]. Figure 5.6a shows the ^{31}P nuclear spin-lattice relaxation rate divided by temperature, $1/T_1T$, for BaFe2(As1-xPx)2. In the standard Fermi-liquid state, the Korringa law $T_1TK^2=$ const. generally holds, where K is the Knight shift. However, this is inapplicable to BaFe2(As1-xPx)2 near the SDW phase (x < 0.3) because the Knight shift K is almost independent of T although Curie-Weiss behavior is observed in $1/T_1T$. For $x\sim0.3,\ 1/T_1T$ increases significantly with approaching T_c . Since $1/T_1T$ is described by the wavevector average of the imaginary part of the dynamical susceptibility $\chi''(q,\omega_0),\ 1/T_1T\propto\sum_q|A(q)|^2\chi''(q,\omega_0)/\omega_0$, the $1/T_1T$ data demonstrates that AF fluctuations with finite q continue to grow with approaching T_c at optimal doping.

The AF fluctuations in BaFe₂(As_{1-x}P_x)₂ are enhanced significantly as the P concentration approaches the maximum T_c ($x \sim 0.3$), as evidenced by the rapid increase in $1/T_1T$ from conventional Fermi-liquid behavior at x = 0.64, where $1/T_1T$ and K are almost constant. The crossover from Fermi-liquid to non-Fermi-liquid behavior in $1/T_1T$ is consistent with the resistivity results. As the system approaches the optimal

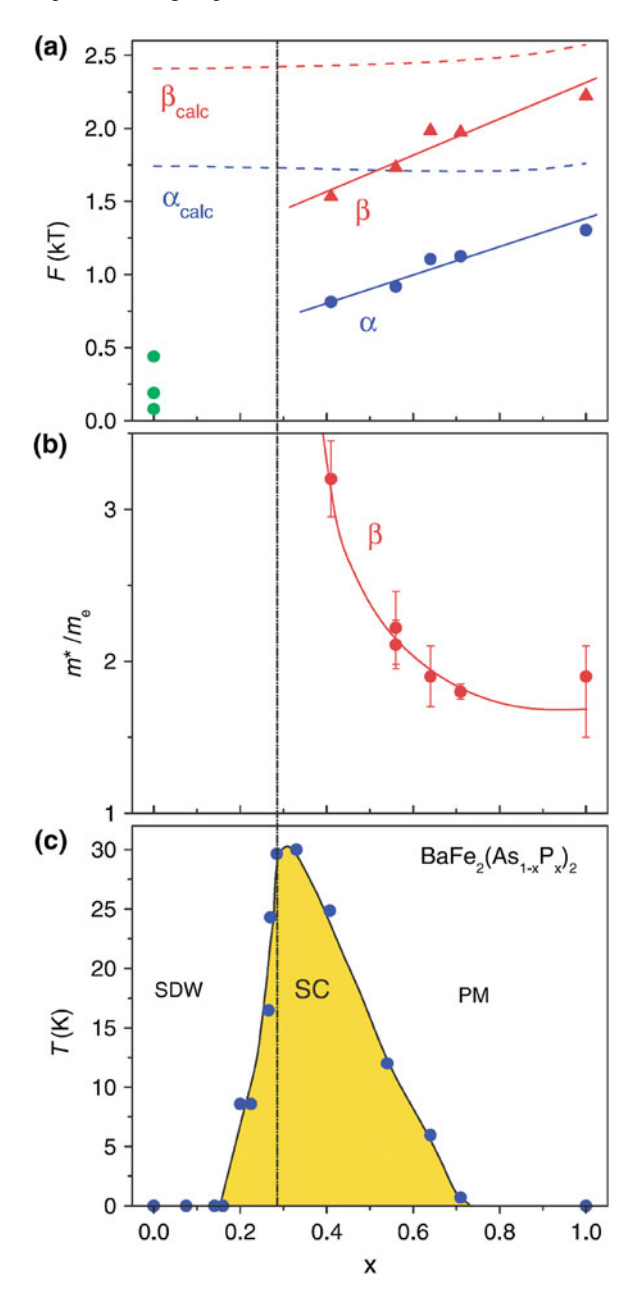


Fig. 5.5 Averaged electron sheet frequencies (α and β) versus P content x. a The dashed lines show band structure predictions. b The variation with x of the quasiparticle effective masses m^* and c T_c . The vertical dashed line indicates the location of the onset of the appearance of magnetism at T=0 K. The figure is taken from Ref. [18]

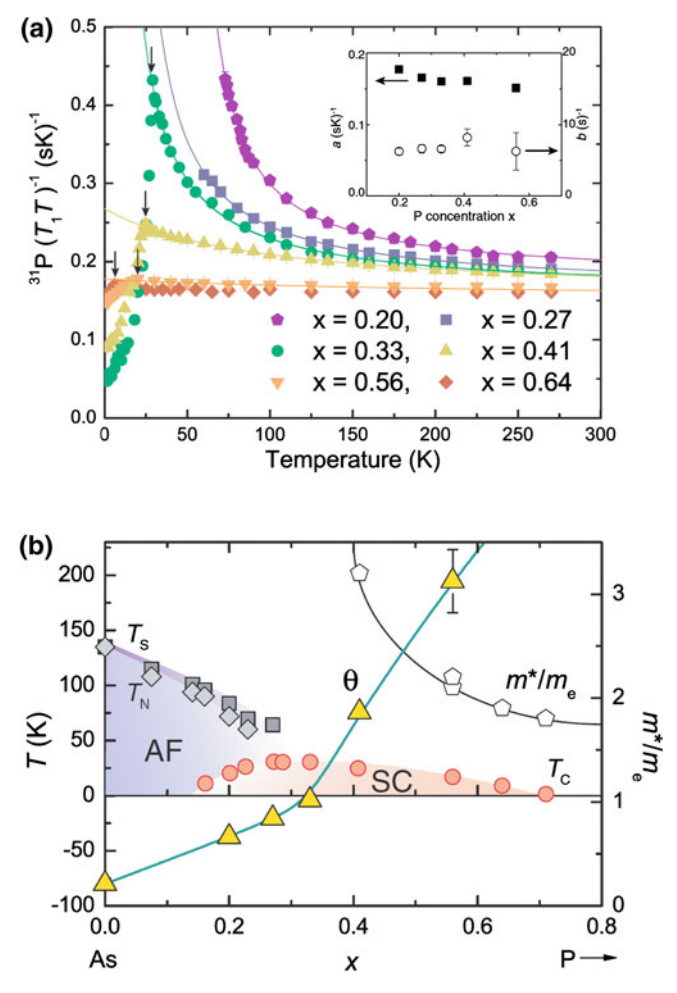


Fig. 5.6 a 31 P1/ T_1 divided by temperature T of BaFe₂(As_{1-x}P_x)₂ for several P concentrations x. *Solid lines* represent fits to $1/T_1T = a + b(T + \theta)^{-1}$. As AF fluctuations are suppressed, T_c (denoted by *arrows*) also decreases. *Inset* fitting parameters of $1/T_1T$. The fitting parameters a and b are plotted against x. The a and b weakly depend on x, but θ shows a strong x dependence. The small value of θ at $x \approx 0.3$ are insensitive to the fitting parameters of a (*left axis*) and b (*right axis*). b x - T phase diagram of BaFe₂(As_{1-x}P_x)₂. *Left axis* the *triangles* represent θ . *Right axis* the enhancement of the effective mass (*pentagons*) is observed in proximity to a magnetic instability signaled by $\theta \sim 0$ at $x \sim 0.3$. The figure is taken from Ref. [23]

composition with maximum T_c ($x \sim 0.3$), the temperature dependence of the resistivity changes from T^2 to T-linear. The evolution of the AF spin fluctuations detected by $1/T_1T$ against P substitution x can be fitted by the equation expected from the self-consistent renormalization (SCR) theory, $1/T_1T = a + b(T + \theta)^{-1}$. The Weiss temperature θ obtained from the fitting increases with x and becomes almost zero near $x \sim 0.3$, where the maximum T_c is achieved (see Fig. 5.6b). $\theta = 0$ K implies that

the dynamical susceptibility probed by the $1/T_1T$ measurement diverges at absolute zero, which strongly suggests the existence of an AF QCP near $x \sim 0.3$ in proximity to the AF phase boundary. As x is varied towards optimal doping $x \sim 0.3$ from x=0.64, the magnetic fluctuations are dramatically enhanced. Importantly, the quasiparticle mass m^* and T_c increase as θ approaches 0 K. This strongly suggests that the AF quantum fluctuations lead to the strong mass renormalization.

5.2 Experimental

Single crystals of BaFe₂($As_{1-x}P_x$)₂ were provided by Dr. Sigeru Kasahara at Kyoto University. The crystals were grown by a self-flux method and characterized by using x-ray diffraction and energy dispersion. Our BaFe₂($As_{1-x}P_x$)₂ crystals [17] exhibit excellent bulk superconducting properties. In Fig. 5.7 we show the temperature dependence of the dc resistivity and the specific heat for the nearly optimally doped BaFe₂($As_{0.67}P_{0.33}$)₂, which demonstrate a very sharp superconducting transition at $T_c = 30$ K. The specific heat data measured by using an ac technique is also used to determine the upper critical field H_{c2} (see the inset of Fig. 5.7).

The temperature dependence of penetration depth $\lambda(T)$ in BaFe₂(As_{1-x}P_x)₂ over a wide range of concentration x (see Fig. 5.8) was measured by the tunnel diode oscillator down to ~80 mK and by the microwave superconducting and dielectric cavity

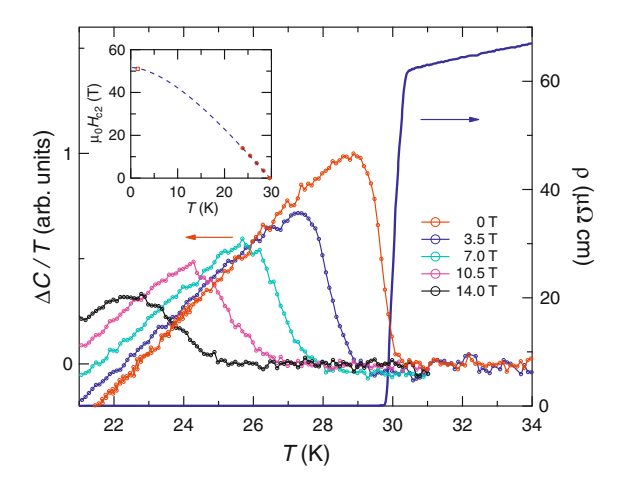
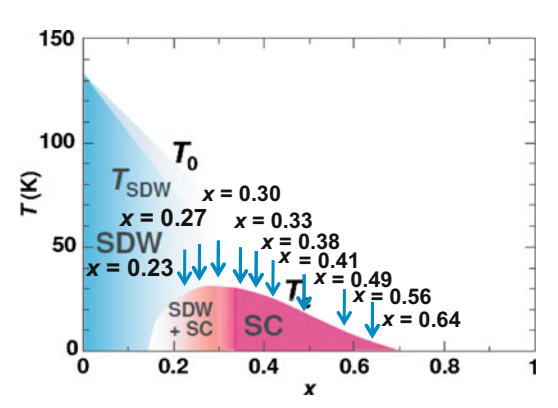


Fig. 5.7 Relative change in the electronic specific heat $\Delta C/T$ under magnetic fields applied along the c axis in a single crystal of $BaFe_2(As_{0.67}P_{0.33})_2$. A smooth background determined from an extrapolation of the 14 T data has been subtracted. Temperature dependence of the in-plane resistivity ρ of a crystal from the same batch is also shown on the *right axis*. *Inset* shows the upper critical field $H_{c2}(T)$ determined from the mid point of the specific heat jump at each field (*closed circles*) and the irreversibility field measured by torque measurements (*open square*). [18] The *dashed line* is a fit to the Wertharmer-Helfand-Hohenberg formula

5.2 Experimental 73

Fig. 5.8 Phase diagram of BaFe₂(As_{1-x}P_x)₂. The *arrows* indicate the composition x measured in this study



resonators down to $\sim 1.6\,\mathrm{K}$ [3, 4]. In both measurements a weak ac magnetic field is applied along the c axis, generating supercurrents in the ab plane. The penetration depth results obtained by the two techniques at different frequencies show excellent agreement.

To determine the absolute value of $\lambda(0)$, we performed three different methods. The first is the Al-coated method [24, 25], in which the tunnel diode oscillator technique is extended to obtain the absolute penetration depth. The second is the microwave cavity perturbation technique using the superconductivity Pd and dielectric material TiO₂. In addition to the above two direct methods, we also evaluate $\lambda(0)$ from the low-temperature slope of the relative change in the penetration depth, $\Delta\lambda(T) = \lambda(T) - \lambda(0)$, measured by the tunnel diode oscillator down to $80\,\mathrm{mK}$, by assuming the relation $\frac{\Delta\lambda(T)}{\lambda(0)} = \frac{\ln 2}{\Delta_{\mathrm{gap}}} k_B T$.

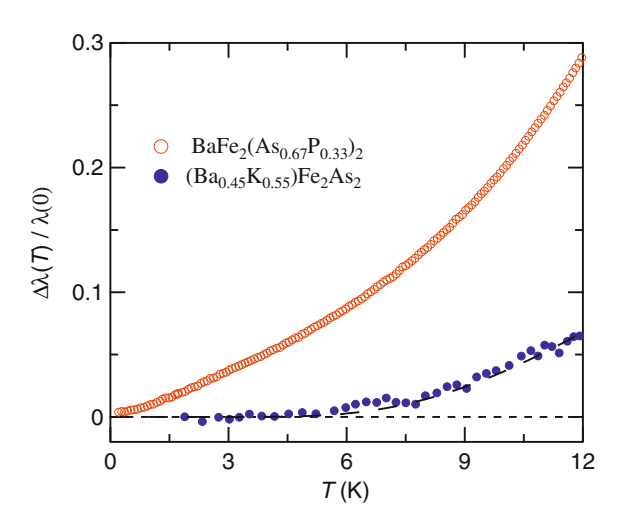
5.3 Results and Discussion 1: Superconducting Gap Structure of $BaFe_2(As_{1-x}P_x)_2$

5.3.1 Nearly Optimally Doped BaFe₂(As_{0.67}P_{0.33})₂

Figure 5.9 shows the normalized change in the penetration depth $\Delta\lambda(T)/\lambda(0)$ in the nearly optimally doped BaFe₂(As_{0.67}P_{0.33})₂, compared with the results for the optimally doped (Ba_{0.45}K_{0.55})Fe₂As₂ obtained from the microwave cavity perturbation technique [4]. In sharp contrast to the flat behavior observed in the K-doped crystal, $\Delta\lambda(T)$ in BaFe₂(As_{0.67}P_{0.33})₂ exhibits a strong superlinear temperature dependence below \sim 6 K. Such a steep temperature dependence is a strong indication of line nodes in the superconducting gap.

The normalized superfluid density $\rho_s(T) \equiv \lambda^2(0)/\lambda^2(T)$ in Fig. 5.10 also clearly demonstrates the fundamental difference between the P- and K-doped samples. The low-temperature data of BaFe₂(As_{0.67}P_{0.33})₂ can be fitted to $1 - \alpha (T/T_c)^n$ with the

Fig. 5.9 Normalized change in the penetration depth $\Delta \lambda(T)/\lambda(0)$ for BaFe₂ $(As_{0.67}P_{0.33})_2$, compared with the data of $(Ba_{0.45}K_{0.55})Fe_{2}As_{2}$ $(T_{c} \simeq$ 33 K) obtained from the microwave cavity perturbation technique [4]. We used $\lambda = 200$ and $280 \, \text{nm}$ for BaFe₂(As_{0.67}P_{0.33})₂ and (Ba_{0.45}K_{0.55})Fe₂As₂, respectively. The dashed line represents the fit to the exponential form, $\Delta \lambda(T)/\lambda(0) =$ $\sqrt{\pi \Delta_0/2T} \exp(-\Delta_0/T)$



exponent $n = 1.13(\pm 0.05)$, close to unity. This is completely incompatible with the flat exponential dependence observed in the fully gapped (Ba_{0.45}K_{0.55})Fe₂As₂, and immediately indicates the low-lying quasiparticle excitations in this system. This is fundamentally different from some studies [4, 7, 8] in iron-based superconductors such as Ba(Fe_{1-x}Co_x)₂As₂ suggesting unconventional superconductivity from the power-law dependence of superfluid density with $n=2.0\sim2.4$. In the fully gapped s_{+} state, it has been suggested that substantial impurity scattering may induce in-gap states that change the exponential superfluid density to a power-law dependence, but the exponent is expected to be not smaller than ~ 2 [9, 10]. However, the present results with exponent significantly smaller than 2 and much closer to 1 expected for clean superconductors with line nodes, cannot be explained by these modifications of a full-gap state, but is indicative of well-developed line nodes in the gap. Here we note that our data do not exclude that some of the bands remains fully gapped. Indeed the whole temperature dependence of $\lambda^2(0)/\lambda^2(T)$ is different from that of the single-band d-wave superconductor YBa₂Cu₃O_{7- δ} [26], which can be explained by different gap structures in different bands.

The fact that the experimental value of n is slightly larger than unity may result from impurity scattering. In the limit of high levels of disorder, a gap with line nodes gives $\Delta\lambda(T)\sim T^2$, and the following formula is often used to interpolate between the clean and dirty limits [27], $\Delta\lambda(T)\propto T^2/(T+T^*)$. The disorder parameter T^* is related to the impurity band width γ_0 . If we use this formula to fit our data (solid line in Fig. 5.10b), we get $T^*=1.3\,\mathrm{K}\approx 0.04T_c$, suggesting that our crystals are reasonably clean superconductors with line nodes. We note that the small upturn in $\Delta\lambda(T)$ is observed in some samples as shown in the inset of Fig. 5.10b, which is likely due to a small amount (of the order of 0.1% in volume) of paramagnetic impurities. However, this effect is negligible for $T>0.5\,\mathrm{K}$ ($\sim 0.017T_c$), and is very small in sample #1, so this does not affect our conclusion of the existence of low-lying quasiparticle excitations.

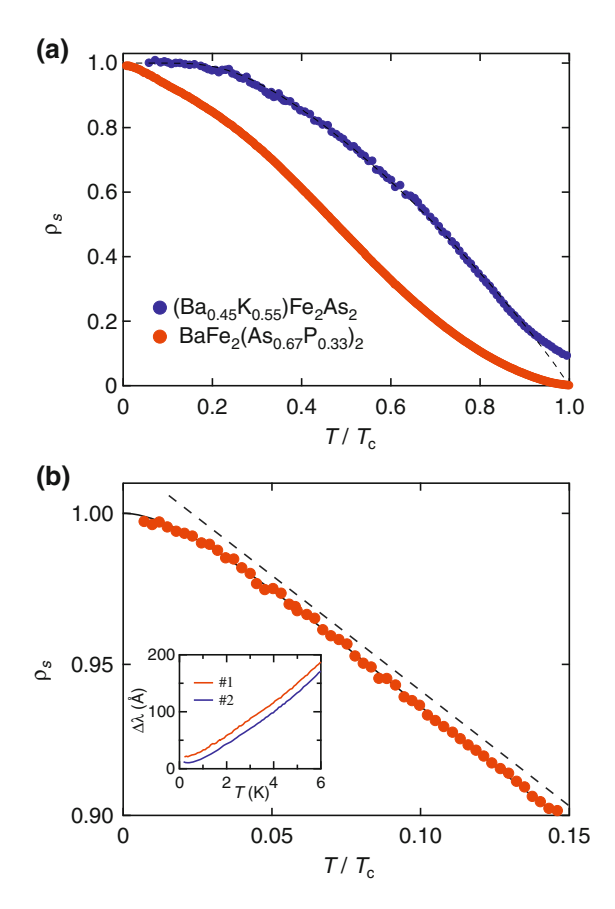
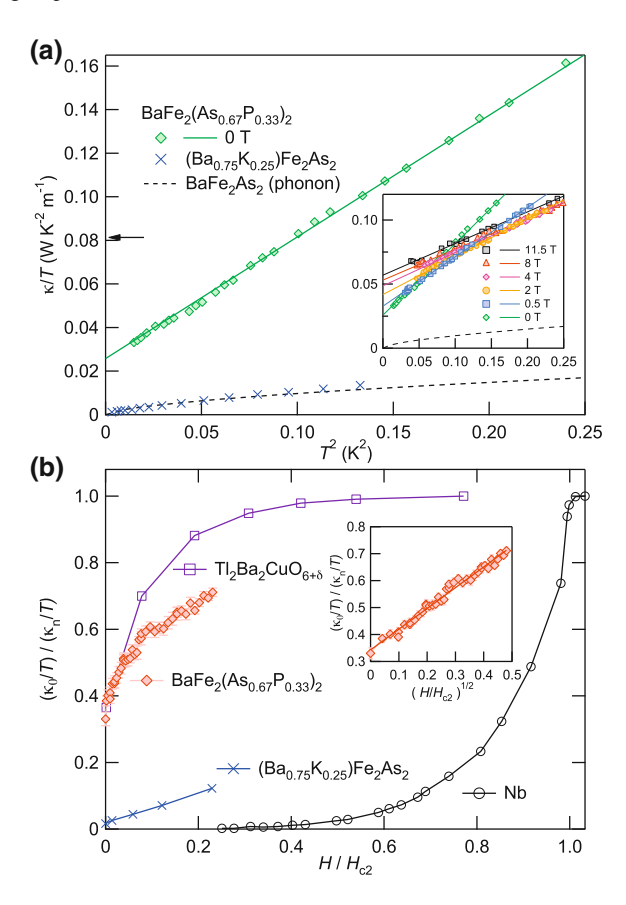


Fig. 5.10 a Normalized superfluid density $\rho_s(T) \equiv \lambda^2(0)/\lambda^2(T)$ as a function of T/T_c for BaFe₂(As_{0.67}P_{0.33})₂ and (Ba_{0.45}K_{0.55})Fe₂As₂. The *dashed line* represents the fit to a two-gap model with fully opened gaps. The tail near T_c in (Ba_{0.45}K_{0.55})Fe₂As₂ is due to the skin depth effect at microwave frequencies. **b** The data follow a T-linear dependence (*dashed line*) down to $T/T_c \sim 0.05$. The deviation at lower T/T_c can be fitted to the dependence for a gap with line nodes with disorder (*solid line*). The *inset* shows $\Delta\lambda(T)$ at low temperatures in two samples (shifted vertically for clarity)

5.3.2 Comparisons with Thermal Conductivity and NMR Measurements

Figure 5.11a shows the temperature dependence of κ/T in zero field. In hole-doped (Ba_{0.75}K_{0.25})Fe₂As₂ [5], $\kappa(T)/T$ is nearly identical to the phonon contribution κ_{ph}/T obtained from non-superconducting BaFe₂As₂ [28]. This is consistent with fully-gapped superconductivity, in which very few quasiparticles are excited at $T \ll T_c$. In spite of similar values of residual electrical resistivity in the normal state [5, 17], the magnitude of κ/T in BaFe₂(As_{0.67}P_{0.33})₂ is strongly enhanced from

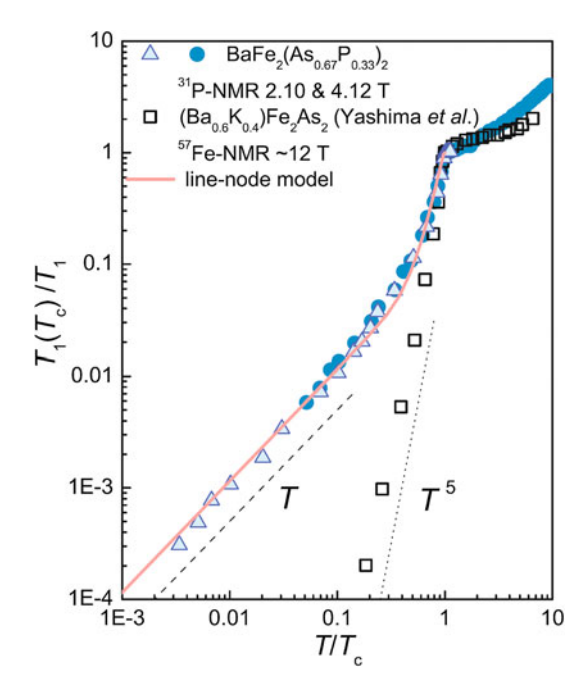
Fig. 5.11 a Thermal conductivity divided by temperature κ/T is plotted against T^2 at zero field (main panel) and on a linear T axis (inset). The solid lines are the fits to the T^2 dependence. The reported data of (Ba_{0.75}K_{0.25})Fe₂As₂ $(T_c \simeq 30 \,\mathrm{K})$ [5] and the phonon contribution estimated in BaFe2As2 [28] are also shown. **b** Residual $\kappa_0(H)/T$ vs. H/H_{c2} . Also shown are the results for Tl₂Ba₂CuO_{6+δ} [31], $(Ba_{0.75}K_{0.25})Fe_2As_2$ [5], and Nb [32]. The gradual increase of $\kappa(H)/T$ in $(Ba_{0.75}K_{0.25})Fe_2As_2$ has been attributed to the slight modulation of the gap value [5]. The inset shows the same data in BaFe₂(As_{0.67}P_{0.33})₂ plotted against $(H/H_{c2})^{1/2}$. The *line* represents the \sqrt{H} dependence



that in $(Ba_{0.75}K_{0.25})Fe_2As_2$. At low temperatures the data are well fitted by $\kappa/T=aT^2+b$. The presence of a finite residual value $b\simeq 25\,\mathrm{mW/K^2}$ m is clearly resolved. It has been shown that in the range $k_BT<\gamma_0$ the quasiparticle thermal conductivity in superconductors with line nodes is given by $\kappa/T=\kappa_0/T$ $\left(1+O\left[T^2/\gamma_0^2\right]\right)$, where γ_0 is the impurity bandwidth [29]. The term κ_0/T arises from the residual quasiparticles, or the zero-energy density of states (DOS) caused by the impurity induced Andreev bound states. For line nodes, a rough estimation gives $\kappa_0/T\approx 22\,\mathrm{mW/K^2}$ m [30], which reasonably coincides with the observed value. The second T^2 -term in the above equation arises from the thermally excited quasiparticles around the nodes, which is also consistent with the observed quadratic temperature dependence of κ/T with a slope one order of magnitude larger than κ_{ph}/T .

Figure 5.11b shows the field dependence of κ_0/T . The most distinguished feature is that $\kappa_0(H)/T$ increases steeply at low fields and attains nearly 70% of the normal-state value κ_n/T even at $0.2H_{c2}$ (where $\kappa_n/T\sim 81\,\mathrm{mW/K^2}$ m is estimated from the Wiedemann-Franz law by using the residual resistivity $\rho_0\approx 30\,\mu\Omega$ cm). Such a field dependence is quite similar to that in $Tl_2Ba_2CuO_{6+\delta}$ with line nodes [31] but is in

Fig. 5.12 Normalized $1/T_1$ by its T_c value for BaFe₂(As_{0.67}P_{0.33})₂ and (Ba_{0.6}K_{0.4})Fe₂As₂. *Solid line* represents the calculation for a line-node form $\Delta(\phi) = \Delta_0 \sin(2\phi)$ with $2\Delta_0 = 6k_BT_c$ and $N_{res}/N_0 = 0.34$. The figure is taken from Ref. [34]



dramatic contrast to that in fully gapped superconductors such as Nb [32]. In fully gapped superconductors, quasiparticles excited by vortices are localized and unable to transport heat at low fields. In sharp contrast, the heat transport in superconductors with nodes is dominated by contributions from delocalized quasiparticles outside vortex cores. In the presence of line nodes where the density of states has a linear energy dependence $N(E) \propto |E|, N(H)$ increases steeply in proportion to \sqrt{H} because of the Doppler shift of the quasiparticle energy [33]. This is consistent with the field dependence of $\kappa_0(H)/T$ in BaFe₂(As_{0.67}P_{0.33})₂ shown in the inset of Fig. 5.11b.

Figure 5.12 shows the temperature dependence of the normalized 31 P $1/T_1$ in the superconducting state for BaFe₂(As_{0.67}P_{0.33})₂ [34] at several magnetic fields, as well as the data for (Ba_{0.6}K_{0.4})Fe₂As₂. In BaFe₂(As_{0.67}P_{0.33})₂ a marked $1/T_1$ behavior different from other iron-based superconductors such as (Ba_{1-x}K_x)Fe₂As₂ is observed; while the $1/T_1$ in (Ba_{0.6}K_{0.4})Fe₂As₂ exhibits a T^5 power-law dependence down to low temperatures indicative of a fully gapped state, in BaFe₂(As_{0.67}P_{0.33})₂ $1/T_1T$ = const. behavior below \sim 0.1 T_c is observed, demonstrating the existence of the residual density of states at zero energy. Although $1/T_1$ depends on the magnetic fields, the $1/T_1T$ = const. behavior below \sim 0.1 T_c can been seen even at $H \rightarrow 0$. There are two possible sources for the field dependence of $1/T_1$ in the vortex mixed state: one is from localized quasiparticles inside vortex cores and the other is from delocalized quasiparticles originating from nodes in the gap. Since the applied magnetic field is much smaller than $H_{c2} \sim 52\,T$, it is unlikely that the observed

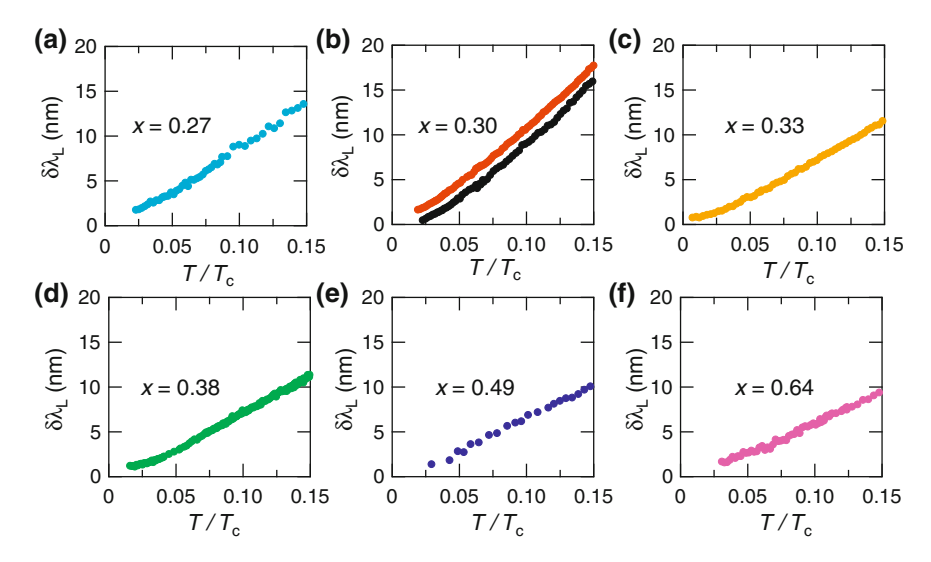


Fig. 5.13 Relative change in the penetration depth at low temperatures as a function of T/T_c for different compositions from x = 0.27 (a) to 0.64 (f)

saturation of $1/T_1T$ is causes by localized quasiparticles inside vortex cores. Therefore, the field dependence of $1/T_1$ in BaFe₂(As_{0.67}P_{0.33})₂ comes from the contributions of the delocalized quasiparticles originating from nodes in the gap, which is consistent with the existence of the residual density of states near the Fermi energy.

The present results, (i) the quasi–T-linear dependence of $\Delta\lambda(T)$, (ii) the presence of κ_0/T at zero field, (iii) the T^2 dependence of κ/T , (iv) the \sqrt{H} field dependence of κ/T , and (v) the $1/T_1T$ = const. behavior, all indicate that line nodes exist in the gap function of BaFe₂(As_{0.67}P_{0.33})₂.

5.3.3 Doping Dependence of Penetration Depth

An important question is then to answer where the nodes are located. Since the superconducting gap structure is closely related to the pairing mechanism, knowledge of the detailed superconducting gap structure is a major step toward identifying the interactions that produce pairing. To do this, we have performed measurements of the magnetic penetration depth over a wide range of x (0.26 $\leq x \leq$ 0.64). Figure 5.13a-f show the low-temperature relative change in the penetration depth, $\Delta\lambda = \lambda(T) - \lambda(0)$, as a function of T/T_c . The most notable feature is that all samples exhibit the nearly T-linear dependence of $\Delta\lambda(T)$. This is an important result indicating that the presence of line nodes in the superconducting gap is a robust signature in this P-substituted system. Another feature of the doping dependence of $\Delta\lambda$ is that the relative slope is the steepest for x = 0.30, about which we will discuss

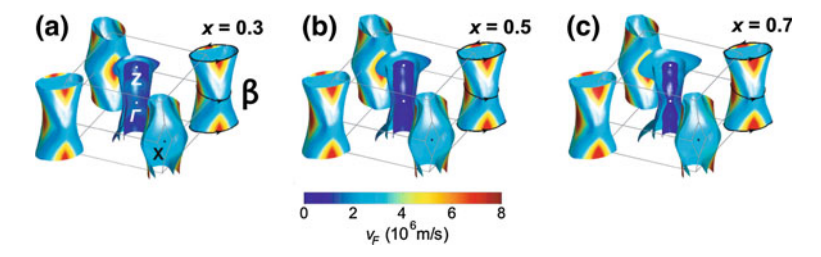


Fig. 5.14 Fermi surface of BaFe₂(As_{1-x}P_x)₂ with **a** x = 0.3, **b** 0.5, **c** and 0.7 from the band-structure calculation using a density functional theory implemented in the WIEN2K code. The *shading* represents the in-plane Fermi velocity v_F . The flat parts of the outer electron sheets have high v_F values. The *lines* represent the extremal β -orbit

in the next section in terms of a quantum critical behavior inside the superconducting dome.

For further investigation, we have calculated the band structure using a density functional theory implemented in the WIEN2K code for x=0.3, 0.5 and 0.7 (see Fig. 5.14). The obtained Fermi surface consists of five quasi-cylindrical pockets: three hole pockets at the center of the Brillouin zone, and two electron pockets centered at its corners. The shading of Fig. 5.14 represents the magnitude of v_F^{ab} ; the red (blue) area denotes regions with high (low) Fermi velocity. It can be seen that the hole pockets have low velocity and heavy-mass quasiparticles, whereas the electron pockets have high velocity and light-mass quasiparticles. Moreover, the band structure calculations with doping reveal that while the hole sheets show substantial warping with the P substitution, the electron sheets don't change the shapes with increasing the concentrations x. Since the penetration depth is dominated by the region with higher Fermi velocity v_F , the robustness of the presence of line nodes in BaFe₂(As_{1-x}P_x)₂ over a wide range of x implies little change in v_F at the near-nodal regions. Therefore, we infer that the nodes are located on the electron sheets rather than the hole sheets whose shapes significantly change with x.

5.3.4 Detailed Gap Structure of BaFe₂($As_{1-x}P_x$)₂

5.3.4.1 Nodes Being on the Electron Sheets

Considering the robustness of the presence of line nodes in BaFe₂($As_{1-x}P_x$)₂, the scenario with the nodes being on the electron sheets rather than the hole sheets is most likely in this system. This has been supported by several experiments. Recent bulk-sensitive laser-ARPES experiments [35] report isotropic gaps in all three hole pockets around the Z point. Three hole sheets around the Z point have been observed by using circularly polarized laser. The temperature dependence of the energy distribution curves at k_F for the outer Fermi surface shows the opening of the superconducting

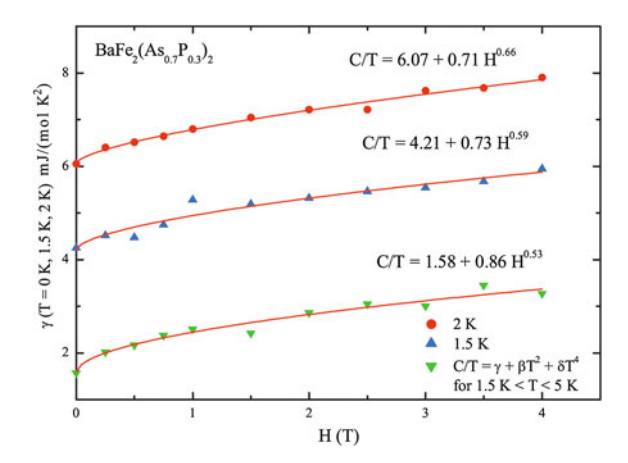


Fig. 5.15 Low-field electronic specific heat coefficient γ for BaFe₂(As_{0.7}P_{0.3})₂ up to 4T at 2K (*circles*) and 1.5 K (up triangles). *Down triangles* indicate the data for $T \to 0$ K. The fitting functions of the data are also shown. The figure is taken from Ref. [36]

gap below T_c . The superconducting gap magnitude Δ is directly extracted from the fitting procedure using the BCS spectral function. The obtained Δ value is in excellent agreement with the BCS-like T-dependence. The angle dependence of Δ of the three hole sheets, which indicates the fully gapped nature of these Fermi surface sheets. This result rules out the d-wave gap symmetry in BaFe₂(As_{1-x}P_x)₂ and strongly supports the possible presence of line nodes in the electron sheets around zone corners.

A comparison of the field dependence of κ/T with that of C/T also suggests the presence of nodes on the electron sheets. Figure 5.15 shows the field dependence of the electronic specific heat coefficient $\gamma = C/T$ at low fields for BaFe₂(As_{0.7}P_{0.3})₂ [36]. While the residual κ/T in the magnetic field exhibits a clear \sqrt{H} dependence over a much wider range, the residual specific heat C/T shows a moderate increase and nearly linear-dependence above 5T. This suggests that the nodes are located in regions with higher in-plane Fermi velocity v_F^{ab} , since the quasiparticles near the regions with higher in-plane Fermi velocity give a lower relative contribution to C/T (proportional to the DOS, $N(\varepsilon_F, H)$) than to thermal transport (proportional to $N(\varepsilon_F)(v_F^{ab})^2$). The shading of Fig. 5.16a represents the magnitude of v_F^{ab} for BaFe₂(As_{0.67}P_{0.33})₂ [37]. The red (blue) area denote regions with high (low) Fermi velocity. As mentioned above, the hole pockets have low velocity and heavy mass, while the electron Fermi surface sheets have high velocity and light mass. Considering that the electron pockets have a lower scattering rate than the hole pockets, their contribution to the total thermal conductivity is even more pronounced. Note that these regions with high v_F^{ab} also have a higher Doppler shift for $H \perp ab$. Therefore, these observations strongly support the scenario with the nodes on the electron sheet. Figure 5.16b, c show $N(\varepsilon_F)$ ($\propto C/T$) and $N(\varepsilon_F)(v_F^{ab})^2$) ($\propto \kappa/T$) as a function of v_E^{ab} . The gray shaded areas indicate the high velocity regions with

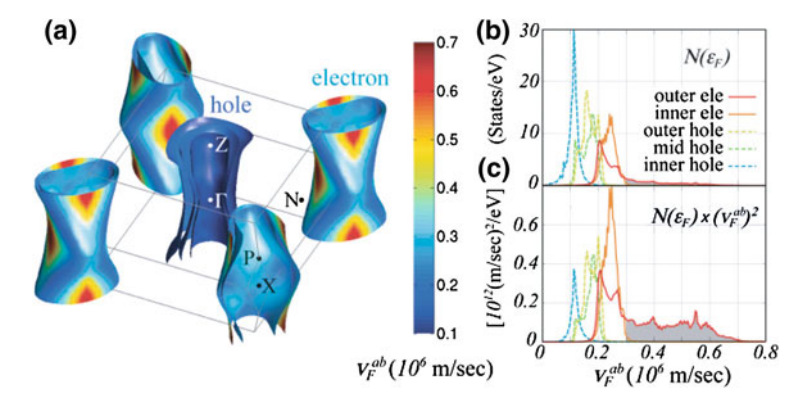


Fig. 5.16 a Fermi surface of BaFe₂(As_{0.67}P_{0.33})₂. The *shading* represents the magnitude of the in-plane Fermi velocity v_F^{ab} , **b**, **c** The density of states, $N(\varepsilon_F)$, and $N(\varepsilon_F)(v_F^{ab})^2$ of each band, which are proportional to C/T and κ/T , respectively, are plotted as a function of v_F^{ab} . The flat parts of the outer electron sheets in **a** are the regions with high v_F^{ab} values, which correspond to the *gray shading* in **b** and **c**. The figure is taken from Ref. [37]

 $v_F^{ab} \ge 0.3 \times 10^6$ m/s, flat parts in the outer electron sheets. Although their contribution is less than 5% in the total DOS (C/T), it exceeds 30% in κ/T . Importantly, this analysis suggests that the nodes may be located in the flat parts in the outer electron sheets where the Fermi velocity is highest.

5.3.4.2 Looped Line Nodes in the Outer Electron Sheet

Recent angle-resolved thermal conductivity measurements in a magnetic field rotated within the basal plane for BaFe₂(As_{0.67}P_{0.33})₂ [37] have revealed the detailed superconducting gap structure, which is also consistent with the robustness of the presence of nodes on the electron sheets. Figure 5.17a shows the angular dependence of $\kappa(\phi)$, where ϕ is the angle between the a axis and the magnetic field H. It is clear that $\kappa(\phi)$ shows minima at $\phi = \pm 45^{\circ}$, which indicates the presence of fourfold modulation. As shown by the solid lines, $\kappa(\phi)$ at each T and H can be fitted to $\kappa(\phi) = \kappa_0 + \kappa_{2\phi} + \kappa_{4\phi}$, where κ_0 is a constant, and $\kappa_{2\phi} = C_{2\phi} \cos 2\phi$ and $\kappa_{4\phi} = C_{4\phi} \cos 4\phi$ are the terms with twofold and fourfold symmetry, respectively. The twofold contribution can be attributed to the difference in transport with the field parallel to and normal to the heat current, which is present even for an isotropic gap. Figure 5.17c-h show $\kappa_{4\phi}/\kappa_n$ at low T and low H. It can be seen that clear fourfold oscillations with the amplitude $|C_{4\phi}|/\kappa_n \sim 0.01$ –0.02 are observed. Such oscillations are due to the creation of unpaired quasiparticles in the regions with small or vanishing gaps by the applied field. The strength of the pair breaking in a given near-nodal region vanishes when the Fermi velocity v_F is parallel to H, and becomes maximal when v_F is perpendicular to H. This can be explained by the Doppler shift of the quasiparticle energy by the

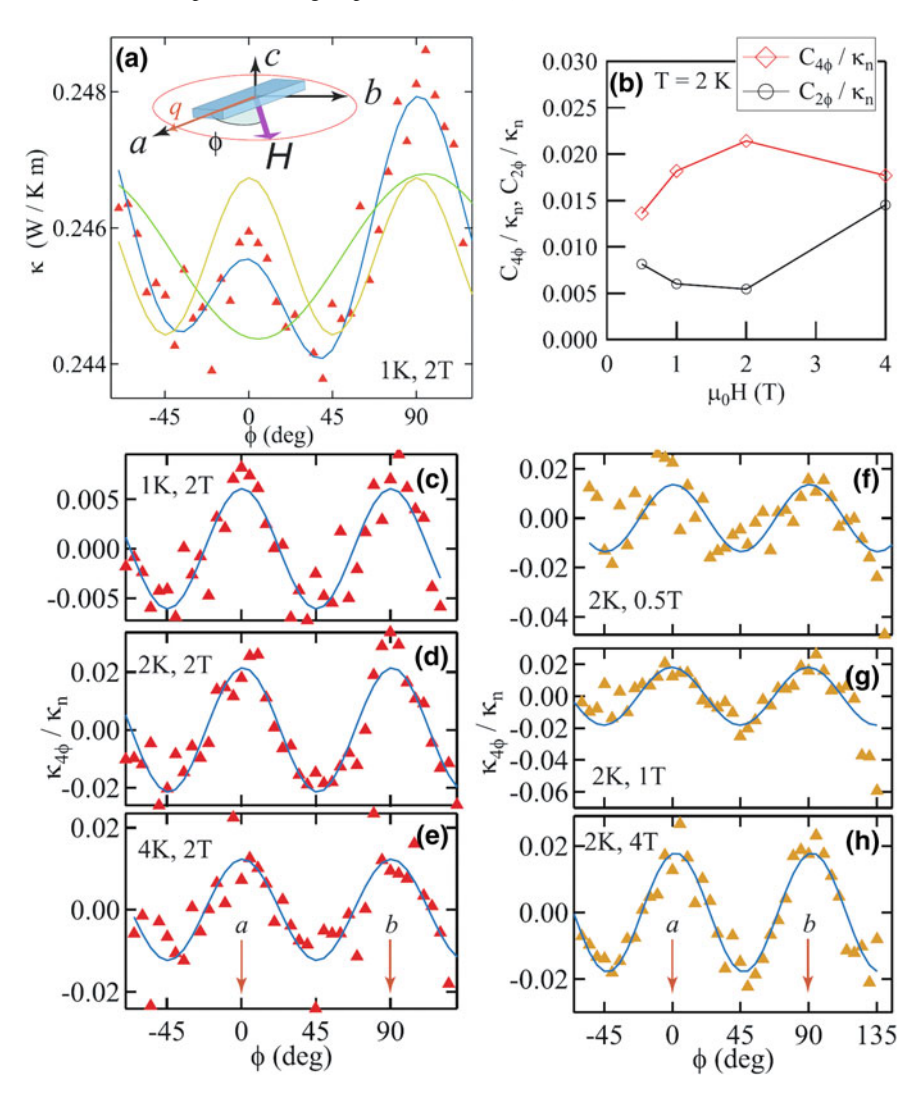


Fig. 5.17 a Angular variation of $\kappa(\phi)$ in BaFe₂(As_{0.67}P_{0.33})₂. The *blue solid line* represents the fit to $\kappa(\phi) = \kappa_0 + \kappa_{2\phi} + \kappa_{4\phi}$. The *sinusoidal curves* with one minimum (two minima) represent the twofold (fourfold) term obtained by the fitting. The *inset* shows the definition of the angle θ . **b** The magnitudes of $\kappa_{2\phi}$ and $\kappa_{4\phi}$ at 2 K as a function of the fields. **c**-**e** The fourfold term $\kappa_{4\phi}$ at 2 T and at several temperatures. **f**-**h** The fourfold term $\kappa_{4\phi}$ at 2 K and several magnetic fields. The figure is taken from Ref. [37]

amount $\delta \varepsilon(r, v_F) = v_F(k) \cdot p_s(r)$, where p_s is the superflow due to the vortices in the plane normal to H. Hence rotating H provides a probe of the node positions.

The profile of $\kappa(\phi)$ under a rotated field allows us to explore the positions of nodes. The fourfold oscillations of $\kappa(\phi)$ of similar amplitude to that in materials with vertical

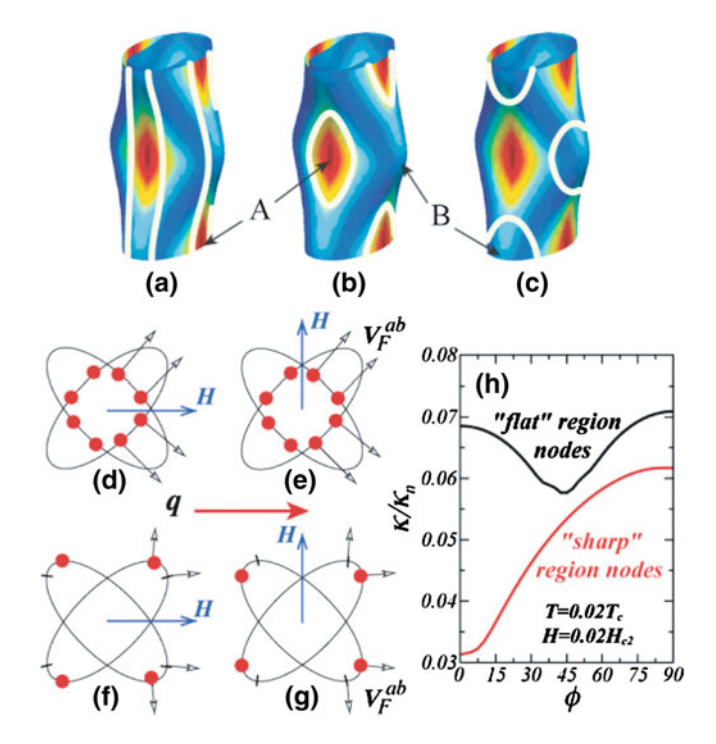


Fig. 5.18 a-c Possible positions of nodes on the electron Fermi surface. For $k_z=0$ and $\pm 2\pi/c$, cross sections of the electron surface are approximately elliptical. **d**, **e** When the nodes are located on the flat part of the outer electron band, the field-induced states near all nodes ($red\ circles$) have a comparable contribution to the heat current for H||q d and for $H\perp q$ e, so that the twofold component of κ is nearly absent. **f**, **g** When the nodes are on the sharp ends, the field-induced DOS is small for nodes with v_F nearly parallel to $H\ (crosses)$. The nodes with more quasiparticles (circles) have a different angle between v_F and q for the two field orientations, leading to a dominant twofold anisotropy. **h** Comparison of $\kappa(\theta)$ for the two cases with the scattering rate $\gamma = \Gamma/2\pi T_c = 0.01$, phase shift of scattering $\delta = \pi/3$, and the ratio of interband to intraband scattering $\delta v = 0.9$. The figure is taken from Ref. [37]

line nodes argue against nearly horizontal line nodes suggested by several theories. Depending on the temperature and field range, either minima or maxima of $\kappa_{4\phi}$ can indicate nodal directions. The inversion of the oscillations reported in Fe(Se,Te) with a similar Fermi surface structure occurs at a much higher temperature and field than the present range $(0.03 \le T/T_c \le 0.13$ and $0.007 \le H/H_{c2} \le 0.06$). Therefore the minima at $\phi = \pm 45^{\circ}$ observed in the present low-T and low-T range indicate that the nodes are located at the position of the Fermi surface where ν_F is nearly parallel to $[\pm \pi/a, \pm \pi/a, 0]$ directions.

In the '122' system, the k_z cuts of electron sheets are elliptical with twofold symmetry because of the body-centered tetragonal symmetry. These ellipses are rotated by 90° between $k_z = 0$ and $\pm 2\pi/c$, forming the so-called 'snake that swallowed a chain 'shape. As shown in Fig. 5.18a–c, flat regions appear in the electron

pockets around point A (along Γ -X) and the Fermi surface has a higher curvature near point B. In the A_{1g} symmetry we consider three possible nodal structures shown in Figs. 5.18a-c; (a) eight vertical line nodes, (b) closed-loop line nodes in the flat part, and (c) nodal loops in the high curvature part. To distinguish among these possible gap structures, the profile of the thermal conductivity has been calculated as a function of the field angle by using the microscopic approach generalized to the multiband system, which has been successful in describing C/T and κ/T oscillations. For simplicity we assume one electron sheet with nodes and one hole Fermi surface that is fully gapped. The obtained results are shown in Fig. 5.18h, which can be interpreted by an intuitive physical analysis. The two ellipsoids in Fig. 5.18d-g represent the electron sheets at $(\pi/a, \pi/a)$ and $(\pi/a, -\pi/a)$ points, respectively. In an applied magnetic field, quasiparticles are predominantly generated at locations where $v_F \perp H$ (filled red circles) and quasiparticles with $v_F \parallel q$ contribute more to the heat transport. If the nodes are on the high curvature region as in the case of Fig. 5.18c, the Fermi velocities at the nodes are not parallel. For the field parallel (normal) to the heat current, the majority of unpaired states have v_F nearly normal (parallel) to the heat current (Fig. 5.18f, g), yielding a dominant twofold component (see the lower curve in Fig. 5.18h). In contrast, the nodes on the flat part of the ellipse as in the case of Fig. 5.18b have a nearly identical direction of the Fermi velocity (Fig. 5.18d, e), and contribute equally to the q for both $H \parallel q$ and $H \perp q$ (see the upper curve in Fig. 5.18h). Thus, the observation of a large fourfold component with minima near $\pm 45^{\circ}$ eliminates the possibility of the nodal loops at the sharp edges of the Fermi surface (Fig. 5.18c). It also argues against vertical line nodes (Fig. 5.18a) as this gap structure would essentially average the two curves in Fig. 5.18h, which leads to a large twofold anisotropy not seen in the experiment. Therefore the observed results are most consistent with the closed nodal loops located at the flat parts of the electron Fermi surface with high Fermi velocity.

Finally we discuss why such a nodal loop structure is realized. Experimentally, recent neutron-scattering measurements suggest that the line nodes should create only a limited area of sign reversal on a single Fermi surface [39], which is consistent with the present nodal loop structure. The Raman scattering measurements for $Ba(Fe_{1-x}Co_x)_2As_2$ [38] have suggested a similar gap structure. A number of model calculations predict that the superconducting gap in the electron Fermi surfaces can be more anisotropic than that in hole bands, and that nodes can appear in some parameter range. In that case, formation of the nodes in the flat regions with low DOS does not significantly reduce the superconducting condensation energy. In addition, it has been suggested that the nesting between the Fermi surface regions with the same orbital character is important for the pairing interaction. We note that the change of the orbital character from xy to xz + yz occurs near the rim of the flat part of the electron pocket (see Fig. 5.19), implying that the orbital character may favor the closed-loop nodes. Thus the pairing interaction and low DOS stabilize the nodal loop structure with no serious reduction of T_c . A more detailed fully microscopic calculation is required to clarify the origin of the closed nodal loop structure.

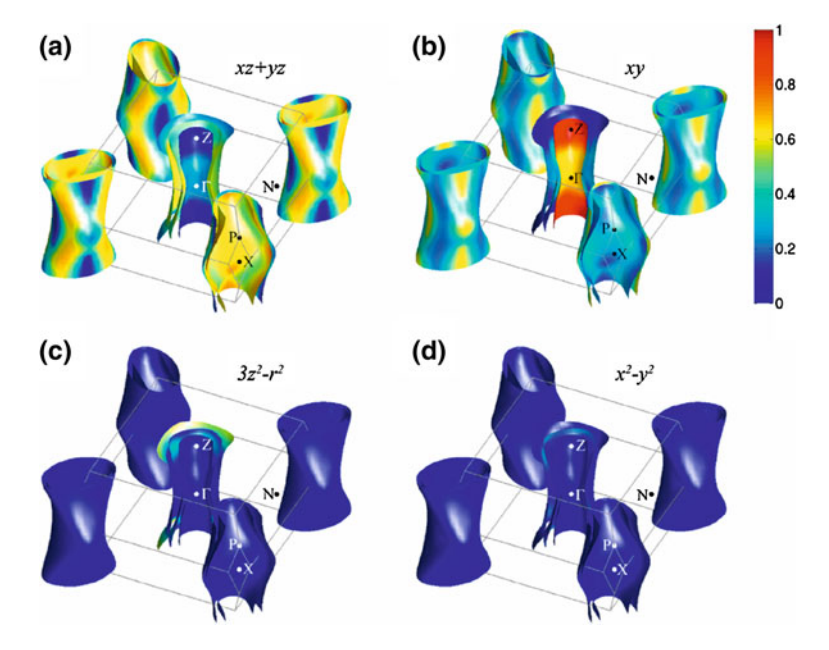


Fig. 5.19 Calculated Fermi surfaces of BaFe₂(As_{0.67}P_{0.33})₂. *Color* indicates the relative weigh of **a** the d_{xz+yz} orbital, **b** d_{xy} orbital, **c** $d_{3z^2-r^2}$ orbital, **d** and $d_{x^2-y^2}$ orbital contribution

5.4 Results and Discussion 2: Quantum Critical Point Beneath the Superconducting Dome

Investigating the QCP inside the superconducting dome is an experimentally challenging task, because most physical quantities vanish below T_c . Although non-Fermi liquid properties have been reported in BaFe₂(As_{1-x}P_x)₂ by several experiments, all of them have been performed in the normal state above the superconducting dome. It is therefore required to study systematically the superfluid response in the zero-temperature limit, which can be accessible by the measurements of the absolute penetration depth $\lambda(0)$.

For a reliable determination of the absolute value of $\lambda(0)$ in small single crystals, we adopted three different methods. The first is the lower- T_c material coating method [24, 25], in which $\lambda(0)$ is determined from the frequency shift of the tunnel diode oscillator containing the BaFe₂(As_{1-x}P_x)₂ crystal coated with aluminum film ($T_c = 1.2 \,\mathrm{K}$) of known thickness and penetration depth. In Fig. 5.20 we show the temperature dependence of the penetration depth for the optimally doped BaFe₂(As_{0.7}P_{0.3})₂ sample coated with the Al film of thickness of ~100 nm. Above $T_c^{\mathrm{Al}} = 1.2 \,\mathrm{K}$, the normal-state skin depth of Al ($\delta_{\mathrm{Al}} \sim 75 \,\mathrm{\mu}\,\mathrm{m}$ for $\rho_0^{\mathrm{Al}} = 10 \,\mathrm{\mu}\,\Omega$ cm at 13 MHz) is much larger than the thickness of the Al film. Therefore, the penetration depth of the coated sample, $\lambda_{\mathrm{eff}}(T)$, is almost identical to the penetration depth $\lambda(T)$ before the Al coating on the sample. On the other hand, when the Al film is super-

Fig. 5.20 The temperature dependence of the effective penetration depth for the optimally doped BaFe₂(As_{0.7}P_{0.3})₂ sample coated with Al film. The *inset* shows the low-temperature region. The overall variation of the penetration depth blow the Al transition, denoted as L, is used for the calculation of $\lambda(0)$

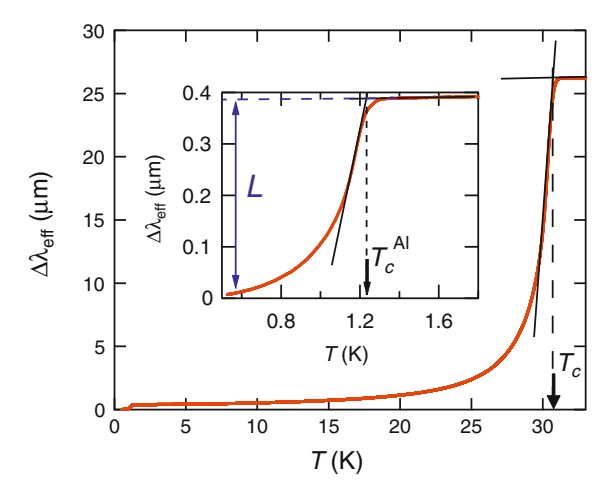
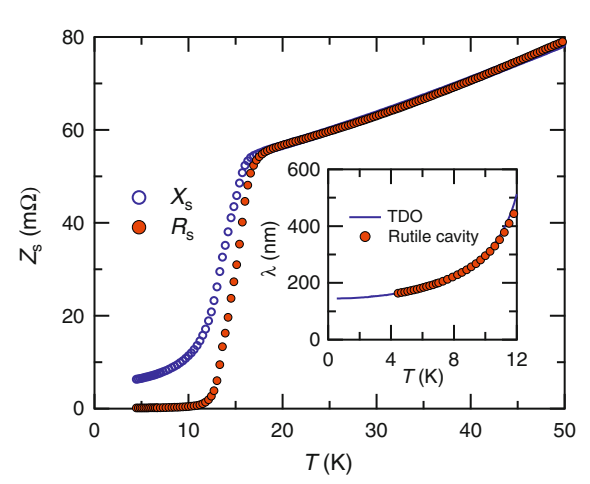


Fig. 5.21 Surface resistance R_s and reactance X_s as a function of the temperature at 5 GHz for x = 0.56. In the normal state, $R_s = X_s$ is observed. *Inset* shows the temperature dependence of the absolute penetration depth. *Solid line* represents the TDO data measured down to 80 mK on the same single crystal



conducting $(T < T_c^{\rm Al})$, Al acts together with the coated superconductor to screen the magnetic fields. Then, the effective magnetic penetration depth into both the Al film and the coated superconductor for $T < T_c^{\rm Al}$ can be given by Eq. 4.26. The overall penetration depth change below the Al transition $L \equiv \Delta \lambda_{\rm eff}(T) = \lambda_{\rm eff}(T) - \lambda_{\rm eff}(T_{\rm min})$, where $\lambda(T)$ is the penetration depth of the coated superconductor and $\lambda_{\rm Al}(T)$ is the penetration depth of the Al film, is used for the calculation of $\lambda(0)$, which gives $\lambda(0) = 330\,{\rm nm}$ for x = 0.3. The obtained results for the other concentrations x are summarized in Fig. 5.22a (black diamonds).

The second is the microwave cavity perturbation technique, in which $\lambda(0)$ is determined from the measurements of surface impedance, $Z_s = R_s + iX_s$, by using a superconducting resonator (with the resonant frequency $\omega/2\pi \approx 28\,\mathrm{GHz}$) and a rutile cavity resonator (5 GHz), both of which have very high quality factor $Q \sim 10^6$. In Fig. 5.21 we show the typical temperature dependence of the sur-

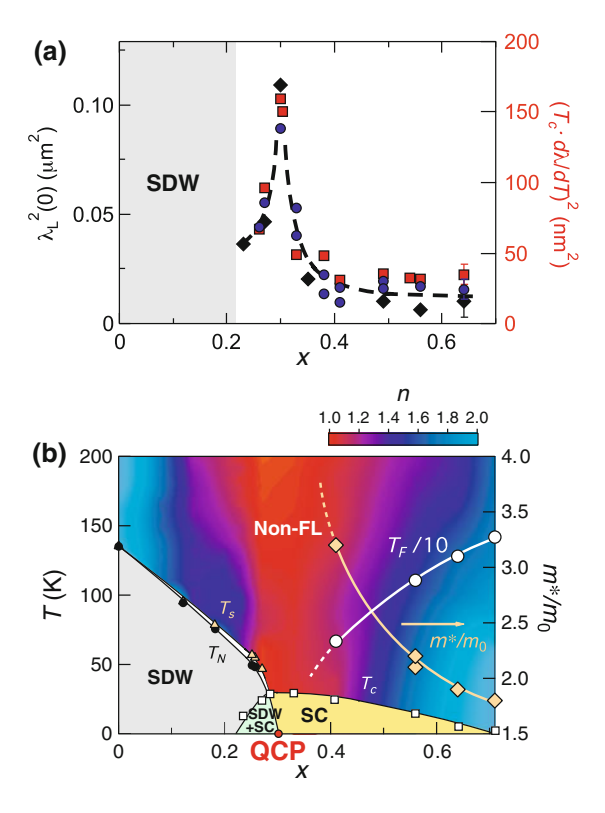


Fig. 5.22 a Doping evolution of the penetration depth $\lambda(0)$ in the zero-temperature limit determined by three different methods; Aluminum coating method (black diamonds), microwave cavity perturbation technique (blue squares), and the low-temperature slope of the relative change of the penetration depth with temperature (red squares, right hand scale). The right axis corresponds to the left axis if we assume a d-wave formula for nodal superconductors and BCS relation $\Delta=1.76k_BT_c$. b Phase diagram of BaFe₂(As_{1-x}P_x)₂. The red shaded region at around x=0.3 represents the region where the exponent n of the temperature dependence of the resistivity, $\rho_{dc}(T)=\rho(0)+AT^n$, is close to unity, which is a hallmark of the non-Fermi liquid (non-FL). The doping dependence of the effective Fermi temperature T_F (left axis) and renormalized mass m_e^*/m_0 (right axis) determined by dHvA oscillations arising from the β -orbit (see Fig. 5.14) are also shown

face resistance R_s and reactance X_s for the x=0.56 sample. In the normal state where $\omega \tau$ is much smaller than unity (Hagen-Rubens limit), $R_s=X_s$ is expected from the relation $R_s=X_s=\sqrt{\mu_0\omega\rho_{dc}/2}$. Such a behavior is indeed observed in Fig. 5.21. As shown in Fig. 5.21, the data shows a low residual R_s value in the low-temperature limit, which indicates high quality of the crystal. We note that the transition in microwave is intrinsically broader than that in dc resistivity data since the applied GHz microwave excites additional quasiparticles just below T_c . In the superconducting state well below T_c , $\lambda(T)$ is obtained by the surface reactance via the relation $X_s(T)=\mu_0\omega\lambda(T)$. The absolute value of X_s is determined from Z_s and dc-resistivity ρ_{dc} in the normal state by the relation $R_s=X_s=\sqrt{\mu_0\omega\rho_{dc}/2}$. The inset of Fig. 5.21 shows the temperature dependence of the absolute penetration

depth for the x = 0.56 sample, which shows extremely good agreement with the TDO data. The data is extrapolated down to zero temperature from the TDO data measured down to 80 mK, which gives $\lambda(0) = 135$ nm. The obtained results are also summarized in Fig. 5.22a (blue circles).

In addition to the above two direct methods, we also evaluate $\lambda(0)$ from the low-temperature slope of the relative change in the penetration depth with temperature, $\Delta\lambda(T) = \lambda(T) - \lambda(0)$, measured by the tunnel diode oscillator down to $\sim 80\,\mathrm{mK}$ (see Fig. 5.13). As discussed above, for all samples measured covering a wide range of concentrations $0.26 \le x \le 0.64$, the quasi-T-linear variation of $\Delta\lambda(T)$ is observed. A remarkable feature of the nearly linear-dependence of $i\Delta\lambda(T)$ is that the relative slope is the steepest for x=0.30 (Fig. 5.13b). This slope is related to $\lambda(0)$ and the superconducting energy gap magnitude $i\Delta_{\mathrm{gap}}$: for a d-wave nodal superconductor one may derive $\frac{\Delta\lambda(T)}{\lambda(0)} = \frac{\ln 2}{\Delta_{\mathrm{gap}}}k_BT$ [24]. By simply assuming this formula and the BCS relation $\Delta_{\mathrm{gap}} = 1.76k_BT_c$, we evaluate $\lambda(0)$ values (red squares in Fig. 5.22a). Although this simple assumption should be scrutinized, the obtained $\lambda(0)$ is close to the other data. The absolute values of $\lambda(0)$ determined by three different methods are thus quantitatively in good agreement in all x range of study.

Figure 5.22a shows the doping dependence of the squared in-plane penetration length $\lambda^2(0)$ in the zero-temperature limit. Its inverse $\lambda^{-2}(0)$ is given by the formula $\sum_{i} \mu_{0} n_{i} e^{2} / m_{i}^{*}$, where m_{i}^{*} and n_{i} are the effective mass and concentration of the superconducting carriers in the band i, respectively. The most notable feature $\lambda^2(0)$ shown in Fig. 5.22a is the sharp peak at x = 0.30, at about the same composition level where T_c is maximal. The prominent enhancement of $\lambda^2(0)$ is observed on approaching x = 0.30 from either side and has been seen in multiple samples by using different techniques. This reproducibility, combined with the above mentioned low $R_s(0)$, sharp superconducting transitions, and large heat capacity anomalies at all values of x close to x = 0.30 (8), shows that the enhancement is not an experimental artifact associated with poor screening caused by nonbulk superconductivity. We attribute the peak in $\lambda^2(0)$ to the existence of a OCP at x = 0.30. Generally, the penetration depth is dominated by the Fermi surface regions with large Fermi velocity. As shown by the shading in Fig. 5.14, the flat parts of the outer electron sheets, where the β -orbit mainly lies, have the highest Fermi velocity. The enhancement of $\lambda^2(0)$ is therefore likely to be closely related to the mass renormalization for $m_e^*(x)$ of the electron sheets revealed by the dHvA experiments in the normal state [18].

We stress that the critical behavior of $\lambda(0)$ has never been reported in any other superconductors, including heavy-fermion, cuprate and other iron-based superconductors. Even in the present system, no clear evidence for such a pronounced quantum critical behavior has been reported in the superconducting properties near T_c [40]. These may be related to the sharpness of the peak in $\lambda^2(0)$, suggesting that the fine tuning to the QCP both in the x and T axes is required to see the effect on the superconducting condensate. We note that the specific heat jump at T_c in based superconductors follows an unusual relation $\Delta C/T_c \propto T_c^2$ [20, 40, 41], which has been pointed out to be consistent with a normal state that is a quantum critical metal undergoing a pairing instability [42].

Our observation has profound implications for the superfluid in strongly correlated superconducting systems. How the strong electron correlations influence the condensed electron pairs in superconductors has been a long-standing issue [43–46]. In fact, it has been pointed out that in an ordinary one-component Galilean invariant Fermi liquid the electron correlation effect does not cause the renormalization of the mass responsible for the superfluid density [43]. On the other hand, the superfluid mass renormalization occurs in heavy-fermion superconductors, which contain interacting conduction electrons and local moments [44, 45]. The present results reveal that the electron correlation effect associated with the critical fluctuations near the QCP can lead to a striking mass renormalization of the superfluid in $BaFe_2(As_{1-x}P_x)_2$, in which the interaction between electron and hole pockets plays an important role for the electronic properties [21]. This calls for a new theory to explain the superfluid mass renormalization in this new strongly correlated multiband system.

We now discuss the consequences of a QPT inside the superconducting dome. Such a QPT implies that the non-Fermi liquid behavior indicated by the red region in 5.22b is most likely associated with a finite temperature quantum critical region linked to the QCP. Moreover, this transition immediately indicates two distinct superconducting ground states. The robust T-linear behavior of $\Delta\lambda(T)$ with the slope scaled by $\lambda(0)$ in both sides of the QCP argues against a drastic change in the superconducting gap symmetry [21, 22]. The fact that zero-temperature extrapolation of the antiferromagnetic transition $T_N(x)$ into the dome coincides with the location of the QCP (Fig. 5.22b) leads us to consider that the QCP separates the pure superconducting phase and the superconducting phase coexisting with the spin density wave (SDW). There has been much debate as to whether superconductivity coexists with magnetic ordering not only in based superconductors but also in cuprates, heavy fermions and other exotic superconductors, because of the difficulty to distinguish from mesoscopic phase separation. The present results revealing the QCP strongly suggests that superconductivity and SDW coexist on a microscopic level, but compete for the same electrons in the underdoped region. This is evidenced by the overall larger $\lambda(0)$ values in the SDW side of the QCP than the other side (see Fig. 5.22a), corresponding to the smaller volume of Fermi surface due to the SDW gapping. The microscopic coexistence is also supported by the enhancement of $\lambda^2(0)$ with approaching the QCP from the SDW side, which is not expected in the case of phase separation.

To place BaFe₂(As_{1-x}P_x)₂ in the context of other superconductors, we plotted T_c as a function of the effective Fermi temperature T_F for several types of compounds (Uemura plot, Fig. 5.23); the red symbols correspond to various values of x for BaFe₂(As_{1-x}P_x)₂studied here, and the others are obtained from mSR measurements reported previously [47]. Because the relevant Fermi surface sheets are nearly cylindrical, T_F for two-dimensional (2D) systems may be estimated directly from the superfluid density $\lambda^{-2}(0)$ via the relation, $T_F = (\hbar^2 \pi) n_{2D}/k_B m^* \approx \hbar^2 \pi/\mu_0 e^2 d\lambda^2(0)$, where n_{2D} is the carrier concentration within the superconducting planes and d is the interlayer spacing; $T_F = (\hbar^2/2)(3\pi^2)^{2/3}n^{2/3}/k_B m^*$ for 3D systems [47]. The dashed line in Fig. 5.23 corresponds to the Bose-Einstein condensation (BEC) tem-

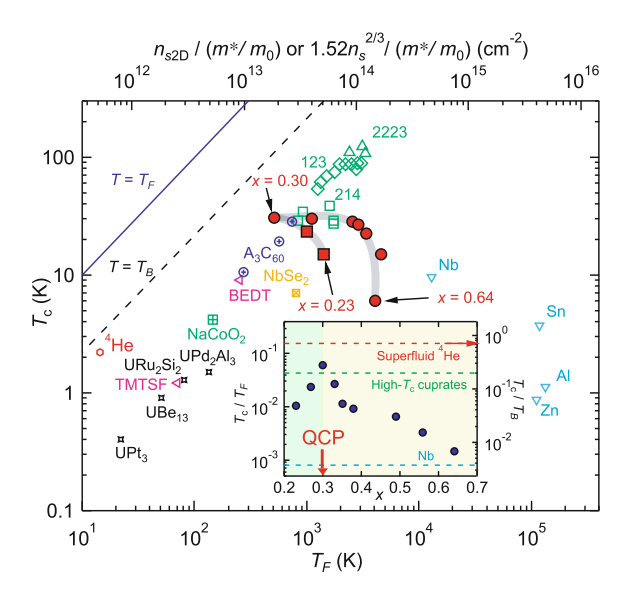


Fig. 5.23 The so-called Uemura-plot. T_c is plotted as a function of effective Fermi temperature T_F evaluated from the superfluid density for various superconductors $(n_{2D}/(m^*/m_0))$ for 2D and $1.52n/(m^*/m_0)$ for 3D systems, where m_0 is the free electron mass) [47]. We used an average of the Al-coating and microwave data. The present data in BaFe₂(As_{1-x}P_x)₂ for $x \ge 0.30$ (red circles) and for x < 0.30 (red squares) bridge a gap between the conventional superconductors such as Nb and cuprate high- T_c superconductors such as (La, Sr)₂CuO₄ (214), YBa₂Cu₃O_{7-\delta} (123), and Bi₂Sr₂Ca₂Cu₃O_y (2223). x = 0.3 represents the data at the QCP. The dashed line is the BEC temperature for the ideal 3D boson gas. The inset shows the doping dependence of T_c normalized by the Fermi temperature (left axis) or BEC temperature (right axis). Yellow and black dashed lines mark the T_c/T_F values for underdoped cuprates 123 and for the conventional superconductor Nb. Green arrow represents $T_c/T_B = 0.7$ for superfluid ⁴He

perature for ideal 3D boson gas, $T_B = \frac{\hbar^2}{2\pi m^* k_B} (\frac{n}{2.612})^{2/3} = 0.0176 T_F$. In quasi-2D system, this value of T_B provides an estimate of the maximum condensate temperature. The evolution of the superfluid density in the present system is in sharp contrast to that in cuprates, in which T_c is roughly scaled by T_F . The inset of Fig. 5.23 depicts the P-composition dependence of T_c normalized by Fermi (or BEC) temperature, $T_c/T_F(T_c/T_B)$. In the large composition region (x>0.6), T_c/T_F is very small, comparable to that of conventional superconductor Nb. As x is decreased, T_c/T_F increases rapidly, and then decreases in the SDW region after reaching the maximum at the QCP (x=0.3). What is remarkable is that the magnitude of $T_c/T_B(\simeq 0.3)$ at the QCP exceeds that of cuprates and reaches as large as nearly 40% of the value of superfluid 4 He.

The fact that T_c/T_F , and hence Δ/ε_F , becomes largest at the QCP indicates that the strongest pairing interaction is achieved at the QCP, which provide direct evidence that the high- T_c superconductivity is favored by the QCP in iron-based superconductors. In a multiband system, we need to introduce the effective Fermi energy ε_F for each band, which is defined for electron (hole) bands as the energy of

5.5 Summary 91

the highest occupied state relative to the bottom (top) of the band. Since the outer electron sheet with the highest Fermi velocity has the largest ε_F and hence mostly contributes to the superfluid density, the magnitude of T_c/T_F in the other sheets are expected to be even larger. These results lead us to consider that in terms of T_c/T_F the system is closer to the BCS-BEC crossover [48] than the cuprates, in which phase fluctuations are important for determining T_c [49]. A possible crossover towards the BEC driven by the QCP may cause unexpected phenomena of superconductivity. The extremely large Δ/ε_F value indicates that BaFe₂(As_{0.7}P_{0.3})₂ may be in the region where any other superconductors could not access. For instance, this may lead to highly unusual superconducting states with anomalous vortex core and superclean vortex dynamics are expected.

5.5 Summary

In this study we have performed high precision measurements of the magnetic penetration depth in $BaFe_2(As_{1-x}P_x)_2$ over a wide range of x, which provide strong evidence that this material has line nodes in its energy gap. We find that the presence of line nodes in the superconducting gap is a robust signature in this P-substituted system, which is consistent with the nodes being on the electron sheets rather than the hole sheets whose shapes significantly change with x. By combining several results for the isovalent-doped $BaFe_2(As_{1-x}P_x)_2$, we conclude that the observed results are most consistent with the closed nodal loops located at the flat parts of the electron Fermi surface with high Fermi velocity.

We have also reported the zero-temperature anomaly of the superconducting condensate in very clean BaFe₂(As_{1-x}P_x)₂ crystals that reveals the first convincing signature of a second-order quantum phase transition deep inside the dome. We find that the x-dependence of the penetration depth exhibits a sharp peak at the optimum composition x = 0.30 ($T_c = 30$ K), demonstrating pronounced quantum fluctuations associated with the QCP, which separates two distinct superconducting phases. Moreover, the ratio of T_c/T_F at x = 0.3 marks the highest record among superconductors exceeding the cuprate case and even approaches the superfluid ⁴He value, implying a possible crossover towards the Bose-Einstein condensate driven by quantum criticality.

References

- 1. I.I. Mazin, D.J. Singh, M.D. Johannes, M.H. Du, Phys. Rev. Lett. 101, 057003 (2008)
- K. Kuroki, S. Onari, R. Arita, H. Usui, Y. Tanaka, H. Kontani, H. Aoki, Phys. Rev. Lett. 101, 087004 (2008)
- 3. K. Hashimoto, T. Shibauchi, S. Kasahara, K. Ikada, S. Tonegawa, T. Kato, R. Okazaki, C.J. van der Beek, M. Konczykowski, H. Takeya, K. Hirata, T. Terashima, Y. Matsuda, Phys. Rev. Lett. **102**, 207001 (2009)

- K. Hashimoto, T. Shibauchi, S. Kasahara, K. Ikada, T. Kato, R. Okazaki, C.J. van der Beek, M. Konczykowski, H. Takeya, K. Hirata, T. Terashima, Y. Matsuda, Phys. Rev. Lett. 102, 207001 (2009)
- X.G. Luo, M.A. Tanatar, J.-Ph. Reid, H. Shakeripour, N. Doiron-Leyraud, N. Ni, S. L. Bud'ko, P. C. Canfield, H. Luo, Z. Wang, H.-H. Wen, R. Prozorov, L. Taillefer, Phys. Rev. B 80, 140503(R) (2009)
- H. Ding, P. Richard, K. Nakayama, T. Sugawara, T. Arakane, Y. Sekiba, A. Takayama, S. Souma, T. Sato, T. Takahashi, Z. Wang, X. Dai, Z. Fang, G.F. Chen, J. L. Luo, N.L. Wang, Europhys. Lett. 83, 47001 (2008)
- R.T. Gordon, C. Martin, H. Kim, N. Ni, M.A. Tanatar, J. Schmalian, I.I. Mazin, S.L. Bud'ko, P.C. Canfield, R. Prozorov, Phys. Rev. B 79, 100506(R) (2009)
- 8. C. Martin, R.T. Gordon, M.A. Tanatar, H. Kim, N. Ni, S.L. Bud'ko, P.C. Canfield, H. Luo, H.H. Wen, Z. Wang, A.B. Vorontsov, V.G. Kogan, R. Prozorov, Phys. Rev. B 80, 020501(R) (2009)
- 9. A.B. Vorontsov, M.G. Vavilov, A.V. Chubukov, Phys. Rev. B 79, 140507(R) (2009)
- 10. Y. Bang, Europhys. Lett. **86**, 47001 (2009)
- D.S. Inosov, J.T. Park, P. Bourges, D.L. Sun, Y. Sidis, A. Schneidewind, K. Hradil, D. Haug, C.T. Lin, B. Keimer, V. Hinkov, Nat. Phys. 6, 178 (2009)
- A.D. Christianson, E.A. Goremychkin, R. Osborn, S. Rosenkranz, M.D. Lumsden, C.D. Malliakas, I.S. Todorov, H. Claus, D.Y. Chung, M.G. Kanatzidis, R.I. Bewley, T. Guidi, Nature (London) 456, 930 (2008)
- 13. S. Onari, H. Kontani, M. Sato, Phys. Rev. B 81, 060504(R) (2010)
- J.D. Fletcher, A. Serafin, L. Malone, J.G. Analytis, J.-H. Chu, A.S. Erickson, I.R. Fisher, A. Carrington, Phys. Rev. Lett. 102, 147001 (2009)
- C.W. Hicks, T.M. Lippman, M.E. Huber, J.G. Analytis, J.-H. Chu, A.S. Erickson, I.R. Fisher, K.A. Moler, Phys. Rev. Lett. 103, 127003 (2009)
- M. Yamashita, N. Nakata, Y. Senshu, S. Tonegawa, K. Ikada, K. Hashimoto, H. Sugawara, T. Shibauchi, Y. Matsuda, Phys. Rev. B 80, 220509(R) (2009)
- 17. S. Kasahara, T. Shibauchi, K. Hashimoto, K. Ikada, S. Tonegawa, H. Ikeda, H. Takeya, K. Hirata, T. Terashima, Y. Matsuda, Phys. Rev. B **81**, 184519 (2010)
- H. Shishido, A.F. Bangura, A.I. Coldea, S. Tonegawa, K. Hashimoto, S. Kasahara, P.M.C. Rourke, H. Ikeda, T. Terashima, R. Settai, Y. Onuki, D. Vignolles, C. Proust, B. Vignolle, A. McCollam, Y. Matsuda, T. Shibauchi, A. Carrington, Phys. Rev. Lett. 104, 057008 (2010)
- T. Yoshida, I. Nishi, S. Ideta, A. Fujimori, M. Kubota, K. Ono, S. Kasahara, T. Shibauchi, T. Terashima, Y. Matsuda, H. Ikeda, R. Arita, Phys. Rev. Lett. 106, 117001 (2011)
- 20. G.R. Stewart, Rev. Mod. Phys. 83, 1589 (2011)
- 21. P.J. Hirschfeld, M.M. Korshunov, I.I. Mazin, Rep. Prog. Phys. 74, 124508 (2011)
- 22. R.M. Fernandes, J. Schmalian, Phys. Rev. B 82, 014521 (2010)
- Y. Nakai, T. Iye, S. Kitagawa, K. Ishida, H. Ikeda, S. Kasahara, H. Shishido, T. Shibauchi, Y. Matsuda, T. Terashima, Phys. Rev. Lett. 105, 107003 (2010)
- 24. R. Prozorov, R.W. Giannetta, Supercond. Sci. Technol. 19, R41 (2006)
- R.T. Gordon, H. Kim, N. Salovich, R.W. Giannetta, R.M. Fernandes, V.G. Kogan, T. Prozorov, S.L. Bud'ko, P.C. Canfield, M.A. Tanatar, R. Prozorov, Phys. Rev. B 82, 054507 (2010)
- 26. W.N. Hardy, D.A. Bonn, D.C. Morgan, R. Liang, K. Zhang, Phys. Rev. Lett. 70, 3999 (1993)
- 27. P.J. Hirschfeld, Nigel Goldenfeld, Phys. Rev. B 48, 4219 (1993)
- N. Kurita, F. Ronning, C.F. Miclea, E.D. Bauer, J.D. Thompson, A.S. Sefat, M.A. McGuire, B.C. Sales, D. Mandrus, R. Movshovich, Phys. Rev. B 79, 214439 (2009)
- 29. M.J. Graf, S.-K. Yip, J.A. Sauls, D. Rainer, Phys. Rev. B 53, 15147 (1996)
- K. Hashimoto, M. Yamashita, S. Kasahara, Y. Senshu, N. Nakata, S. Tonegawa, K. Ikada, A. Serafin, A. Carrington, T. Terashima, H. Ikeda, T. Shibauchi, Y. Matsuda, Phys. Rev. B 81, 220501(R) (2010)
- 31. C. Proust, E. Boaknin, R.W. Hill, L. Taillefer, A.P. Mackenzie, Phys. Rev. Lett. 89, 147003 (2002)
- 32. J. Lowell, J.B. Sousa, J. Low Temp. Phys. **3**, 65–87 (1970)

References 93

- 33. G.E. Volovik, JETP Lett. 58, 469 (1993)
- 34. Y. Nakai, T. Iye, S. Kitagawa, K. Ishida, S. Kasahara, T. Shibauchi, Y. Matsuda, T. Terashima, Phys. Rev. B 81, 020503(R) (2010)
- T. Shimojima, F. Sakaguchi, K. Ishizaka, Y. Ishida, T. Kiss, M. Okawa, T. Togashi, C.-T. Chen,
 S. Watanabe, M. Arita, K. Shimada, H. Namatame, M. Taniguchi, K. Ohgushi, S. Kasahara, T.
 Terashima, T. Shibauchi, Y. Matsuda, A. Chainani, S. Shin, Science 332, 564 (2011)
- Y. Wang, J.S. Kim, G.R. Stewart, P.J. Hirschfeld, S. Graser, S. Kasahara, T. Terashima, Y. Matsuda, T. Shibauchi, I. Vekhter, Phys. Rev. B 84, 184524 (2011)
- M. Yamashita, Y. Senshu, T. Shibauchi, S. Kasaharsa, K. Hashimoto, D. Watanabe, H. Ikeda, T. Terashima, I. Vekhter, A.B. Vorontsov, Y. Matsuda, Phys. Rev. B 84, 060507(R) (2011)
- I.I. Mazin, T.P. Devereaux, J.G. Analytis, J.H. Chu, I.R. Fisher, B. Muschler, R. Hackl, Phys. Rev. B 82, 180502(R) (2010)
- M. Ishikado, Y. Nagai, K. Kodama, R. Kajimoto, M. Nakamura, Y. Inamura, S. Wakimoto, H. Nakamura, M. Machida, K. Suzuki, H. Usui, K. Kuroki, A. Iyo, H. Eisaki, M. Arai, S. Shamoto, Phys. Rev. B 84, 144517 (2011)
- C. Chaparro, L. Fang, H. Claus, A. Rydh, G.W. Crabtree, V. Stanev, W.K. Kwok, U. Welp Phys. Rev. B 85, 184525 (2012)
- 41. S.L. Bud'ko, N. Ni, P.C. Canfield, Phys. Rev. B 79, 220516(R) (2009)
- 42. J. Zaanen, Phys. Rev. B 80, 212502 (2009)
- 43. A.J. Leggett, Phys. Rev. 140, A1869 (1965)
- 44. C.M. Varma, K. Miyake, S. Schmitt-Rink, Phys. Rev. Lett. 57, 626 (1986)
- 45. F. Gross, B.S. Chandrasekhar, D. Einzel, K. Andres, P.J. Hirschfeld, H.R. Ott, J. Beuers, Z. Fisk, J.L. Smith, Z. Phys, B **64**, 175 (1986)
- 46. Y. Yanase, T. Jujo, T. Nomura, H. Ikeda, T. Hotta, K. Yamada Phys, Rep. 378, 1 (2003)
- 47. Y.J. Uemura, J. Phys. Condens. Matter 16, S4515 (2004)
- 48. Q. Chen, J. Stajic, S. Tan, K. Levin, Phys. Rep. 412, 1 (2005)
- 49. V.J. Emery, S.A. Kivelson, Nature **374**, 434 (1995)

Chapter 6 Superconducting Gap Nodes in the ZoneCentered Hole Bands of KFe₂As₂

Abstract In this chapter, we show the results of the end member of the hole-doped system, KFe₂As₂, which has three zone-centered hole pockets and no electron Fermi surface but still exhibits superconductivity. We have performed measurements of the magnetic penetration depth in very clean single crystals of KFe₂As₂ with residual resistivity ratio $RRR \sim 1200$ by using the tunnel diode oscillator down to $80 \, \text{mK}$. A steep temperature dependence of $\lambda(T)$ at low temperatures indicates the existence of low-energy excitations in KFe₂As₂, which is totally different from the flat temperature behavior observed in the optimally doped $(Ba_{1-x}K_x)Fe_2As_2$. Our analysis based on the DFT band calculation and dHvA results reveals that this material has well formed line nodes located in the Γ -centered hole bands.

Keywords Heavily hole-doped system \cdot KFe₂As₂ \cdot Magnetici penetration depth \cdot Superconducting gap structure \cdot Line nodes

6.1 The End Member KFe₂As₂ in the Hole-Doped System

In most iron-based superconductors there are disconnected quasi-two-dimensional hole and electron Fermi surfaces. The former are centered on the Γ point in the Brillouin zone and the latter at the zone corner. Based on analyses of spin-fluctuation mediated pairing models, strong scattering between the electron and hole sheets, corresponding to a wavevector $q \sim (\pi, \pi)$ leads to a nodeless gap with sign change between the hole and electron sheets (nodeless s_{\pm} state) [1, 2]. Indeed, in certain materials such as optimally doped (Ba_{1-x}K_x)Fe₂As₂ and Ba(Fe_{1-x}Co_x)₂As₂ strong evidence for fully gapped superconductivity has been observed in several experiments. However, if in addition to this there is strong low q scattering this can stabilize a state with nodes in the electron and/or hole bands with either s or d-wave symmetry [2–4]. c-axis Fermi-surface dispersion could also generate horizontal line nodes [3, 5]. In BaFe₂(As_{1-x}P_x)₂, strong evidence of line nodes in the gap has been

obtained from the penetration depth and thermal conductivity measurements [6]. Moreover, recent angle resolved thermal conductivity measurements [7] suggest that the nodes are most likely located on the electron bands near the zone corner of the Brillouin zone, and that the hole bands centered at the Γ point remains fully gapped. Thus, the rich variety of possible pairing states has as its origin the small difference of the unusual multiband electronic structure in the iron-based superconductors.

KFe₂As₂, which is the end member of the hole-doped $(Ba_{1-x}K_x)$ Fe₂As₂ series, is an intriguing material in itself. Figure 6.1 shows the schematic phase diagram of the holed doped $(Ba_{1-x}K_x)Fe_2As_2$ system. The striking feature is that superconductivity $(T_c \sim 3 \text{ K})$ occurs even for x = 1 although substantial hole-doping (one hole per unit cell) causes an significant change in the Fermi surface topology. Figure 6.2a depicts the electronic structure of KFe₂As₂ determined by ARPES measurements, as well as that of the optimally doped Ba_{0.6}K_{0.4}Fe₂As_{2.} [8]. The Fermi surface topology at the X point is dramatically changed for x = 1 due to an excess of hole doping: the ubiquitous X centered electron sheets are replaced by small quasi-two-dimensional hole-like tubes which do not nest at all with the Γ -centered hole sheets. This marked difference can be explained by a simple energy shift due to hole doping (see Fig. 6.2b). Two distinct hole pockets centered at Γ point and small hole blades near X point have also been observed in dHvA measurements [9]. Recent laser ARPES measurements [10] have resolved three hole pockets centered at Γ point. The electronic structure with three hole pockets at Γ point and hole blades at X point is consistent with the DFT band calculation for KFe₂As₂ and with the trends observed in ARPES studies of $(Ba_{1-x}K_x)Fe_2As_2$ with increasing x [8].

If nesting between hole and electron pockets does play an important role in the superconductivity of the high- T_c iron-based superconductors, then the nature of the superconducting state may be quite different in KFe₂As₂. The ⁷⁵As nuclear quadrupole resonance (NQR) and specific heat measurements using a polycrystalline sample

Fig. 6.1 Schematic phase diagram of $(Ba_{1-x}K_x)Fe_2As_2$ against the K content x

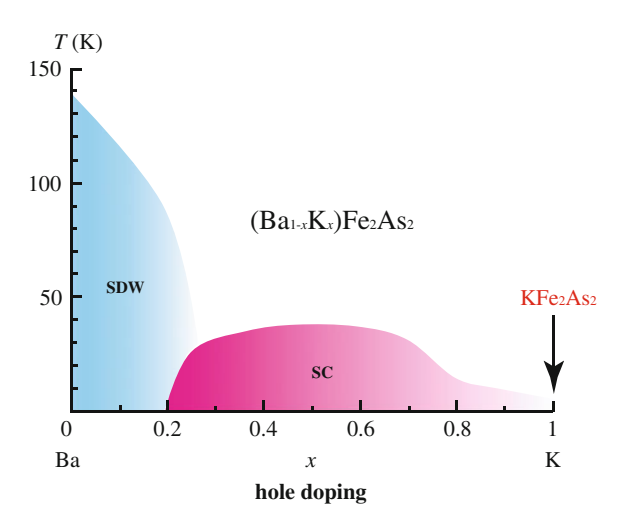
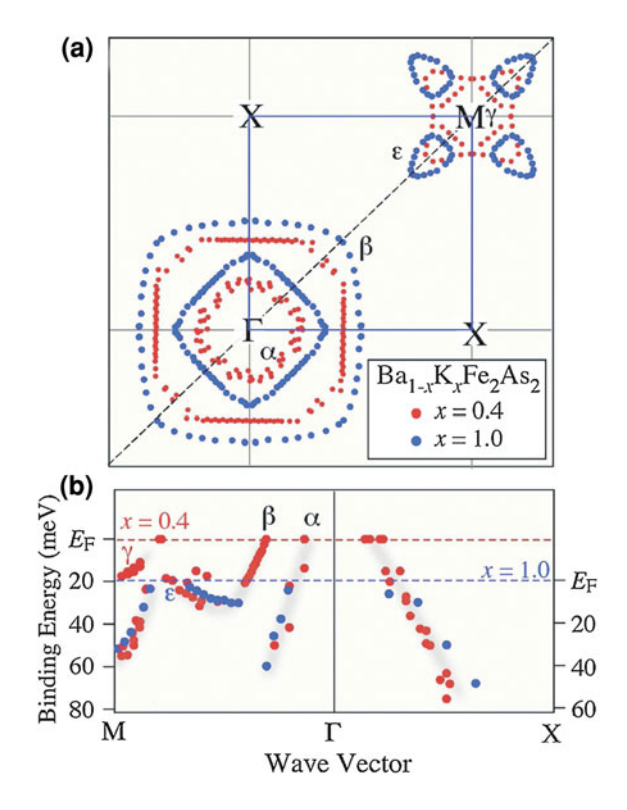


Fig. 6.2 a Comparison of experimentally determined Fermi surfaces between KFe₂As₂ (*blue circle*) and optimally doped Ba_{0.6}K_{0.4}Fe₂As₂ (*red circle*). b Experimental band dispersion in the vicinity of *E_F* for two high-symmetry *lines*. The chemical potential of the KFe₂As₂ sample is shifted downward with respect to that of the Ba_{0.6}K_{0.4}Fe₂As₂ sample. The figure is taken from Ref. [8]



of KFe₂As₂ [11] have revealed the presence of low-energy quasiparticle excitations, in contrast to the optimally doped (Ba_{1-x}K_x)Fe₂As₂. Figure 6.3a shows the spin-lattice relaxation rate $1/T_1$ in the superconducting state. $1/T_1$ follows $T^{1.4}$ down to 0.6 K below T_c and decreases more steeply at lower temperatures. Such an unusual behavior cannot be explained by a simple two-gap model with a nodeless s_{\pm} -wave state, which suggests the existence of line nodes in KFe₂As₂ (see Fig. 6.3a). Alternatively, the data can be well reproduced by two-gap models with nodal gap(s) (see the inset of Fig. 6.3a). This two-gap superconductivity with nodal gap(s) has also been observed in the specific heat measurement. Figure 6.3b displays the temperature dependence of C/T. A small jump, which is about 30% of the electronic specific heat coefficient just below T_c , can be reproduced by the two-gap superconductivity with nodal gap(s). A large residual value of C/T at the lowest temperature ($\sim 0.1 T_c$) also indicates the existence of low-energy quasiparticle excitations.

Furthermore, thermal conductivity measurements using a single crystal of KFe₂As₂ have also suggested nodal superconductivity [12]. Figure 6.4a shows the temperature dependence of κ_0/T at several magnetic fields. In zero field, a large residual linear term κ_0/T is observed, which is totally different from the negligibly small κ_0/T observed in the optimally doped (Ba_{1-x}K_x)Fe₂As₂. Moreover, a very small magnetic field has significantly increased the κ_0/T , while at high fields κ_0/T tends to saturate. Such a rapid increase of κ_0/T at low field is similar to the behavior

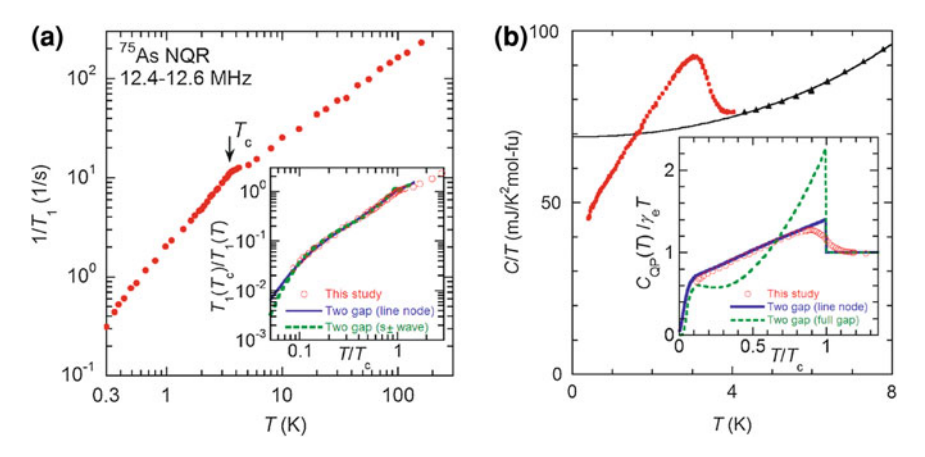


Fig. 6.3 a Temperature dependence of $1/T_1$ for KFe₂As₂. The *inset* shows the data normalized by $1/T_1(T_c)$. The *solid* and *dashed lines* represent the fits to the two-gap model with nodeless and nodal order parameters, respectively. **b** Temperature dependence of C/T for KFe₂As₂. The *solid line* represents the fit to $C/T = \gamma + \beta T^2 + \varepsilon T^4$. The inset shows $C(T)/\gamma_e T$ as a function of T/T_c . The fits to the two-gap model with nodeless (*solid line*) and nodal (*dashed line*) order parameters are shown. The figure is taken from Ref. [11]

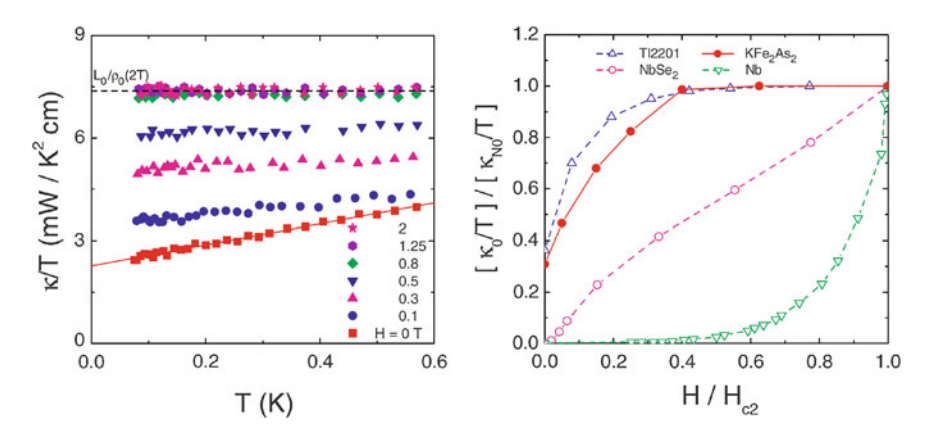


Fig. 6.4 a Low-temperature in-plane thermal conductivity of KFe₂As₂ in magnetic fields applied along the c axis. The *solid line* is the fit to $\kappa/T=a+bT$ for the data at zero magnetic field. The *dashed line* represents the normal state Wiedemann-Franz law. **b** Normalized residual term of κ_0/T in KFe₂As₂ as a function of H/H_{c2} . Similar data of the clean s-wave superconductor Nb, multiband s-wave superconductor NbSe₂, and overdoped sample of the d-wave superconductor Tl-2201 are also shown for comparison. The figure is taken from Ref. [12]

of Tl-2201 and provides clear evidence for unconventional superconducting gap with nodes in KFe_2As_2 .

Thus far, although several experiments have provided strong evidence for unconventional superconductivity with line nodes in KFe₂As, detailed information on the superconducting gap structure, especially where the nodes are located, is still lacking. Since the presence of nodes in the energy gap signals an unconventional pairing mechanism, and the position of the nodes can be a strong guide as the exact form of the pairing interaction $V_{kk'}$, its identification is of utmost importance. In this study, we have performed measurements of the temperature dependent penetration depth in KFe₂As₂, which shows that this material has well formed line nodes located in the Γ -centered hole bands.

6.2 Experimental

Single crystals of KFe₂As₂ were provided by Professor Kohori's group at Chiba University and Professor Eisaki's group at National Institute of Advanced Industrial Science and Technology (AIST) in Tsukuba. High quality single crystals were grown by a K-flux method. dc resistivity measurements ware performed by a standard 4-probe method. Au contacts were evaporated after Ar plasma cleaning of the surface, which give contact resistance less than 1 Ω . Figure 6.5a shows the temperature dependence of dc resistivity $\rho(T)$ measurements, which indicates that our crystals are extremely clean with the residual resistivity ratio $RRR = \rho(300 \text{ K})/\rho_0$ of 1200.

In order to determine the bulk homogeneity of the superconductivity in our samples, specific heat measurements were performed on the same sample as was used

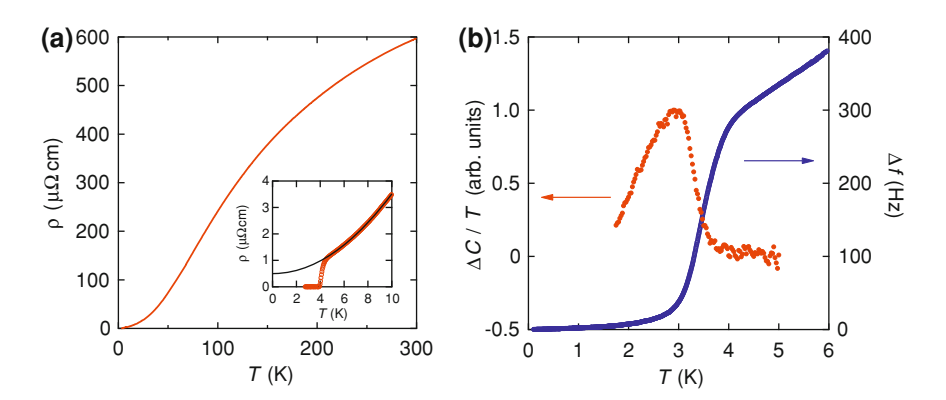


Fig. 6.5 a Temperature dependence of in-plane resistivity $\rho(T)$ in a single crystal of KFe₂As₂. Inset shows the low-temperature resistivity data. The solid line indicates a power law fit $\rho(T) = \rho_0 + AT^2$ with $\rho_0 = 0.5 \,\mu\,\Omega$ cm, $A = 0.030 \,\mu\,\Omega$ cm/K². b The frequency shift Δf of the oscillator (left axis), and relative change in the specific heat divided by temperature $\Delta C/T$ (right axis) in the same sample measured by a modulated temperature method [13]

for the penetration depth measurements. Because of the small size of these samples (mass ${\sim}4\,\mu g$), a modulated temperature method was used [13]. Briefly, the sample is glued to a $10\,\mu m$ diameter chromel-constantan thermocouple and heated with modulated light from a room temperature LED via an optical fiber. This method has a high sensitivity but has poor absolute accuracy, so the values are quoted in arbitrary units.

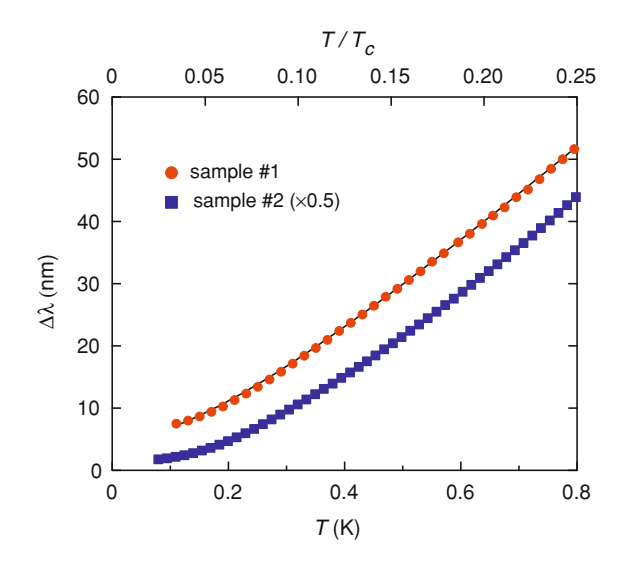
The temperature dependence of the magnetic penetration depth $\lambda(T)$ was measured using the tunnel diode oscillator in a dilution refrigerator. The ac magnetic field is applied parallel to the c axis so that the shielding currents flow in the ab-plane. To avoid degradation of the crystals due to reaction with moisture in the air, we cleaved the crystals on all six sides while they were coated in a thick layer of Apiezon N grease. The measurements were done just after the cleavage without exposure in air. The relatively sharp superconducting transitions found in the frequency shift of the oscillator as well as in the specific heat measured after the penetration depth measurements (see Fig. 6.5b) indicate that our procedure does not damage the sample quality.

6.3 Results and Discussion

6.3.1 Penetration Depth

Figure 6.6 shows the low-temperature variation of the in-plane magnetic penetration depth $\Delta\lambda(T) = \lambda(T) - \lambda(0)$ in two samples. In both samples a strong *T*-linear

Fig. 6.6 Change in the penetration depth $\Delta\lambda(T)$ at low temperatures in two samples. The data are shifted vertically for clarity. Solid lines indicate fits to the empirical formula $\Delta\lambda(T) \approx T^2/(T+T^*)$ with $T^*=0.3$ and 0.5 K for sample #1 and sample #2, respectively



dependence is observed over a wide temperature range of $0.1 \lesssim T/T_c \lesssim 0.25$. Such a strong T-linear dependence is distinctly different from the exponential dependence expected in the fully-gapped superconducting state and is instead consistent with gap with well-developed line nodes. A linear temperature dependence can only be explained by the presence of line nodes [14]. This is in contrast to power law behaviors with exponents close to 2 which could be consistent either with nodal behavior in the dirty limit or with strong impurity scattering in the intrinsically fully gapped s_{\pm} state [14]. Evidence for line nodes in this compound has also been found in NMR, specific heat [11] and thermal conductivity [12] measurements, as mentioned above.

Deviations from the T-linear behavior of $\lambda(T)$ are observed at the lowest temperatures which are likely due to a finite zero-energy density of states created by a small amount of impurity scattering. When impurity scattering is present in superconductors with line nodes, the low-temperature $\Delta\lambda(T)$ changes from T to T^2 , which can be described by the empirical formula $\Delta\lambda(T) \propto T^2/(T+T^*)$ [15]. A fit to this formula (solid lines in Fig. 6.6) gives $T^* \approx 0.3$ K for sample #1 and $T^* \approx 0.5$ K for sample #2, which indicates relatively small levels of disorder in these crystals.

Although the temperature dependence of λ is consistent between samples the absolute values of $d\lambda/dT$ differ by a factor two. Our calibration procedure linking the measured frequency shift to the change in λ has proved to be highly accurate (~5–10%) for polycrystalline elemental test samples and high- T_c cuprate superconductors such as YBa₂Cu₃O_{7- δ} [16, 17]. However, in some cases where there is large surface roughness of the cut edges $\Delta\lambda$ may be overestimated. We obtain almost identical temperature dependence of the normalized superfluid density $\lambda^2(0)/\lambda^2(T)$ if we use the doubled $\lambda(0)$ value for sample #2 (see the inset of Fig. 6.7). This indicates that the only calibration factor has a factor of two differences between the two samples and the whole temperature dependence is quite reproducible. A similar effect was found in LaFePO ([18]) and NbSe₂ [18]. The lower value found for sample #1 is likely to be more representative of the intrinsic value although in LaFePO the values of $\Delta\lambda$ found by scanning SQUID spectrometry [19] were around a factor two smaller than the lowest estimate [18].

6.3.2 Superfluid Density

To evaluate the normalized superfluid density $\rho_s(T) = \lambda^2(0)/\lambda^2(T)$, we need the value of $\lambda(0)$. Recent small-angle neutron scattering (SANS) measurements [20] estimate $\lambda(T=55\,\mathrm{mK})\approx200\,\mathrm{nm}$ and $\mu\mathrm{SR}$ measurements [21] give $\lambda(T_c/2)\approx280\,\mathrm{nm}$ which also suggests $\lambda(0)\sim200\,\mathrm{nm}$. These values are close to the $\lambda(0)$ values calculated from the Fermi surface parameters as will be discussed below (see Table 6.1). Regardless of the choice of $\lambda(0)$ value within the uncertainties, the obtained temperature dependence of $\rho_s(T)$ shows a T-linear behavior over a even wider temperature range than $\lambda(T)$ itself (see Figs. 6.7 and 6.9). This is expected because the $1-\alpha(T/T_c)$ dependence of $\rho_s(T)$ gives $\Delta\lambda(T)/\lambda(0)=\frac{1}{2}\alpha(T/T_c)+\frac{3}{8}\alpha^2(T/T_c)^2+\cdots$ which

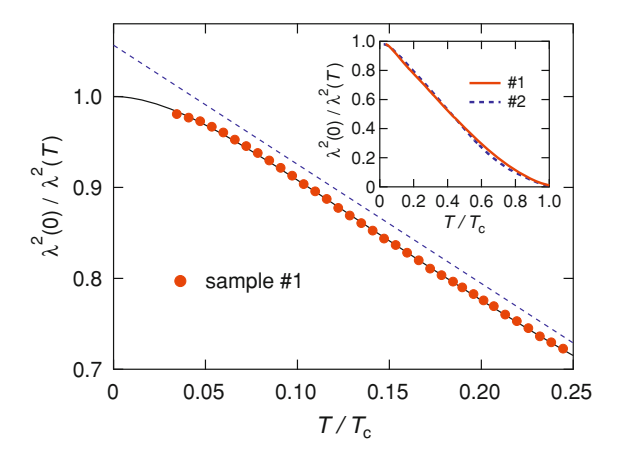


Fig. 6.7 Normalized superfluid density at low temperatures follows a T-linear dependence (dashed line). We used $\lambda(0)=260$ nm estimated from the Fermi-surface parameters. The solid lines are fits to the empirical formula involving the impurity scattering in superconductors with line nodes (see text). Inset compares the normalized superfluid density data for the two samples. To account for the factor of two difference in the slope of $\Delta\lambda(T)$ at low temperatures, we used the doubled $\lambda(0)$ value for sample #2

Table 6.1 Contributions of each band to the normalized superfluid density $\lambda^2(0)/\lambda^2(T)$ evaluated from DFT band structure calculations as well as the dHvA measurements [9]

From DFT calculations					From dHvA			
Sheet	# holes	DOS (eV)	$\omega_p \; (\mathrm{eV})$	$\frac{\omega_p^2}{(\omega_p^2)^{\rm total}}$	Name	# holes	$\frac{m^*}{m_e}$	$\frac{\omega_p^2}{(\omega_p^2)^{\rm total}}$
1 (pillow at Z)	0.002	0.06	0.16	0.04	_	_	_	_
2 (inner tube at Γ)	0.258	1.11	1.47	0.32	α	0.17	6	0.31
3 (middle tube at Γ)	0.342	1.48	1.40	0.29	ζ	0.26	13	0.23
4 (outer tube at Γ)	0.390	1.52	1.51	0.34	β	0.48	18	0.31
5 (tubes near <i>X</i>)	0.009	1.33	0.55	0.05	ε	0.09	7	0.15
Total	1.00	5.50	2.59	1		1.0		1

 m_e is the free electron mass

leads to slightly concave (superlinear) temperature dependence for the penetration depth as we observed.

In order to proceed with a more quantitative analysis of our results we have estimated the contribution of each Fermi surface sheet to the total superfluid density from DFT calculations and dHvA results, respectively.

Estimation from DFT calculations:

As a first approach we have calculated the band structure of KFe₂As₂ using density functional theory (DFT) using the WIEN2K package [22] and the experimental lattice

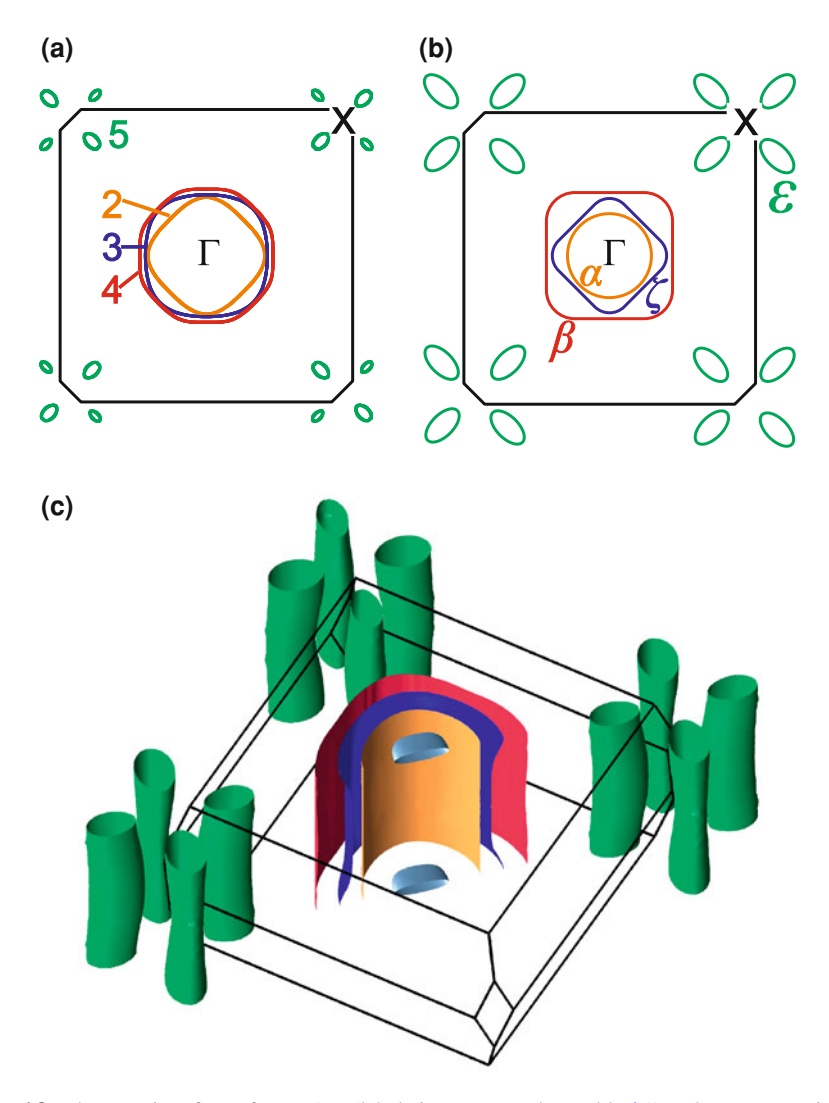


Fig. 6.8 The Fermi surface of KFe_2As_2 (labels in correspond to Table 6.1). **a** 2D cross-sectional representation of our band-structure calculations (note the pillow surface from band 1 does not appear in this cut). **b** Schematic cross-section with shapes of the various pockets determined by dHvA [9] and ARPES [8] experiments. **c** 3D view of the DFT calculated Fermi surface with bands energies shifted to best fit the dHvA frequencies (Rigid band energy shifts of 0, +20, -120, +50, +30 meV for bands 1-5 respectively were applied)

constants and internal positions [23]. 1 4 × 10 5 k points (in the full Brillouin zone) were used for the calculations of plasma frequencies ω_p , Fermi surface volumes, and sheet-specific density of states (DOS), which are reported in Table 6.1. The Fermi

 $^{^{1}}$ a = 3.841 Å, c = 13.861 Å, and z = 0.3525.

surface topology and band masses are very similar to those reported previously [9]. Also we show the calculated Fermi surface of KFe₂As₂ in Fig. 6.8a, c. The calculated total DOS and ω_p correspond to the Sommerfeld constant $\gamma=13.0\,\mathrm{mJ/K^2mol}$ and $\lambda(0)=76.6\,\mathrm{nm}$, respectively. The experimentally observed $\gamma=93\,\mathrm{mJ/K^2mol}$ (Ref. [11]) implies a renormalization of 7.2 in the total density of states at the Fermi level. Assuming that the superfluid density is renormalized by the same factor leads to $\lambda(0)$ being increased to 205 nm. Such a renormalization for the penetration depth $\lambda(0)$ in Galilean-invariant systems like liquid ³He is canceled by the Fermi-liquid parameter corrections [24], but in the electronic systems a large renormalization close to the thermodynamic mass enhancement is expected [25] and has been observed in heavy fermion systems [26].

Estimation from dHvA results:

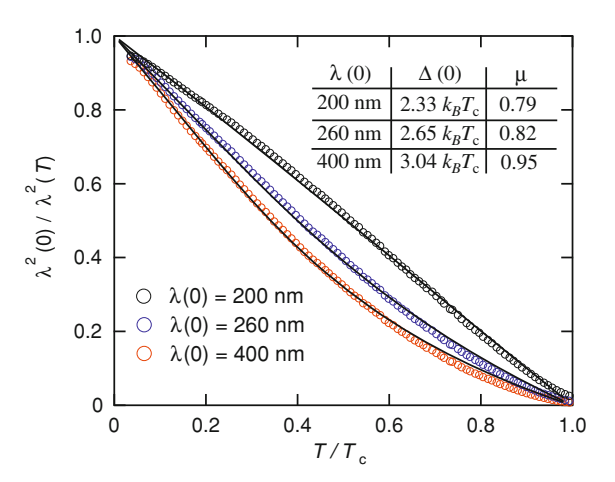
Although the general features of this Fermi surface calculation are confirmed by ARPES [8] and dHvA measurements [9], the exact size of the various sheets and their warping are not. Also, dHvA measurements show that the mass renormalization effects vary between the different sheets. So as a second approach we estimate the contribution of the various sheets to the superfluid density directly from the dHvA measurements, assuming each sheet is a simple two dimensional cylinder. As the largest β sheet was not observed by dHvA, we estimate its volume from the total hole number constraint and its mass by using the measured specific heat. Note that for sheets with more than one extremal dHvA orbit we have taken the average. Also we have ignored any possible contribution from the small pillow sheet (band 1: see Fig. 6.8 and Table 6.1). The contribution of each sheet to the superfluid density were then calculated using $\lambda^{-2} = \mu_0 e^2 n_H / m^* = \omega_p^2 / c^2$, where n_H and m^* are the hole density and effective mass for each sheet. From this we obtain a total superfluid density which corresponds to $\lambda(0) = 260 \,\mathrm{nm}$. The fact that this procedure and the direct calculation from the band structure (including renormalization) give values of $\lambda(0)$ which compare favorable to the direct measurements by μ SR and SANS gives us confidence in the accuracy of the result. A key result from this analysis is that the contribution of the ε band near the X point is small. It contributes only up to \sim 15% of the total superfluid density.

6.3.3 Position of the Nodes

The temperature dependence of the normalized superfluid density $\rho_s = \lambda^2(0)/\lambda^2(T)$ is plotted in Fig. 6.9. Here we have used values of $\lambda(0)$ which encompass the above estimates as well as a factor of 2 larger value in case that our values of $\Delta\lambda(T)$ are overestimated because of remaining surface roughness in sample #1. These plots show that the superfluid density at $T = T_c/3$ does not exceed ~75% of the zero-temperature value which indicates that the nodes are located on at least one of the Γ -centered bands which have large contributions to the superfluid density.

In a nodal superconductor a rapid decrease of superfluid density with increasing temperature is indicative of a small value of the gap slope near the nodes

Fig. 6.9 Normalized superfluid density obtained by using representative values of $\lambda(0)$. The *lines* are the fits to the nodal-gap model with parameters indicated in the figure



 $\mu\Delta_0=1/d\Delta/d\phi|_{\rm node}$ (in a simple d-wave model [27] for $T\ll T_c$: $\rho_s(T)\simeq 1-4\ln 2/\mu\Delta_0$). The presence of multiple Fermi surface sheets complicates the analysis in the present case, but it is reasonable to approximately model the gaps and Fermi velocity values on the different sheets by globally averaged values of μ and Δ . We then approximate the variation of the gap with in-plane Fermi surface angle ϕ by $\Delta(\phi)=\min(\mu\Delta_0\phi,\Delta_0)$ [27]. We note that for $\mu=2$ this produces a very similar form of $\rho_s(T/T_c)$ to the more usual d-wave form $\Delta(\phi)=\Delta_0\cos(2\phi)$. An alternative way of modeling the gap would be to add higher harmonics to this lowest order d-wave form. However, this would introduce more fitting parameters if more than one extra harmonic was required. In the weak-coupling limit, μ is the only free parameter in this model as the temperature dependent gap can be calculated self-consistently [27]. Here, however, we allow for possible strong-coupling corrections to Δ_0 and leave this as a free parameter, fixing the temperature dependence of Δ to its weak-coupling d-wave form.

As shown in Fig. 6.9, we find this model fits our data well for all assumed values of $\lambda(0)$. There is strong covariance between the two parameters μ and Δ_0 because the low T slope is determined only by the product $\mu\Delta_0$ whereas the variable ratio μ/Δ_0 influences the higher-temperature behavior only weakly. We find the data can also be reasonably well fitted by the inclusion of a second isotropic gap accounting for $\sim 30\,\%$ of the total, but the large reduction of ρ_s at low temperatures cannot be reproduced if we assume that only the ε tubes have line nodes as they only contribute $\sim 15\,\%$ to the total superfluid density. This reaffirms our conclusion that nodes must be present on the Γ centered hole bands, although there is a possibility that some of the sheets could be fully gapped. We note that recent laser ARPES measurements [10] have revealed octet-line nodes on the middle hole pocket (band 3 in Fig. 6.8) and an almost-zero gap on the outer hole pocket (band 4), which are consistent with the presence of line nodes in the energy gap on the large zone-centered hole sheets experimentally-derived from our measurements. Although the superconducting gap

structure of KFe₂As₂ is different both from the fully gapped superconducting state in (Ba,K)Fe₂As₂ and from the nodal state with line nodes in the electron sheet as in the case of BaFe₂(As,P)₂, the recent laser ARPES result that eight-fold sign reversal in the gap function is realized in KFe₂As₂ suggests that the non-universal superconducting gap structure in iron-pnictides can be interpreted in the framework of A_{1g} symmetry.

6.4 Summary

In summary, we have performed measurements of the magnetic penetration depth in very clean single crystals of KFe₂As₂ with residual resistivity ratio $RRR \sim 1200$ by using the tunnel diode oscillator down to 80 mK. A steep temperature dependence of $\lambda(T)$ at low temperatures indicates the existence of low-energy excitations in KFe₂As₂, which is totally different from the flat temperature behavior observed in the optimally doped (Ba_{1-x}K_x)Fe₂As₂. Our analysis based on the DFT band calculation and dHvA results reveals that there are line nodes in the energy gap on the large zone-centered hole sheets. This is different both from the nodeless states found in (Ba,K)Fe₂As₂ and from the nodal s state with nodes in the electron bands which may be the case in BaFe₂(As,P)₂. The recent laser ARPES result that eight-fold sign reversal in the gap function is realized in KFe₂As₂ suggests that the non-universal superconducting gap structure in iron-pnictides can be interpreted in the framework of A_{1g} symmetry. How this difference is linked to the changes in the Fermi surface will be an important clue towards a microscopic mechanism of superconductivity in iron-based superconductors.

References

- 1. I.I. Mazin, D.J. Singh, M.D. Johannes, M.H. Du, Phys. Rev. Lett. **101**, 057003 (2008)
- 2. K. Kuroki, H. Usui, S. Onari, R. Arita, H. Aoki, Phys. Rev. B 79, 224511 (2009)
- 3. S. Graser, A.F. Kemper, T.A. Maier, H.-P. Cheng, P.J. Hirschfeld, D.J. Scalapino, New J. Phys. 11, 025016 (2009)
- 4. A.V. Chubukov, M.G. Vavilov, A.B. Vorontsov, Phys. Rev. B 80, 140515(R) (2009)
- 5. L. Craco, M.S. Laad, Phys. Rev. B 80, 054520 (2009)
- K. Hashimoto, M. Yamashita, S. Kasahara, Y. Senshu, N. Nakata, S. Tonegawa, K. Ikada, A. Serafin, A. Carrington, T. Terashima, H. Ikeda, T. Shibauchi, Y. Matsuda, Phys. Rev. B 81, 220501(R) (2010)
- M. Yamashita, Y. Senshu, T. Shibauchi, S. Kasaharsa, K. Hashimoto, D. Watanabe, H. Ikeda, T. Terashima, I. Vekhter, A.B. Vorontsov, Y. Matsuda, Phys. Rev. B 84, 060507(R) (2011)
- 8. T. Sato, K. Nakayama, Y. Sekiba, P. Richard, Y.-M. Xu, S. Souma, T. Takahashi, G.F. Chen, J.L. Luo, N.L. Wang, H. Ding, Phys. Rev. Lett. 103, 047002 (2009)
- 9. T. Terashima, M. Kimata, N. Kurita, H. Satsukawa, A. Harada, K. Hazama, M. Imai, A. Sato, K. Kihou, C.-H. Lee, H. Kito, H. Eisaki, A. Iyo, T. Saito, H. Fukazawa, Y. Kohori, H. Harima, S. Uji, J. Phys. Soc. Jpn. **79**, 053702 (2010)

References 107

K. Okazaki, Y. Ota, Y. Kotani, W. Malaeb, Y. Ishida, T. Shimojima, T. Kiss, S. Watanabe, C.T. Chen, K. Kihou, C.H. Lee, A. Iyo, H. Eisaki, T. Saito, H. Fukazawa, Y. Kohori, K. Hashimoto, T. Shibauchi, Y. Matsuda, H. Ikeda, H. Miyahara, R. Arita, A. Chainani, S. Shin, Science 337, 1314 (2012)

- 11. H. Fukazawa, Y. Yamada, K. Kondo, T. Saito, Y. Kohori, K. Kuga, Y. Matsumoto, S. Nakatsuji, H.Kito, P.M. Shirage, K. Kihou, N. Takeshita, C.-H. Lee, A. Iyo, H. Eisaki, J. Phys. Soc. Jpn. 78, 083712 (2009)
- J.K. Dong, S.Y. Zhou, T.Y. Guan, H. Zhang, Y.F. Dai, X. Qiu, X.F. Wang, Y. He, X.H. Chen, S.Y. Li, Phys. Rev. Lett. 104, 087005 (2010)
- 13. A. Carrington, C. Marcenat, F. Bouquet, D. Colson, A. Bertinotti, J.F. Marucco, J. Hammann, Phys. Rev. B **55**, R8674 (1997)
- 14. A.B. Vorontsov, M.G. Vavilov, A.V. Chubukov, Phys. Rev. B 79, 140507(R) (2009)
- 15. P.J. Hirschfeld, N. Goldenfeld, Phys. Rev. B 48, 4219 (1993)
- 16. R. Prozorov, R.W. Gianetta, A. Carrington, F.M.A. Moreira, Phys. Rev. B 62, 115 (2000)
- A. Carrington, F. Manzano, R. Prozorov, R.W. Giannetta, N. Kameda, T. Tamegai, Phys. Rev. Lett. 86, 1074 (2001)
- J.D. Fletcher, A. Serafin, L. Malone, J.G. Analytis, J.-H. Chu, A.S. Erickson, I.R. Fisher, A. Carrington, Phys. Rev. Lett. 102, 147001 (2009)
- C.W. Hicks, T.M. Lippman, M.E. Huber, J.G. Analytis, J.-H. Chu, A.S. Erickson, I.R. Fisher, K.A. Moler, Phys. Rev. Lett. 103, 127003 (2009)
- H. Kawano-Furukawa, C.J. Bowell, J.S. White, R.W. Heslop, A.S. Cameron, E.M. Forgan, K. Kihou, C.H. Lee, A. Iyo, H. Eisaki, T. Saito, H. Fukazawa, Y. Kohori, R. Cubitt, C.D. Dewhurst, J.L. Gavilano, M. Zolliker, Phys. Rev. B 84, 024507 (2011)
- 21. K. Ohishi et al. (unpublished)
- P. Blaha, K. Schwarz, G.K.H. Madsen, D. Kvasnicka, J. Luitz, Wien2k. ISBN 3-9501031-1-2 (2001)
- 23. S. Rozca, H.U. Schuster, Z. Naturforsch. B 36, 1668 (1981)
- 24. A.J. Leggett, Phys. Rev. 140, A1869 (1965)
- 25. C.M. Varma, K. Miyake, S. Schmitt-Rink, Phys. Rev. Lett. 57, 626 (1986)
- F. Gross, B.S. Chandrasekhar, D. Einzel, K. Andres, P.J. Hirschfeld, H.R. Ott, J. Beuers, Z. Fisk, J.L. Smith, Z. Phys, B 64, 175 (1986)
- 27. D. Xu, S.K. Yip, J.A. Sauls, Phys. Rev. B **51**, 16233 (1995)

Chapter 7 Nodeless Versus Nodal Order Parameters in LiFeAs and LiFeP

Abstract In this chapter, we demonstrate the results of magnetic penetration depth measurements in the stoichiometric superconducting materials LiFeAs and LiFeP, which reveal contrasting behaviors. In LiFeAs the low-temperature penetration depth shows a flat dependence indicative of a fully gapped state. In contrast, LiFeP exhibits a T-linear dependence of $\lambda(T)$, indicating a nodal superconducting order parameter. We found that the stronger electron-electron correlations for LiFeAs than LiFeP from the Kadawaki-Woods relation, which is the opposite of the general trend that strong correlations usually promote sign change in the superconducting order parameter. Our analysis based on accumulated $\lambda(T)$ data in the 1111, 122, and 111 series of superconductors implies that the nodal state is induced when the pnictogen height from the iron plane decreases below a threshold value of \sim 1.33 Å. By comparing the electronic band structures of LiFeAs and LiFeP, we discuss the origin of the different gap structures in these materials.

Keywords Stoichiometric system \cdot LiFeAs \cdot LiFeP \cdot Magnetici penetration depth \cdot Superconducting gap structure \cdot Pnictogen-height

7.1 Stoichiometric Superconducting System LiFeAs and LiFeP

Soon after the discovery of the '1111' and '122' families, the so-called '111' compound LiFeAs was discovered to exhibit superconductivity ($T_c = 18 \,\mathrm{K}$) in stoichiometric composition without either structural or magnetic transitions [1]. It has a tetragonal Cu₂Sb-type crystal structure with space group P4/nmm. Recently, superconductivity ($T_c = 4.5 \,\mathrm{K}$) of its counterpart LiFeP [2, 3] was also reported. Since charge doping introduces scattering in the system, stoichiometric superconductivity is highly desirable to investigate the intrinsic nature of the pairing symmetry in the iron-based superconductors.

Identification of the particular electronic structure and characteristics which drive superconductivity in the iron-pnictides is of utmost importance. ARPES measurements in LiFeAs [4] for $k_z=0$ report two hole pockets near the zone center (Γ point) and two electron pockets near the zone corner (M point), but a significant discrepancy between the observed size of the hole sheets and the density functional theory (DFT) calculations [5, 6] was found: there is no quasi-nesting between the hole and electron Fermi surface pockets. However, recent dHvA measurements using very clean single crystals LiFeAs and LiFeP [7] reveal that for both compounds the Fermi surface topology is in good agreement with DFT calculations (Fig. 7.1b, c) and shows quasi-nested electron and hole bands (Fig. 7.1d): quasi-cylindrical hole sheets centered around the Γ -point and two warped electron sheets centered near the M-point of the Brillouin zone. Given detailed information on the electronic structure for both compounds, a comparative study of the '111' materials, LiFeAs and LiFeP, may provide crucial information on the pairing mechanism of this system.

For LiFeAs, the fully gapped superconducting state has been observed in several experiments [4, 8–14]. No residual term κ_0/T at zero-field has been reported by recent thermal conductivity measurements [11], which indicates there are no zero-energy quasiparticle excitations in LiFeAs. Figure 7.2 shows the field dependence of κ_0/T in LiFeAs. Both data for the two directions of heat flow along $(J \mid\mid c)$ and perpendicular $(J \mid\mid a)$ to the c axis are normalized by the normal-state value κ_n/T , respectively. The field dependence of κ_0/T is isotropic for both axes and shows a slow increase at low field and rapid increase as H approaches H_{c2} . Such an isotropic and upward curvature of κ_0/T is a typical behavior expected in an isotropic s-wave superconductor, which is opposite to the field dependence expected for a superconductor with gap nodes, as shown in Fig. 7.2.

Magnetic penetration depth measurements also demonstrate fully gapped superconductivity in LiFeAs [9, 10]. Figure 7.3a shows the temperature dependence of the penetration depth at low temperatures. A clear flat temperature dependence is observed. The best fits to the power-law form, $\Delta\lambda(T) = AT^n$ with n=3.39 (solid line), and exponential form, $\Delta\lambda(T) = \lambda(0)\sqrt{\pi}\,\Delta_0/2T\,\exp{(-\Delta_0/T)}$ with $\Delta_0/T_c=1.09$ (dashed line), for sample #1 are shown in Fig. 7.3a. The smaller gap value obtained from the exponential fit than that of $1.76T_c$ expected for a conventional single gap s-wave superconductor can be explained by two-gap isotropic superconductivity in LiFeAs. Figure 7.3b shows the whole temperature dependence of normalized superfluid density. The analysis based on the framework of the self-consistent γ model reveals two-gap superconductivity with $\Delta_1(0)/T_c=1.89$ and $\Delta_2(0)/T_c=1.11$ (see Fig. 7.3b). Two-gap superconductivity is also supported by magnetization [12], specific heat [13], NMR [14], and ARPES [4] measurements.

Although fully gapped superconductivity has been demonstrated by several experiments in LiFeAs, no information has been reported for the pairing state in LiFeP because of the lack of single crystals. Recently, however, our group succeeded to grow single crystals of LiFeP as big as $150\,\mu\text{m}^2$ [15], which enables us to study the low-energy quasiparticle excitations of LiFeP by using the tunnel diode oscillator with a noise level of one part in 10^9 .

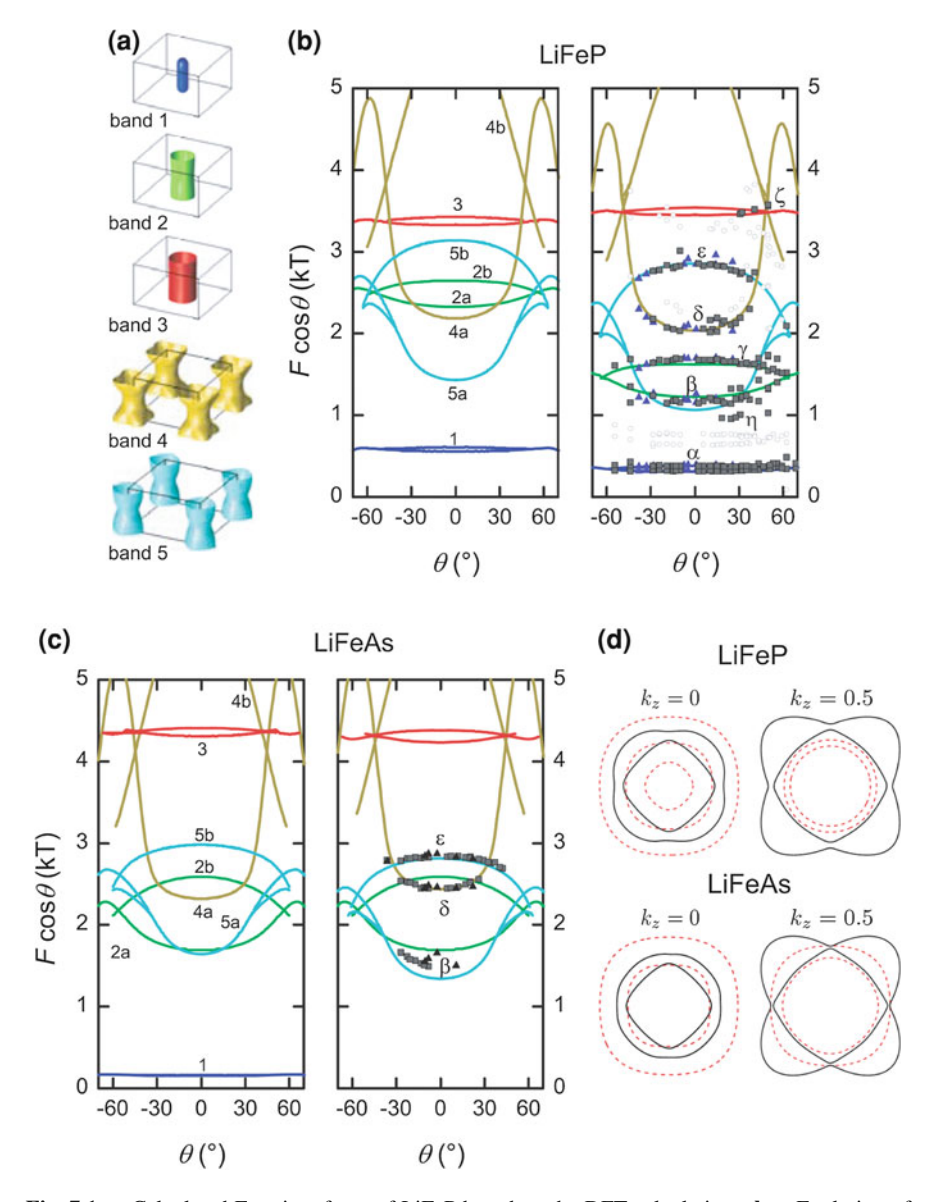


Fig. 7.1 a Calculated Fermi surfaces of LiFeP based on the DFT calculations. b, c Evolution of the dHvA frequencies as a function of magnetic field angle. Experimental data are shown in the *right panels (triangle:* pulsed field, *square/circle:* dc field, circles: 2nd harmonics). The *solid lines* represent the result of the DFT calculations. The bands are shifted in the *right hand panels* to best fit the experimental results. In all panels the frequencies have been multiplied by $\cos\theta$ for clarity. d Cross-sectional views through the determined Fermi surfaces at particular k_z values. The *dashed (solid) lines* are the hole (electron) pockets and the electron pockets have been shifted along the [110] direction such that their center coincides with the holes. The figure is taken from Ref. [7]

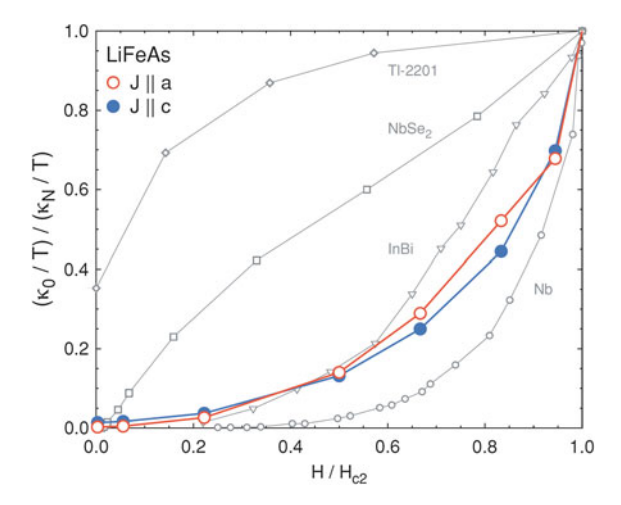


Fig. 7.2 Residual $\kappa_0(H)/T$ versus H/H_{c2} for the two directions of heat flow along $(J \mid \mid c)$ and perpendicular $(J \mid \mid a)$ to the c axis. For comparison, as representatives of standard isotropic s-wave superconductors, the clean Nb and the dirty InBi are shown. Also the results for the d-wave superconductor Tl-2201 and the multiband s-wave superconductor NbSe₂ are shown. The figure is taken from Ref. [11]

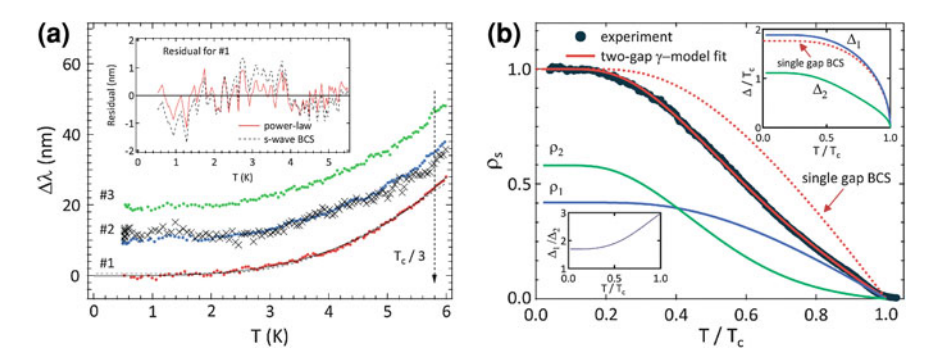


Fig. 7.3 a The low-temperature change in the in-plane penetration depth $\Delta\lambda(T)$ in three crystals of LiFeAs (*solid dots*) and $\Delta\lambda_{c,mix}(T)$ containing a linear combination of λ_{ab} and λ_c for sample #2 (*crosses*). Analysis, which is shown for sample #1, was done assuming both power-law (*solid lines*) and exponential (*dashed line*) T-dependences. The inset shows the comparison of the fit residuals for sample #1 for the power-law and exponential functions. **b** Temperature dependence of the superfluid density calculated with $\lambda(0) = 200 \, \text{nm}$. *Solid lines* show the fit to a two-gap γ model. *Dashed line* represents a single-gap BCS model. Upper inset shows the amplitude of the superconducting gaps $\Delta_1(T)$ and $\Delta_2(T)$, which are extracted from the fitting. Lower inset indicates Δ_1/Δ_2 as a function of temperature. The figure is taken from Ref. [9]

Theories based on antiferromagnetic spin fluctuations suggest that the pnictogen height h_{Pn} above the iron plane is an important factor in determining the structure of the superconducting order parameter [16–18]. Generally, h_{Pn} is much shorter for the P based iron-pnictides in comparison to their As counterparts, so a good test of the theory would be to systematically compare As and P based superconductors. Although this can be achieved in part in the BaFe₂(As,P)₂ series, the fully As containing end member BaFe₂As₂ is a nonsuperconducting antiferromagnet. The same is true for LaFeAsO which is the As analogue of the nodal superconductor LaFePO. Charge doping of the arsenides induces superconductivity, but also introduces disorder which complicates the identification of the pairing state. Therefore, the 111 materials, LiFeAs and LiFeP provide a unique route to study this problem since both materials are superconducting, nonmagnetic, and importantly very clean, with long electronic mean-free paths, as demonstrated by the observation of quantum oscillations [7].

Here, we report on high-precision measurements of the magnetic penetration depth $\lambda(T)$ in single crystals, which demonstrate a nodal gap state in LiFeP in sharp contrast to the nodeless state in LiFeAs. Our analysis based on accumulated $\lambda(T)$ data in the 1111, 122, and 111 series of superconductors indicates that the nodal state is induced when h_{Pn} is below a threshold value. By comparing the electronic band structures of LiFeAs and LiFeP, we discuss the origin of this behavior.

7.2 Experimental

Single crystals of LiFePn (Pn = As or P) grown by a flux method [15] were provided by Dr. Sigeru Kasahara at Kyoto University. The crystal size of LiFeP is up to $135 \times 135 \times 10 \,\mu\text{m}^3$, which is significantly smaller than that of LiFeAs with typical dimensions of $1 \times 1 \times 0.1 \,\text{mm}^3$. dc resistivity measurements show that our crystals are extremely clean with residual resistivity ratios RRR = 57 and 150 for LiFeAs and LiFeP, respectively [15] (see Fig. 7.4a), which are also supported by the observation of dHvA oscillations in magnetic torque measurements [7].

The temperature dependence of change in the magnetic penetration depth was measured by the tunnel diode oscillator technique [19, 20] down to $T/T_c \approx 0.03$ using a 3 He cryostat for LiFeAs and a dilution refrigerator for LiFeP. A weak ac field is applied along the c axis so that the supercurrent flows in the ab plane. To avoid degradation of the samples due to reaction with air, the crystals were handled in an argon glove box and encapsulated in degassed Apiezon N grease before measurements. Sharp superconducting transitions (see Fig. 7.4b) indicate that our procedure does not damage the sample quality for both materials.

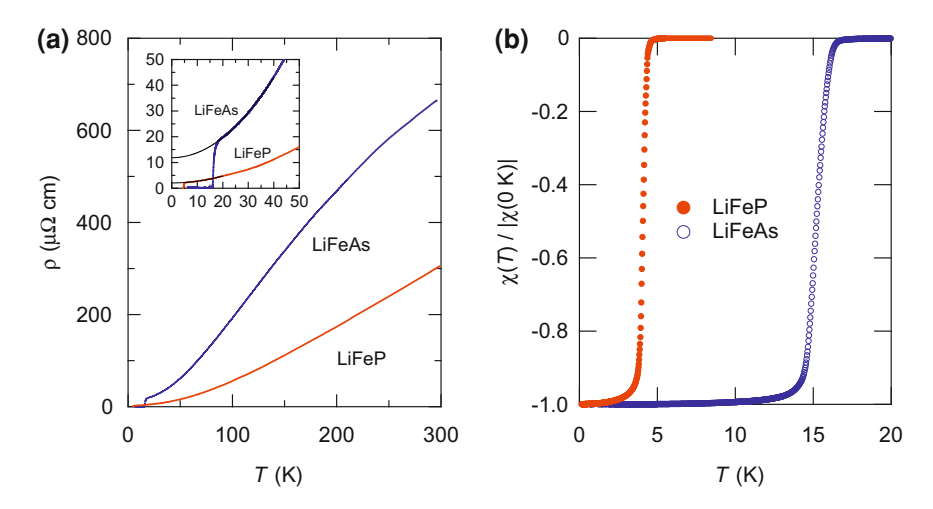


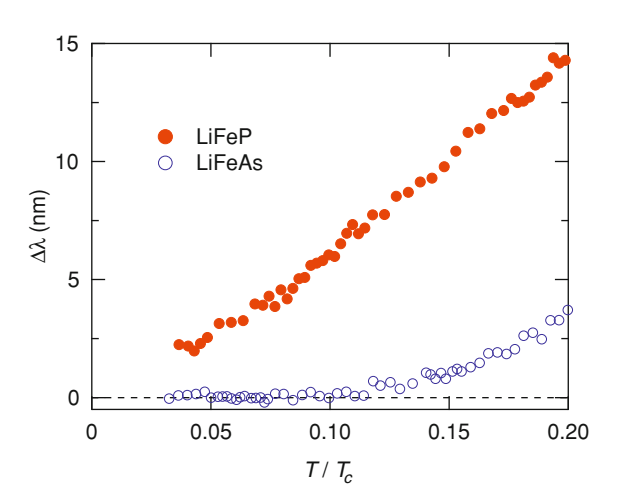
Fig. 7.4 a The temperature dependence of in-plane resistivity $\rho(T)$ for LiFeAs and LiFeP. Inset shows the low-temperature resistivity data. The *solid lines* indicate power law fits $\rho(T) = \rho_0 + AT^2$ with $\rho_0 = 11.9\,\mu\Omega$ cm, $A = 0.020\,\mu\Omega$ cm/K² for LiFeAs and $\rho_0 = 2.06\,\mu\Omega$ cm, $A = 0.0067\,\mu\Omega$ cm/K² for LiFeP, respectively. **b** The ac susceptibility of LiFePn crystals measured from the frequency shift of the TDO

7.3 Results and Discussion

7.3.1 Penetration Depth

Figure 7.5 depicts the low-temperature variation of the in-plane penetration depth $\Delta \lambda(T) = \lambda(T) - \lambda(0)$. The data for LiFeAs are completely flat within the experimental error of ~ 0.3 nm below $T/T_c \sim 0.1$. This demonstrates negligible quasiparticle excitations at low temperatures, indicating a fully gapped state. This result is fully consistent with previous results in LiFeAs [9]. In sharp contrast to LiFeAs, the data for LiFeP exhibit much steeper temperature dependence of $\Delta\lambda(T)$ at low temperatures. When we use a power law fit $\Delta \lambda(T) \propto T^{\alpha}$ to this data below $T/T_c \sim 0.25$, we obtain a small value of $\alpha \approx 1.3$. In iron-based superconductors, as discussed before, a power law dependence with $\alpha \sim 2$ can be expected even in the dirty full gap case when the sign changing s_{\pm} state is considered [21], and indeed a tendency of the exponent decrease from $\alpha \gtrsim 3$ to ~ 2 with increased impurity scattering has been observed experimentally [22, 23]. However, the small power $\alpha \lesssim 1.5$ cannot be explained by such a dirty nodeless state, and it is rather a strong indication that the superconducting gap has line nodes. Indeed, our data can also be fitted to $\propto T^2/(T+T^*)$, which is applicable to the nodal case with small impurity scattering [24]. The obtained low value of $T^* \approx 0.3$ K indicates a clean nodal behavior and is consistent with the other measures of sample quality described above.

Fig. 7.5 Low-temperature change in the magnetic penetration depth in single crystals of LiFeAs and LiFeP



7.3.2 Superfluid Density

We also analyze the normalized superfluid density $\rho_s(T) = \lambda^2(0)/\lambda^2(T)$. To do this we need the value of $\lambda(0)$. The small angle neutron scattering measurements of LiFeAs reveal $\lambda(0) \approx 210 \, \text{nm}$ [8]. The value of $\lambda(0)$ for LiFeP has not been reported. To estimate the value for LiFeP, we consider the difference of the effective mass in these two superconductors because the carrier numbers (Fermi surface volumes) for these materials are quite similar. The effective masses determined by the dHvA oscillations [7] as well as the electronic specific heat coefficients γ have a factor of \sim 2 difference ($\gamma \approx 16$ and \approx 30 mJ/K²mol for LiFeP [2] and LiFeAs [25], respectively), from which we estimate $\lambda(0) \approx 150 \, \text{nm}$. In Fig. 7.6a, we plot the whole temperature dependence of normalized superfluid density for both crystals. The extracted temperature dependence of $\rho_s(T)$ shows contrasting behaviors for As and P cases at low temperatures again: flat dependence for As and steeper dependence for P. The expanded view at low temperatures in Fig. 7.6b demonstrates a wide temperature range of T-linear dependence for LiFeP, which clearly indicates the energy-linear density of state of quasiparticles and hence the existence of line nodes in the energy gap.

7.3.3 Electron-Electron Correlations

The strength of the electron-electron correlations can be estimated by the mass enhancement which is closely related to the A-value obtained from the low-temperature resistivity data and the Sommerfeld coefficient in the specific heat γ . Figure 7.7 shows the Kadowaki-Woods (KW) relations for LiFeAs and LiFeP, which

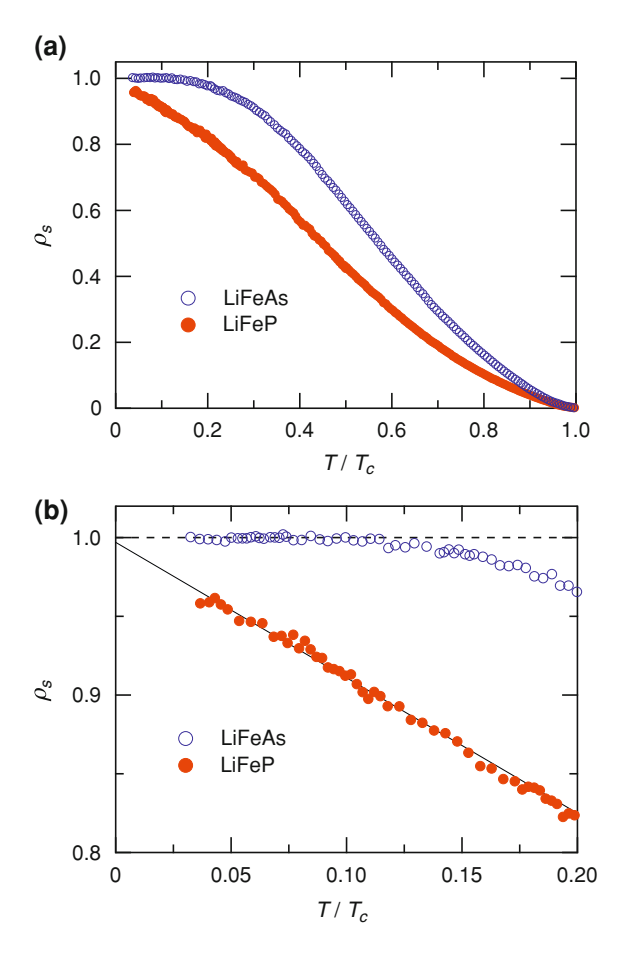


Fig. 7.6 a Temperature dependence of normalized superfluid density $\rho_s(T)$. We used $\lambda(0) = 210$ and 150 nm for LiFeAs and LiFeP, respectively. **b** Expanded view of $\rho_s(T)$ at low temperatures. The *solid line* is a fit to the *T*-linear dependence. The *dotted line* is the guide for eyes

demonstrate that they are in the moderately correlated regime. The larger γ for LiFeAs than for LiFeP suggests weaker correlations in the P case, which is reinforced by the smaller quasiparticle mass enhancements obtained by quantum oscillations [7]. Strong correlations usually promote sign change in the superconducting order parameter [20], which leads to the gap nodes in single-band superconductors. In the present multiband case with separated Fermi surface sheets, however, the opposite trend that LiFeP has nodes but is weakly correlated is observed, which suggests that other factors are also important for node formation.

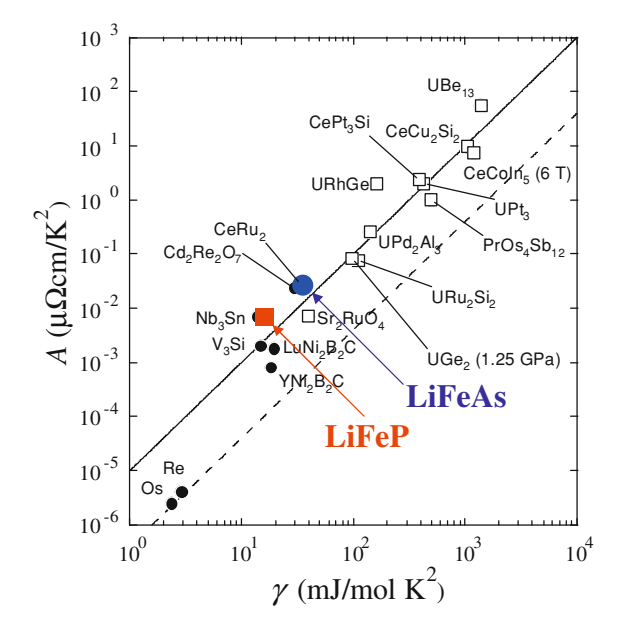


Fig. 7.7 The so-called Kadowaki-Woods-plot. *Circles* represent superconductors with *s*-wave symmetry, while *squares* represent unconventional superconductors with nodes in the gap. The *lines* represent $A = a_{KW} \gamma^2$ with $a_{KW} = 10.5 \,\mu\Omega$ cm (Kmol/mJ)² (*solid line*) and $4 \times 10^7 \,\mu\Omega$ cm (Kmol/mJ)² (*dashed line*)

7.3.4 Pnictogen-Height Dependence of Nodal Versus Nodeless Behaviors

To obtain further insights, we gather the available data for the low-energy quasiparticle excitations in several iron-pnictide superconductors including 1111 [19, 26–28], 122 [20, 22, 29–31], and 111-based materials [9]. The amount of thermally excited quasiparticles is directly related to the change in the penetration depth. Thus we quantify $\Delta\lambda(0.2T_c)$ as a measure of excitations so that we avoid ambiguity resulting from uncertainties in $\lambda(0)$. Among the available data in the literature, we select only the data which shows either $\alpha<1.5$ or >2.5 in the power-law approximation, because the power-law dependence with $\alpha\sim2$ cannot distinguish the dirty nodeless and nodal states as discussed previously. A plot of $\Delta\lambda(0.2T_c)$ as a function of pnictogen height h_{Pn} in Fig. 7.8 suggests that there is a threshold value of ~1.33 Å, below which all the superconductors exhibit significant quasiparticle excitations (with $\alpha<1.5$) characteristic of a nodal state. Above the threshold, most of the materials are nodeless with the exception of the highly hole-doped compound, KFe₂As₂. As discussed in Chap. 6, this particular material is unusual in that it lacks electron sheets. Therefore, our analysis strongly suggests that the pnictogen height is an important parameter that

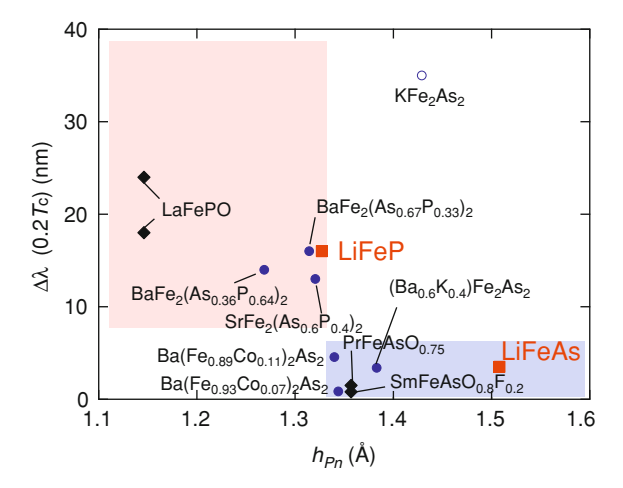


Fig. 7.8 Pnictogen-height dependence of $\Delta\lambda(T)$ at $T=0.2T_c$ as a measure of low-temperature quasiparticle excitations in 1111 (diamonds), 122 (circles), and 111 (squares) series of iron-pnictide superconductors. Here the pnictogen height h_{Pn} is determined from the structural analysis at room temperature [15, 32–35]

determines the gap structure in the iron-pnictide superconductors having significant interband scattering.

The above correlation found in this study is distinct from those proposed between the pnictogen height and T_c [36]. Although the nodes in the gap structure usually tend to suppress T_c , apparently there is no direct correlation between T_c and nodes here. In the 122 system, optimally doped (Ba,K)Fe₂As₂ and BaFe₂(As,P)₂ have almost the same T_c but display nodeless and nodal behavior respectively [29]. Moreover, the h_{Pn} versus T_c correlation does not seem to work for the 111 systems, in which LiFeP has a lower T_c but has a closer h_{Pn} value to the putative optimum height of \sim 1.37 Å [36]. One may also ask about the Fe-Pn-Fe bond angle, but the nodal LiFeP has a closer angle (108.6°) to the perfect tetrahedron value of 109.47° than the nodeless LiFeAs (102.8°), from which we do not find any simple correlation between the bond angle and gap structure in iron-pnictide superconductors.

The importance of the pnictogen height h_{Pn} on the superconducting order parameter in iron-pnictides has been suggested in theoretical considerations based on the antiferromagnetic spin fluctuation mechanism. When h_{Pn} is low, one of the hole bands with d_{xy} orbital character, which is located near the (π, π) position in the unfolded Brillouin zone (BZ), tends to sink below the Fermi level. The disappearance of this Fermi surface makes interband electron-hole scattering weaker and hence the importance of the scattering between electron sheets relatively greater, promoting a sign change of the superconducting gap (and hence nodes) on the electron sheets.

In the LiFeAs/P system this explanation is questionable because band structure calculations [6] suggest that both compounds have a well formed (third) d_{xy} hole sheet. To gain further insights into the important difference in band structure between

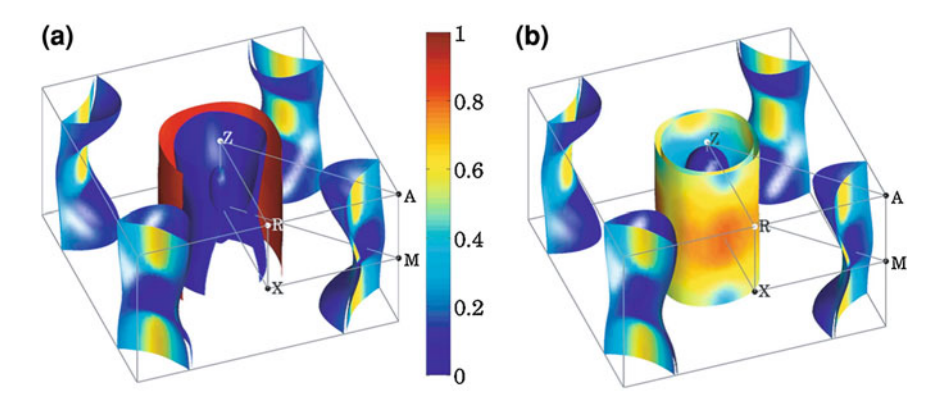


Fig. 7.9 Calculated Fermi surfaces of LiFeAs (a) and LiFeP (b). *Color* indicates the relative weight of the d_{xy} orbital contribution, which has been obtained from the Wannier fit by using WANNIER90 [38] via WIEN2WANNIER interface [39]

LiFeAs and LiFeP we have performed our own density functional theory (DFT) calculations [37] using the experimental lattice constants¹ and internal positions [1] and including the spin-orbit (SO) interaction.

Our results shown in Fig. 7.9 highlight the d_{xy} orbital character of each bands. We find that for LiFeP the size of the outer hole sheet shrinks and its d_{xy} orbital character is significantly suppressed compared to LiFeAs. Moreover, the middle hole sheet in LiFeP has strongly mixed d_{xy} and $d_{xz/yz}$ contributions due to the SO interaction. So despite the presence of the third hole band in LiFeP, its reduced d_{xy} character may be sufficient to tip the balance towards a nodal state.

Bulk Fermi surface dHvA measurements in LiFeP [7] suggest that the middle hole sheet has weaker electron-electron correlations (mass enhancement) than the electron sheets and other hole sheets. This suggests that the mixed orbital character of the two outer hole bands has suppressed electron-hole scattering and by the above argument this leads to the formation of line nodes in the electron sheets.

In Chap. 5, the extended-s state with line nodes in the electron sheets has been discussed as the most likely nodal gap structure of BaFe₂(As,P)₂ [40]. The strong T-linear dependence of superfluid density in LiFeP is consistent with the nodes being on electron bands containing high Fermi velocity parts, which almost coincide with the d_{xy} -dominated regions (yellow parts of the electron sheets in Fig. 7.9b) [15]. To determine the exact node locations in LiFeP, however, other measurements are necessary including angle-resolved probes of low-energy quasiparticle excitations such as thermal conductivity or specific heat measurements in rotated magnetic fields.

Finally, we note that it has also been theoretically suggested that a competition between the orbital fluctuations and spin fluctuations generates nodes in the electron

¹ X-ray diffraction for the LiFeP crystals revealed $a = 3.6955(7) \text{ Å}, c = 6.0411(19) \text{ Å}, z_P = 0.2803(10), and <math>z_{Li} = 0.144(8)$.

sheets [41]. The difference in the orbital character in hole sheets would also change the orbital fluctuations, which may affect the competition and hence the gap structure. Further quantitative calculations of the pnictogen-height effect based on these theories will help clarify the mechanism of iron-based superconductivity.

7.4 Summary

In summary, we have performed the magnetic penetration depth measurements in clean crystals of LiFeAs and LiFeP using the tunnel diode oscillator technique. In LiFeAs the low-temperature $\lambda(T)$ shows a flat dependence indicative of a fully gapped state, which is consistent with previous thermal conductivity, ARPES, and penetration depth measurements. In contrast, LiFeP exhibits a T-linear dependence of superfluid density $\propto \lambda^{-2}$, indicating a nodal superconducting order parameter.

We found the stronger electron-electron correlations for LiFeAs than LiFeP from the Kadawaki-Woods relation, which is the opposite of the general trend that strong correlations usually promote sign change in the superconducting order parameter. These contrasting results may be linked to the pairing origin to the iron-pnictide superconductors.

A systematic comparison of quasiparticle excitations in the 1111, 122, and 111 families of iron-pnictide superconductors implies that the nodal state is induced when the pnictogen height from the iron plane decreases below a threshold value of \sim 1.33 Å. Our result that the nodal state is favored for low h_{Pn} support the trend that the spin-fluctuation theory predicts, but there remains challenging issues including the fact that the emergence of nodes is not directly caused by the disappearance of the d_{xy} hole sheet. It remains to be seen if this can be explained by detailed microscopic calculations.

References

- X.C. Wang, Q.Q. Liu, Y.X. Lv, W.B. Gao, L.X. Yang, R.C. Yu, F.Y. Li, C.Q. Jin, Solid State Commun. 148, 538 (2008)
- Z. Deng, X.C. Wang, Q.Q. Liu, S.J. Zhang, Y.X. Lv, J.L. Zhu, R.C. Yu, C.Q. Jin, EPL 87, 3704 (2009)
- 3. K. Mydeen et al., Phys. Rev. B 82, 014514 (2010)
- S.V. Borisenko, V.B. Zabolotnyy, D.V. Evtushinsky, T.K. Kim, I.V. Morozov, A.N. Yaresko, A.A. Kordyuk, G. Behr, A. Vasiliev, R. Follath, B. Buechner, Phys. Rev. Lett. 105, 067002 (2010)
- 5. D.J. Singh, Phys. Rev. B 78, 094511 (2008)
- 6. I.R. Shein, A.L. Ivanovskii, Solid State Commun. 150, 152 (2010)
- C. Putzke, A.I. Coldea, I. Guillamon, D. Vignolles, A. McCollam, D. LeBoeuf, M.D. Watson, I.I. Mazin, S. Kasahara, T. Terashima, T. Shibauchi, Y. Matsuda, A. Carrington, Phys. Rev. Lett. 108, 047002 (2012)
- 8. D.S. Inosov, J.S. White, D.V. Evtushinsky, I.V. Morozov, A. Cameron, U. Stockert, V.B. Zabolotnyy, T.K. Kim, A.A. Kordyuk, S.V. Borisenko, E.M. Forgan, R. Klingeler, J.T. Park,

References 121

- S. Wurmehl, A.N. Vasiliev, G. Behr, C.D. Dewhurst, V. Hinkov, Phys. Rev. Lett. 104, 187001 (2010)
- 9. H. Kim, M.A. Tanatar, Y.J. Song, Y.S. Kwon, R. Prozorov, Phys. Rev. B 83, 100502(R) (2011)
- Y. Imai, H. Takahashi, K. Kitagawa, K. Matsubayashi, N. Nakai, Y. Nagai, Y. Uwatoko, M. Machida, A. Maeda, J. Phys. Soc. Jpn. 80, 013704 (2011)
- M.A. Tanatar, J.-Ph. Reid, S. Rene de Cotret, N. Doiron-Leyraud, F. Laliberte, E. Hassinger, J. Chang, H. Kim, K. Cho, Y.J. Song, Y.S. Kwon, R. Prozorov, L. Taillefer, Phys. Rev. B 84, 054507 (2011)
- 12. K. Sasmal, B. Lv, Z. Tang, F.Y. Wei, Y.Y. Xue, A.M. Guloy, C.W. Chu, Phys. Rev. B **81**, 144512 (2010)
- 13. F. Wei et al., Phys. Rev. B 81, 134527 (2010)
- Z. Li, Y. Ooe, X.C. Wang, Q.Q. Liu, C.Q. Jin, M. Ichioka, G.Q. Zheng, J. Phys. Soc. Jpn. 79, 083702 (2010)
- S. Kasahara, K. Hashimoto, H. Ikeda, T. Terashima, Y. Matsuda, T. Shibauchi, Phys. Rev. B 85, 060503(R) (2012)
- 16. K. Kuroki, H. Usui, S. Onari, R. Arita, H. Aoki, Phys. Rev. B **79**, 224511 (2009)
- 17. H. Ikeda, R. Arita, J. Kunes, Phys. Rev. B 82, 024508 (2010)
- S. Graser, A.F. Kemper, T.A. Maier, H.-P. Cheng, P.J. Hirschfeld, D.J. Scalapino, Phys. Rev. B 81, 214503 (2010)
- J.D. Fletcher, A. Serafin, L. Malone, J.G. Analytis, J.-H. Chu, A.S. Erickson, I.R. Fisher, A. Carrington, Phys. Rev. Lett. 102, 147001 (2009)
- K. Hashimoto, A. Serafin, S. Tonegawa, R. Katsumata, R. Okazaki, T. Saito, H. Fukazawa, Y. Kohori, K. Kihou, C.H. Lee, A. Iyo, H. Eisaki, H. Ikeda, Y. Matsuda, A. Carrington, T. Shibauchi, Phys. Rev. B 82, 014526 (2010)
- 21. A.B. Vorontsov, M.G. Vavilov, A.V. Chubukov, Phys. Rev. B 79, 140507(R) (2009)
- K. Hashimoto, T. Shibauchi, S. Kasahara, K. Ikada, S. Tonegawa, T. Kato, R. Okazaki, C.J. van der Beek, M. Konczykowski, H. Takeya, K. Hirata, T. Terashima, Y. Matsuda, Phys. Rev. Lett. 102, 207001 (2009)
- H. Kim, R.T. Gordon, M.A. Tanatar, J. Hua, U. Welp, W.K. Kwok, N. Ni, S.L. Budfko, P.C. Canfield, A.B. Vorontsov, R. Prozorov, Phys. Rev. B 82, 060518 (2010)
- 24. P.J. Hirschfeld, N. Goldenfeld, Phys. Rev. B 48, 4219(1993)
- 25. B. Lee, S. Khim, J.S. Kim, G.R. Stewart, K.H. Kim, EPL 91, 67002 (2010)
- L. Malone, J.D. Fletcher, A. Serafin, A. Carrington, N.D. Zhigadlo, Z. Bukowski, S. Katrych, J. Karpinski, Phys. Rev. B 79, 140501(R) (2009)
- 27. K. Hashimoto, T. Shibauchi, T. Kato, R. Okazaki, H. Shishido, M. Ishikado, H. Kito, A. Iyo, H. Eisaki, S. Shamoto, Y. Matsuda, Phys. Rev. Lett. **102**, 017002 (2009)
- C.W. Hicks, T.M. Lippman, M.E. Huber, J.G. Analytis, J.-H. Chu, A.S. Erickson, I.R. Fisher, K.A. Moler, Phys. Rev. Lett. 103, 127003 (2009)
- K. Hashimoto, M. Yamashita, S. Kasahara, Y. Senshu, N. Nakata, S. Tonegawa, K. Ikada, A. Serafin, A. Carrington, T. Terashima, H. Ikeda, T. Shibauchi, Y. Matsuda, Phys. Rev. B 81, 220501(R) (2010)
- 30. K. Hashimoto et al., (unpublished)
- 31. L. Luan, T.M. Lippman, C.W. Hicks, J.A. Bert, O.M. Auslaender, J.H. Chu, J.G. Analytis, I.R. Fisher, K.A. Moler, Phys. Rev. Lett. 106, 067001 (2011)
- K. Kodama, M. Ishikado, F. Esaka, A. Iyo, H. Eisaki, S. Shamoto, J. Phys. Soc. Jpn. 80, 034601 (2011)
- 33. S. Drotziger, P. Schweiss, K. Grube, T. Wolf, P. Adelmann, C. Meingast, H. Lohneysen, J. Phys. Soc. Jpn. 79, 124705 (2010)
- 34. S. Kasahara, T. Shibauchi, K. Hashimoto, K. Ikada, S. Tonegawa, H. Ikeda, H. Takeya, K. Hirata, T. Terashima, Y. Matsuda, Phys. Rev. B 81, 184519 (2010)
- 35. D.C. Johnston, Adv. Phys. 59, 803 (2010) and references therein
- Y. Mizuguchi, Y. Hara, K. Deguchi, S. Tsuda, T. Yamaguchi, K. Takeda, H. Kotegawa, H. Tou, Y. Takano, Supercond. Sci. Technol. 23, 054013 (2010)

- P. Blaha, K. Schwarz, G.K.H. Madsen, D. Kvasnicka, J. Luitz, Wien2k. ISBN 3-9501031-1-2 (2001)
- 38. A.A. Mostofi, J.R. Yates, Y.-S. Lee, I. Souza, D. Vanderbilt, N. Marzari, Comput. Phys. Commun. 178, 685 (2008). www.wannier.org
- 39. J. Kuneš, R. Arita, P. Wissgott, A. Toschi, H. Ikeda, K. Held, Comput. Phys. Commun. 181, 1888 (2010)
- 40. M. Yamashita, Y. Senshu, T. Shibauchi, S. Kasaharsa, K. Hashimoto, D. Watanabe, H. Ikeda, T. Terashima, I. Vekhter, A.B. Vorontsov, Y. Matsuda, Phys. Rev. B **84**, 060507(R) (2011)
- 41. H. Kontani, S. Onari, Phys. Rev. Lett. **104**, 157001 (2010)

Chapter 8 Conclusions

Abstract In order to elucidate the detailed superconducting gap structure of iron-based superconductors, we have performed high precision measurements of the magnetic penetration depth for several iron-pnictide superconductors. We have revealed convincing evidence that the superconducting gap structure of iron-based superconductors is not universal depending on the doping materials and its doping levels. In addition, we have performed three different absolute penetration depth measurements for the $BaFe_2(As_{1-x}P_x)_2$ series over a wide range of x to explore the possibility of a quantum phase transition beneath the superconducting dome. The significant influence of quantum critical fluctuations associated with the QCP on the condensed electron pairs in the superconducting state is evident from the present study. In this chapter, we will summarize the results of this study.

Keywords Superconducting gap structure · Quantum critical point · Iron-based superconductor · Magnetic penetration depth

In order to elucidate the detailed superconducting gap structure of iron-based superconductors, we have performed high precision measurements of the magnetic penetration depth using the tunnel diode oscillator and microwave cavity perturbation techniques. In this study, we have revealed that in the iron-based superconductors there is convincing evidence that the superconducting gap structure is not universal depending on the doping materials and its doping levels. In certain materials such as optimally doped $(Ba_{1-x}K_x)Fe_2As_2$, strong evidence for a fully gapped superconducting state has been observed from several low-energy quasiparticle excitation probes. In contrast, through this study significant quasiparticle excitations at low temperatures due to nodes in the energy gap have been revealed for several iron-based superconductors such as $BaFe_2(As_{1-x}P_x)_2$ ($T_c \leq 30 \, \text{K}$), KFe_2As_2 ($T_c = 4 \, \text{K}$), and LiFeP ($T_c = 5 \, \text{K}$). The fact that the superconducting gap structure depends on the detailed electronic structure of individual iron-based superconductors imposes

124 8 Conclusions

an important constraint on the pairing mechanism of the iron-based superconductor, which is quite different from high- T_c cuprate superconductors which all have a nodal $d_{x^2-y^2}$ pairing state. In addition, we have performed three different absolute penetration depth measurements for the BaFe₂(As_{1-x}P_x)₂ series over a wide range of x to explore the possibility of a quantum phase transition beneath the superconducting dome. The significant influence of quantum critical fluctuations associated with the QCP on the condensed electron pairs in the superconducting state is evident from the present study. In the following, we will summarize the results for these materials.

Isovalent-doped BaFe₂ $(As_{1-x}P_x)_2$

The observation of quasi-T-linear penetration depth over a wide range of x (0.26 $\leq x \leq 0.64$) indicates that the presence of line nodes in the gap is a robust signature of the BaFe₂(As_{1-x}P_x)₂ system, which is consistent with the nodes being on the electron sheets rather than the hole sheets whose shapes change significantly with x. By combining several results for the isovalent-doped BaFe₂(As_{1-x}P_x)₂, we conclude that the observed results are most consistent with the closed nodal loops located at the flat parts of the electron Fermi surface with high Fermi velocity.

Besides, the x-dependence of $\lambda(0)$ exhibits a sharp peak at the optimum composition x=0.30 ($T_c=30\,\mathrm{K}$), demonstrating pronounced quantum fluctuations associated with the QCP, which separates two distinct superconducting phases. This gives the first convincing signature of a second-order quantum phase transition deep inside the superconducting dome. Moreover, the ratio of T_c to T_F at x=0.30 marks the highest record among superconductors exceeding the cuprate case and even approaches the superfluid $^4\mathrm{He}$ value, implying a possible crossover towards the Bose-Einstein condensate driven by quantum criticality.

Heavily hole-doped KFe₂As₂

The observed steep T-linear dependence of $\lambda(T)$ at low temperatures indicates the existence of low-energy quasiparticle excitations in KFe₂As₂, which is totally different from the flat temperature dependence observed in the optimally doped $(Ba_{1-x}K_x)Fe_2As_2$. Our analysis based on the DFT band calculations and dHvA results have revealed that there are line nodes in the energy gap on the large hole sheets at the Γ point. This is different both from the nodeless states found in $(Ba_{1-x}K_x)Fe_2As_2$ and from the nodal s-wave state with nodes in the electron bands as in the case of $BaFe_2(As_{1-x}P_x)_2$. The recent laser ARPES result that eight-fold sign reversal in the gap function is realized in KFe₂As₂ suggests that the non-universal superconducting gap structure in iron-pnictides can be interpreted in the framework of A_{1g} symmetry.

Stoichiometric LiFeAs and LiFeP

In LiFeAs, the low-temperature penetration depth shows a flat dependence indicative of a fully gapped state. In contrast, LiFeP exhibits a T-linear dependence of $\lambda(T)$, indicating a nodal superconducting order parameter. We found that the stronger

8 Conclusions 125

electron-electron correlations for LiFeAs than LiFeP from the Kadawaki-Woods relation, which is the opposite of the general trend that strong correlations usually promote sign change in the superconducting order parameter. These contrasting results may be linked to the pairing origin to the iron-based superconductors. Moreover, a systematic comparison of quasiparticle excitations in the '1111', '122', and '111' families of iron-based superconductors implies that the nodal state is induced when the pnictogen height from the iron plane decreases below a threshold value of $\sim 1.33 \,\text{Å}$. Our result that the nodal state is favored for low h_{Pn} support the trend that the spin-fluctuation theory predicts, but there remains challenging issues including the fact that the emergence of nodes is not directly caused by the disappearance of the d_{xy} hole sheet.